This is to certify that the

dissertation entitled

Advanced Electron Paramagnetic Resonance Studies of Some Sodides and an Electride.

presented by

Kerry Ann Reidy-Cedergren

has been accepted towards fulfillment of the requirements for

Doctorate degree in ~~Chemistry~~

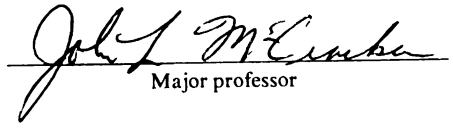

Major professor

Date ~~December 10, 1996~~

ADVANCED EPR STUDIES OF SOME SODIDES AND AN ELECTRIDE

By

Kerry Ann Reidy-Cedergren

A DISSERTATION

Submitted to
Michigan State University
in partial fulfillment of the requirements
for the degree of

DOCTOR OF PHILOSOPHY

Department of Chemistry

1996

ABSTRACT

ADVANCED ELECTRON PARAMAGNETIC RESONANCE STUDIES OF SOME SODIDES AND AN ELECTRIDE

By

Kerry Ann Reidy-Cedergren

Electrides are a class of compounds in which an alkali metal cation is encapsulated by a complexant, usually a crown ether or a cryptand, and the unpaired electron occupies the anionic site in a well defined structural arrangement. The nature of the sites in which these electrons are located is important to their physical and magnetic properties. Electron paramagnetic resonance (EPR) is a good tool for studying these trapping sites. However, since the electrons are so close together, rapid electron exchange often occurs to yield a single exchange narrowed EPR signal. A closely related compound to electrides, alkalides, differs in that an alkali metal now acts as the anion. Trapped electrons are much more isolated than the electrons in electrides, thus they are present in small concentrations which avoids the problems of exchange-narrowing of the EPR spectrum. Often there are weak, superhyperfine couplings between the paramagnetic center and the nearby magnetically-coupled nuclei that are unresolved in the cw-EPR spectrum due to inhomogeneous broadening of

the resonance lineshape, which can mask the hyperfine structure in th EPR spectrum. Spin-echo experiments can reverse this observation.

Cavity-trapped electrons in the electride Li^+(cryptand [2.1.1]e^- ca interact through rather open channels that connect the cavities to forı essentially 1D linear chain Heisenberg antiferromagnets (LCHAs). I each case, the EPR spectrum of powdered samples consists of a narrow, (2 G. p.p.) slightly anisotropic absorption whose integrated intensity vs. mirrors the static susceptibility. Very strong *rf* responses in an ENDO cavity during near-saturation microwave irradiation, at magnetic fiel offsets on either side of the EPR line, match the EPRlineshape. Th frequency at a given position on the *rf* response curve is equal to th frequency equivalent of the field offset from the corresponding position o the EPR curve. The linear power dependence of the intensity shows that th *rf* absorption is a one-photon process. This *rf*-microwave doubl resonance demonstrates the presence of a high density of energy level around the Zeeman level, consistent with the presence of 1D, spin 1/ antiferromagnetic spin-waves, with average lengths of about 50 spins.

ACKNOWLEDGMENTS

This can often be the most difficult part of the thesis writing for of leaving someone out! I will try to include everyone. First I would li thank my two advisors, Professors John McCracken and Jim Working for such different people has been a very stimulating experi I cannot think of two better mentors for one to have during grad school. I thank you both for your patience with me over the years an teaching me how to be an independent thinker. I will miss the stories Professor McCracken has provided over the years!! There *is* no substi I would also like to thank my other committee members, Professors Blanchard and Mike Rathke.

I would not have been able to function without the excellent se provided by the glass shop. Manfred, Scott and Keki were always wi to give my job high priority if I needed it badly enough and I thank t for that. In addition, Russ, Dick and Sam offered excellence in machine shop that is second to none. Of course, Ron, Scott and Tom always there for me when I blew a major fuse and shut down the vac lines. MSU is very fortunate to have such talented service shops.

No thesis could ever be completed without the help from secreta There have been four in particular who have helped over the years, Li

Vada, Beth and Lisa and they deserve tremendous thanks and appreciation.

Graduate school presents the opportunity to meet new people and have been very fortunate to meet many friends over the years who are more than just friends. In particular, Dr. Michelle Mac has offered a friendship that is unsurpassed by any other friendship that I have had. cannot thank her enough for going through all of the hoops with me, from qualifiers to the final defense. She always could make me laugh, even when I had already heard the joke before! I know that good friends never fade and distance will not keep us from staying in touch.

There are many other friends who have provided an occasional diversion from work. I thank them all (Sara, Jeff, Beth, Paul, Deena, Chris Tom, Jerry, Per...) and I will miss them all.

I want to thank the group members that I have worked with over the years. In particular, Rui, Song, Erik, Andrew and Mike, and also the Hong-In meister (for **countless** scientific discussions), Professor Kurt Warncke, *the boys* (György and Vlad) and all of the new McCracken students.

My family, Mom, Dad, Michael, Trish, little Garrett, Pam, Keegan Krysta, Matty (*polis*), Sean, Mom, Karen, Tom, Linnea, Mark, Kyle and Keith: You have all at some time during my career, been very supportive and I thank you for that!!

My daughter, Alexandria, has been the light of my life and inspires me every day. Now that I have her, I can't imagine life without her. Finally, I wish to thank my husband Rob. You are my hero, always saving me when I am in a bind, always there for emotional support, and always there to make me laugh. I cannot imagine how empty my life would be without you and I thank you dearly.

To Rob and my little Alexandria Emily

TABLE OF CONTENTS

Page

LIST OF TABLES xi

LIST OF FIGURES xii

CHAPTER 1. A historical perspective of alkalides and electrides. 1
Introduction 2
Alkali metal solutions 3
Electrides 5
Thermodynamic considerations 8
Complexing agents: Crown ethers 9
Complexing agents: Cryptands 11
The first electride crystal structure: $Cs^+(18C6)_2e^-$ 13
Localized and delocalized electrons 15
Trapped electrons 22
The first alkalide 25
Important theoretical considerations 27
An overall message... 32
Bibliography 36

CHAPTER 2. Synthesis of Cesium Hexamethyl Hexacyclen Sodide: $Cs^+(HMHCY)Na^-$. 41
Introduction 42
Preparation of $Cs^+(HMHCY)Na^-$ 44
Bibliography 53

CHAPTER 3. Theoretical Treatment of Electron Magnetic Resonance Spectroscopy 54

Spectroscopy 55
Magnetic interactions 55
The spin operator 59
The spin Hamiltonian 60
The EPR experiment 69
Application of the Hamiltonian 71
Relaxation 73
Electron spin echo envelope modulation 77
Nuclear modulation effect 81
The density matrix formalism 84
EPR instrumentation 90
The Michigan State University ESEEMometer 92
Bibliography 94

CHAPTER 4. Interesting Magnetic Behavior of the Electride:
$Li^+(C211)e^-$. Evidence for 1-Dimensional Spin Waves. 95
Introduction 96
Previous Studies 97
Synthetic considerations 99
Structral facts 101
Properties of newly synthesized $Li^+(C211)e^-$ 106
Brief magnetism primer 108
The spin-Peierls transition 112
Susceptibility data 113
EPR 116
Pulsed- EPR measurements 121
Anamolous *rf*-effect 127
ENDOR-Induced EPR (EIE) 135
Analysis of magnetic data 136
Discussion 145
Conclusions 146
Bibliography 149

CHAPTER 5. ESEEM Studies of Electron Trapping in
$Cs_2^+(21C7)Na_2^-$: Mapping the Electron Density. 154
Background information 155

Synthesis of $Cs_2^+(21C7)Na_2^-$ 15
Structural information 15
Physical properties of $Cs_2^+(21C7)_2Na_2^-$ 16
Summary of the physical properties 16
Pulsed and cw-EPR experiments 16
Discussion 17
Bibliography 18

CHAPTER 6. Multifrequency ESEEM Studies of Potassium
Hexamethyl Hexacyclen Sodide. 18
Background information 18
Structural information 18
Thermal stability 19
EPR studies 19
ESEEM studies 19
Conclusions 19
Bibliography 20

LIST OF TABLES

Table 1.1: Alkali metal radii. ..... Page 11.

Table 1.2: Hole diameters of some crown ethers. ..... Page 12.

Table 1.3: Current structural data of alkalides and electrides. Page 35.

Table 5.1: Comparison between the time domain and the frequency domain. ..... Page 175.

LIST OF FIGURES

Figure 1.1: Typical complexants used in the synthesis of alkalides and electrides. ..... Page 14.

Figure 1.2: Ball and stick model of $Cs^+(18C6)_2e^-$. ..... Page 16.

Figure 1.3: Optical absorption spectra of solvent free electride films. ..... Page 18.

Figure 1.4: cw-EPR spectra of $K^+(C222)e^-$ before and after irradiation. ..... Page 20.

Figure 1.5: Picture of an *F-center* where the electron density occupies the anionic vacancy. ..... Page 24.

Figure 1.6: Drawing of an interstitial ion. ..... Page 24.

Figure 2.1: Pyrex® K-cell used in the synthesis of alkalides and some electrides. ..... Page 45.

Figure 2.2: Quartz apparatus for loading alkalide and electride samples into EPR tubes. ..... Page 51.

Figure 3.1: Classical picture of the energy of a dipole in a magnetic field. ..... Page 57.

Figure 3.2: The interacting dipoles, μ_e and μ_n in a magnetic field. ..... Page 63.

Figure 3.3: Radial dependence of *1s*, *2p* and *3d* wavefunctions of the hydrogen orbital. ..... Page 65.

Figure 3.4: The effect of the H_1 field on the laboratory magnetic field. ..... Page 66.

Figure 3.5: Axial *g*-tensor. ..... Page 68.

Figure 3.6 Electron spin levels in a magnetic field. ..... Page 70.

Figure 3.7: Energy level diagram for an S=1/2, I=1/2 system. .. Page 74.

Figure 3.8: Inhomogeneously broadened line. ..... Page 76.

Figure 3.9: Illustration of the rotating frame. ..... Page 76.

Figure 3.10: Diagram showing the time evolution of the echo decay envelope.. ..... Page 78.

Figure 3.11: Precessional frequencies of the individual spin packets. ..... Page 79.

Figure 3.12: Vector scheme for the two-pulse ESEEM experiment. ..... Page 80.

Figure 3.13: ESEEM pulse schemes for the two and three pulse experiments. ..... Page 82.

Figure 3.14 Nuclear modulation effect for the two-pulse ESEEM sch ..... Page

Figure 3.15a: Coupling of two electrons with an I=1/2 nuc ..... Page

Figure 3.15b: Transition matrix elements connecting the four st ..... Page

Figure 3.16: Transformation rotation. ..... Pag

Figure 3.17: Basic diagram of the microwave bridge components. ..... Page

Figure 4.1: Optical spectra of $Li^+(C211)e^-$ from liquid amm solutions of various ratios. ..... Pag

Figure 4.2: Space filling model of one molecule of $Li^+(C211)e^-$. Page

Figure 4.3: Packing diagram of $Li^+(C211)$ complexed cations. Page

Figure 4.4: Channel and cavity diagram of $Li^+(C211)e^-$. ..... Page

Figure 4.5: Magnetic flux lines. ..... Page

Figure 4.6: Susceptibility as a function of the temperature antiferromagnetic, paramagnetic and ferromag material. ..... Page

Figure 4.7: Magnetic susceptibility of A) crushed crystals an "powder" of $Li^+(C211)e^-$ as a function of the tempera ..... Page

Figures 4.8: EPR spectra of $Li^+(C211)e^-$ at various temperatures. ..... Page

Figure 4.9: EPR spectra of $Li^+(C211)e^-$ at various temperatures. ..... Page

Figure 4.10: EPR spectra of $Li^+(C211)e^-$ at various temperatures. ..... Page

Figure 4.11: Relative intensity for the EPR resonance as a function o temperature for A) crushed crystals and B) "pow samples. ..... Page

Figure 4.12: ESE-detected EPR spectrum of $Li^+(C211)e^-$ collected at 9. GHz; repeition rate 60 Hz; temperature 4.20 K; τ=180 ns. ..... Page

Figure 4.13: Time domain trace of $Li^+(C211)e^-$ (τ =170 ns). ..... Page

Figure 4.14: Time domain trace of $Li^+(C211)e^-$ (τ =263 ns) ..... Page

Figure 4.15: Energy level diagram describing the effect of nu
hyperfine interactions. ..... Page

Figure 4.16: Relaxation pathways in a typical ENDOR experiment.
..... Page

Figure 4.17: Microwave saturation study. ..... Page

Figure 4.18: cw-EPR spectrum collected at 25 K. 'ENDOR' spectra coll
at 3360.0 G and 3358.0 G. ..... Page

Figure 4.19: cw-EPR spectrum collected at 25 K. 'ENDOR' spectra coll
at 3364.0 G and 3367.0 G. ..... Page

Figure 4.20: Plot of the peak position of the 'ENDOR' effect as a fun
of the dc static field offset, converted to MHz. ..... Page

Figure 4.21: Start frequency as a function of the separation betwee
peaks of the ENDOR induced EPR. ..... Page

Figure 4.22: ENDOR induced EPR spectra of $Li^+(C211)e^-$. ..... Page

Figure 4.23: Illustration showing the possible spin interactions in the
zag chains of $Li^+(C211)e^-$. ..... Page

Figure 4.24: Antiferromagnetic spin waves on a line of spins. .. Page

Figure 4.25: Possible energy level diagram describing the anam*rf*-effect. ..... Page

Figure 5.1: Ortep diagram of $Cs^+_2(21C7)2Na^-_2$. ..... Page

Figure 5.2: One view of four unit cells of $Cs^+_2(21C7)2Na^-_2$. .. Page

Figure 5.3: Alternate view of the packing of $Cs^+_2(21C7)2N$ ..... Page

Figure 5.4: A) Optical spectrum of the solvent evaporated fil $Cs^+_2(21C7)2Na^-_2$ in $MeNH_2$. B) ^{23}Na static NMR spec of $Cs^+_2(21C7)2Na^-_2$ powder. ..... Page

Figure 5.5: A) 133Cs static NMR spectrum recorded at 200K. MAS-NMR spectrum recorded at 200K at B) 5 kHz spi speed and C) 10 kHz spinning speed. ..... Page

Figure 5.6: A) cw-EPR spectrum collected at 2.08 μW microwave p 9.4716 GHz microwave frequency, 5.2 Gpp modul amplitude, 100 kHz modulation amplitude, $5x10^5$ gai 3.8 K. B) ESE-EPR spectrum collected at 4.2 K, 250 ns τ, 5 repitition rate, 45.0 dBm microwave power, 10.011 microwave frequency. ..... Page

Figure 5.7: A) 2-pulse ESEEM trace collected at 9.282 GHz micro frequency, 3324.0 G field strength, 180 ns τ, 10 Hz repe

rate and 4 scans collected. B) fourier transform spectrum of trace A. ..... Page 171.

Figure 5.8: A) 3-pulse ESEEM trace collected at 9.282 GHz microwave frequency, 3324.0 G field strength, 180 ns τ, 10 Hz repetition rate and 16 scans collected. B) fourier transform spectrum of trace A. ..... Page 172.

Figure 6.1: Attempts to "cap" the alkali metal cation complexed by HMHCY with 12C4, have thus far failed. .....Page 185.

Figure 6.2: Structural information for two HMHCY sodide. ..Page 187.

Figure 6.3: Diagram of $K^+(HMHCY)Na^-$. .....Page 188.

Figure 6.4: Perspectives of $Cs^+(HMHCY)Na^-$ .....Page 189.

Figure 6.5: A) 3-pulse ESEEM trace of $K^+(HMHCY)Na^-$ at 3300 G, where τ = 288 ns., T=42 ns., tinc = 10 ns., repetition rate = 40 Hz. B) Fourier transform spectrum of A. ..... Page 193.

Figure 6.6: A) 3-pulse ESEEM trace of $K^+(HMHCY)Na^-$ at 3300 G, where τ = 324 ns., T=46 ns., tinc = 10 ns., repetition rate = 40 Hz. B) Fourier transform spectrum of A. .....Page 196.

Figure 6.7: A) 3-pulse ESEEM trace of $K^+(HMHCY)Na^-$ at 4250 G, where τ = 288 ns., T=42 ns., tinc = 10 ns., repetition rate = 40 Hz. B) Fourier transform spectrum of A. ..... Page 198.

CHAPTER 1

A HISTORICAL PERSPECTIVE OF ALKALIDES AND ELECTRIDES

INTRODUCTION

Ionic salts can be defined by two important characteristics: the packing, which is composed of well defined charged species, and the size difference of the anions and cations. The *-ide* ending of sodium chlor*ide*, which packs in a face-centered cubic lattice, implies that chlorine must be negatively charged. Chlorine has an electron affinity of -348 kJ/mol* thereby exhibiting a strong attraction for an electron. It, as well as the other halogens, most commonly retain the minus one oxidation state since the extra electron will fill the outer p-orbital giving the more stable inert gas electron configuration. Since sodium and the other alkali metals are good electron donors, they most commonly possess the plus one oxidation state. These metals will eagerly give up an electron to an acceptor atom or molecule, to form a stable salt. They are so reactive in their metallic state that this form does not even exist in nature. Alkali metals may be the most electropositive family, but they too can form salts that contain alkali metal

*Convention states that the larger the negative value of electron affinity, the more attraction it will have for an electron.

anions. In fact, alkali metal anions in the gas phase have been known to exist for almost fifty years (Patterson *et al.*, 1974). Therefore, if the gegenion were sufficiently resistant to reduction, one might believe that an ionic salt of an alkali metal anion could be stable. The electron affinity of sodium is -52.9 kJ/mol indicating that there is still somewhat of an attraction for an extra electron. After all, adding an electron to an alkali metal fills the outer s-orbital but in a less strongly favored configuration than the sodium cation configuration, so it was deemed *highly* unlikely. In 1974 it was found that alkali metals, under very specific conditions, could form stable ionic salts where the alkali metal maintains both a plus one oxidation state as well as the peculiar minus one oxidation state in a well defined structural arrangement (Tehan *et al.*, 1974). This class of compounds was coined *alkalides* and the structures and properties of these compounds have been extensively studied for over twenty years (for useful review articles, see (Dye, 1977, Dye, 1979, Dye, 1987, Dye, 1993, Dye & Ellaboudy, 1984, Wagner & Dye, 1993) and they continue today.

Alkali metal solutions

In 1864 it was reported that alkali metals could dissolve in liquid ammonia to generate a beautiful blue color, (Weyl, 1864) . Sir Humphrey Davy had made a similar observation in 1808 (Edwards & Sienko, 1982) as was drafted in his laboratory notebook. However, the blue color and

the optical spectrum were not assigned to solvated electrons until Kraus studied the nature of dilute metals in liquid ammonia and established that these solutions were ionic in nature (Kraus & Lucasse, 1921, Kraus & Lucasse, 1922). He also studied extensively the metallic behavior of these concentrated solutions, and coined the term "solvated electron" (Kraus, 1907). Kraus did much of the pioneering work in the field of alkali metal solutions and found in 1907 that lithium was soluble in both methylamine ($MeNH_2$) and ethylamine ($EtNH_2$), and that potassium was soluble in ethylenediamine, but that the other alkali metals were relatively insoluble in most higher primary amines (Kraus, 1907). Since that discovery, there have been widespread studies of solvated electrons in liquid ammonia solutions by electron magnetic resonance as well as optical spectroscopy and many other physical measurements and theoretical treatments (Thompson, 1976). Such work has revealed many aspects of the reactivity of solvated electrons in addition to the physical characterizations. To understand solvated electron structure, it is useful to consider that solvated electrons are formed kinetically by a two stage process (Kevan, 1981). First, localization occurs which depends on the relative energies of the conduction electron level of the medium as well as the energy of the localized electron state in the medium. Once localization is accomplished, solvation occurs. In this case, the electron induces rearrangements in the surrounding shell of solvent molecules which

creates a geometry between them. As a result, the geometry of the solvated electron depends on more than just the medium molecules.

The possible reaction in dilute liquid ammonia solutions

$$M^- \rightleftharpoons M^+ + 2e^-_{solv} \qquad (1.1)$$

where M^- is an alkali metal anion, M^+ is an alkali metal cation and e^-_{solv} is a solvated electron, is shifted far enough to the right that M^- has never been detected in this solvent. Additional complications arise as the solution becomes more concentrated due to the appearance of metallic behavior, ion-pair formation and electron spin-pairing. Thus, there is no direct evidence that alkali metal anions exist in liquid ammonia solvent, and in fact, their existence has recently been brought into serious doubt by studies of concentrated mixed Li-Na solutions (DeBacker *et al.*, 1994).

Electrides

The electron itself is the simplest anion; therefore, if all of the alkali metal anions were replaced by trapped electrons, the salt would no longer be an alkalide, but an *electride*. Electrides are a class of compounds in which an alkali metal cation is encapsulated by a crown ether "sandwich" or a cryptand and stoichiometric amounts of electrons are released to be trapped in vacancies. Thus, the electron occupies the anionic vacancy and serves as the anion. The nomenclature does not apply to systems with

well defined molecular orbitals that localize the charge to a single molecular center. Therefore, typical organic anion radicals would not be defined as electrides since optical and electron paramagnetic resonance (EPR) measurements have shown that the unpaired electron occupies specific orbitals on the molecule. If the density of the trapping sites in electrides is low enough, strong overlap of the wavefunctions of neighboring electrons to form a metal can be prevented and localization of electrons to form electrides can occur. Localization of electrons has an important impact on the characteristics of the electride. A measure of this has been described. Mott (Mott, 1956) stated that at the non-metal to metal transition,

$$a_H (n_c)^{1/3} = 0.25 \qquad (1.2)$$

where n_c is the critical electron concentration, and a_H is an effective hydrogen-like radius for the localized electron. Electrides are highly paramagnetic species with an average electron concentration on the order of 10^{21} cm^{-3}. The packing of the large cations leaves holes which are similar in size to the effective radius of the trapped electrons. These dimensions yield an effective hydrogen-like radius for the localized state to be about 2.5 Å so that the left-hand side of Equation 1.2 is nearly 0.25. Even a slight change in electron concentration or in the effective radius of the electron could lead to some delocalization of the electrons and

possibly to a metallic state in the electride. In such a case, the material is not a true electride but an "expanded metal".

Electrides originate from solvated electrons and alkalides from solvated alkali metal anions. Solvated electrons are thought of as electrons in solution that do not belong specifically to one single molecule or even to a collection of molecules that maintain a well defined geometry. Because of the light mass of the electrons, they are considerably more mobile than other anions in salts and thus are fairly free to travel throughout the solution; this ability contributes to their unique properties. These traits of solvated electrons have been studied by a number of different research groups in a time period of more than eighty years. To prepare stable solutions that contain solvated electrons or alkali metal anions, solvent choice is of utmost importance. The solvent needs to be resistant to reduction and to be a strong solvator of the cation but need not solvate the electron or the alkali metal anion strongly. Alkali metals only dissolve in a few solvents other than ammonia, such as hexamethyl phosphoramide (HMPA), a few primary amines, and a few polyethers. Some more considerations regarding solvent choice during the preparation of alkalides and electrides will be discussed throughout this dissertation.

Thermodynamic Considerations

Thermodynamically, metals with a low ionization energy and small lattice energy can dissolve in amines and other previously mentioned solvents. The equilibria that describe the solubility of alkali metals in the proper solvents are shown in Eqs. 1.3 & 1.4,

$$M_{(s)} \rightleftharpoons M^{+}_{solv} + e^{-}_{solv} \qquad (1.3)$$

$$M_{(s)} + M'_{(s)} \rightleftharpoons M'^{+}_{solv} + M^{-}_{solv} \qquad (1.4)$$

where M and M' can be the same or different alkali metals. This reaction is shifted far to the right when an organic complexant is added to the mixture (Eq. 1.5), where C denotes the polyether complexant.

$$M^{+} + C \rightleftharpoons M^{+}C \qquad (1.5)$$

Because of the importance of the solvation energy of the cation, the metal anion and the solvated electron, the presence of the complexant can drive reactions 1.3 and 1.4 to the right. Solvated electrons are the best reducing agents with the alkali metal anions nearly as powerful. If they were not so unstable and if the conditions did not have to be so stringent, these solutions would be much more common. Empirical results have shown that the equilibrium of reaction 1.1 in $NH_{3(l)}$ lies far to the right

while this reaction in other solvents is not as favorable and as a result, the solution contains both alkali metal anions and solvated electrons.

Complexing agents: *Crown Ethers*

By making use of the discovery of crown ethers by Pedersen (Pedersen, 1967a, Pedersen, 1967b, Pedersen, 1988) and of cryptands by Lehn (Lehn *et al.*, 1970), the Dye group showed that the solubility of the alkali metals could be greatly increased (Dye, 1991). In fact, when potassium metal is allowed to interact with Me_2O, the colorless solution shows that the potassium does not dissolve and produce solvated electrons. This indicates that the equilibrium concentration is less than 10^{-5} M at saturation (Dye, 1991). However, when 15C5 is added to the mixture, the solubility is increased by over four orders of magnitude to 0.3M at 240 K, (Dye, 1991). It follows then that an important aspect of synthesizing alkalides or electrides is the complexing ability of the species that encapsulates the cation. The particular complexant must be resistant to reduction as well as to decomposition and decomplexation. Pedersen showed that the macrocyclic polyethers could form stable complexes with alkali metal cations and that the stability of these complexes was of enormous importance. He showed that the stability depends on the geometrical disposition and the number of ether oxygen atoms in the macrocycle (Pedersen, 1970). Moreover, the size and the shape of the

coordinating polyhedra relative to the cation size was shown to be of importance. These results indicate that the stability of the alkali metal crown-complexed cation does not necessarily follow the conventional trend that the weak coordinating ability in alkali metal chemistry is due to the relatively large size and low charge density of the alkali metal cations (Greenwood & Earnshaw, 1984). Conventional logic predicts that the strength of the coordinated complexes should decrease in the order Li>Na>K>Rb>Cs. However, the maximum stability of alkali metals with crown ethers is often Na^+ and sometimes K^+ or Rb^+ but not necessarily Li^+. Pedersen found that the formation of complexes can be prevented by steric hindrance from the polyether ring (Pedersen, 1967a, Pedersen, 1967b) Complex formation is shown by Eq. 1.6.

$$(M^+)_{solvent} + C \rightleftharpoons CM^+ + solvent \qquad (1.6)$$

Therefore, complex formation of an alkali metal cation will be minimized or even prevented if the cation is too strongly solvated. Typically, the solvation energy of alkali metal cations varies as the reciprocal of the ionic radius (Pedersen, 1967a). Table 1.1 shows the atomic and cationic radii of the alkali metals. In addition, Pedersen estimated, from two different models, the hole diameter of some common crown ethers. These data are catalogued in Table 1.2. Since the complexants play an integral part in solvating alkali metals, the list of only a few solvents available for the

formation of metal solutions, vital for alkalide/electride synthesis, is increased by several more.

Table 1.1
Alkali Metal Radii

Alkali metal	Cation radius (Å)	Atomic radius (Å)	VdW radius (Å)
Li	0.60	1.55	0.971
Na	0.95	1.90	1.287
K	1.33	2.35	1.592
Rb	1.48	2.48	1.674
Cs	1.69	2.67	1.774

Cryptands

Another group of complexants, collectively called cryptands (Lehn *et al.*, 1970), was also found to contain effective ligands. Coordination of alkali metal cations to the macrobicyclic cryptands occurs by a process in which the ligand encapsulates the cation, sometimes with a bicapped trigonal prismatic polyhedron. These complexes are finding increased use in the stabilization of uncommon oxidation states and they promote what were formerly considered to be improbable reactions. The first sodide was made by the reaction of Na metal with the cryptand [2.2.2], {(C222), where the numbers indicate the number of ethyl ether oxygens in each of the linkages to the two tertiary nitrogen atoms in the cryptand}.

The reaction was carried out in ethylamine ($EtNH_2$) followed by evacuation to high vacuum, to yield the $Na^+(C222)Na^-$ salt (Tehan *et al.*, 1974). The crystal structure revealed that the Na^- was located 5.55 Å away from the nearest nitrogen atom in the crypt and 5.16 Å away from the nearest oxygen atom. This observation indicated that Na^- is indeed a separate entity in the structure.

Table 1.2
Hole Diameters of Some Crown Ethers

Crown Ether	Hole Diameter (Å)
14-crown-4	1.2-1.5
15-crown-5	1.7-2.2
18-crown-6	2.6-3.2
21-crown-7	3.4-4.3

To summarize, the thermodynamics of the reaction is driven by the complexant which encapsulates the alkali metal cation. The addition of crown ethers or cryptands markedly increases the solubility of the alkali metals by shifting the equilibrium given by Eq. 1.4 to the right because of the strong complexation of the cation according to Eq. 1.5. The result is to greatly enhance the concentration of M^- in the saturated solution. When there is an excess of alkali metal present, the equilibrium positions of reactions 1.3, 1.4 and 1.5 determines the relative concentrations of M^- and

$e^-_{(solv)}$. When there are stoichiometric amounts of alkali metal and complexant, the equilibria given by Eqs. 1.3 and 1.5 determine the relative concentrations of M^- and e^-. It should be noted, however that the reaction,

$$M^+C + 2e^-_{solv} \rightleftharpoons M^-_{solv} + C \qquad (1.7)$$

can yield a mixture of e^-_{solv} and M^-_{solv} even when the stoichiometry is that of the electride. Reaction 1.7 is particularly important when M is Na.

The overall requirements for the complexing agents used in alkalide and electride synthesis are that they are strong enough complexants so that they will bind the cation better than the strongly polar solvent used in synthesis. In addition, these cyclic and bicyclic complexants should be kinetically resistant to reduction since their role is to encapsulate the alkali metal cation so that the electron released by Eq. 1.3 will either go into solution or attach to an alkali metal to form the metal anion in solution. Figure 1.1 represents three complexant classes that are commonly used in alkalide and electride syntheses.

First Electride Crystal Structure: $Cs^+(18C6)_2e^-$

After proper work-up procedures and depending on the stoichiometry and the solvent, the unpaired electron will either occupy the void spaces in the solid structure to yield an electride, or it may, form the

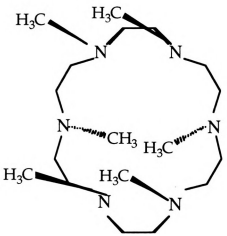

Hexamethyl hexacyclen
(HMHCY)

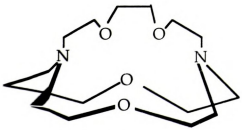

Cryptand [2.1.1]
(C211)

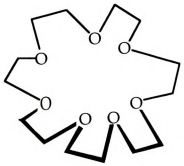

21-Crown-7 ether
(21C7)

Figure 1.1: Typical complexants used in the synthesis of alkalides and electrides.

alkali metal anion in solution and/or in the solid. In this specific case, when 18-crown-6 (18C6) is allowed to react with cesium metal in stoichiometric amounts in a suitable solvent under anaerobic conditions, two complexant molecules encapsulate the alkali metal cation to form a sandwich complex with twelve oxygens coordinated to Cs^+. This electride belongs to the monoclinic crystal system (Dawes *et al.*, 1986) and there are four molecules per unit cell. The Cs^+-e^- distances range from 7.71 to 9.40 Å. The lone pairs of electrons on the oxygen atoms in the ether unit of the crown, are oriented towards the positive ion, thus providing stability of the complex. The Cs^+-O distances range from 3.29 to 4.04 Å. The unpaired electron density is presumably centered at the void site formed by close-packing of eight complexed Cs cations. The ball and stick model (Figure 1.2) shows the structure of the complexed cation in this electride, $Cs^+(18C6)_2e^-$. This particular compound, called a *sandwich* electride since the alkali metal is completely encapsulated by two 18C6 molecules, is important in the EPR studies discussed at length later.

Localized and Delocalized Electrons

As a class, the behavior of the electrons in electrides can represent extremes, in which the trapped electrons may be localized or delocalized as evidenced by optical and conductivity studies. The optical spectrum of most electrides reveals a distinct peak in the near IR region, characteristic

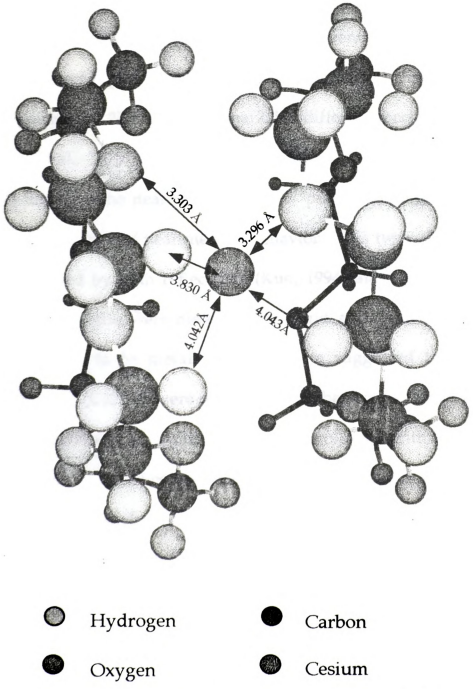

Figure 1.2: Ball and stick model of $Cs^{+}(18C6)_2e^{-}$. This *sandwich* molecule is comprised of two 18C6 molecules, one cesium cation and one isolated electron as the anion (not shown).

of electron localization and similar to that of trapped and solvated electrons (Thompson, 1976). However, solvent-free films formed by evaporation of liquid ammonia from a 1:1 mixture of potassium metal and cryptand [2.2.2], showed a remarkably different spectrum (Figure 1.3), (DaGue *et al.*, 1979). A continually rising absorption throughout the visible and into the near IR (a so-called "plasma edge") was observed, which is indicative of near-metallic behavior. This type of spectrum had been observed by both reflectance (Kuo, 1994) and transmission when alkali metals alone were dissolved in liquid ammonia at high enough concentrations to be metallic. These data suggested that either the electrons in $K^+(C222)e^-$ were delocalized or that very shallow traps were present. Furthermore, optical spectra were collected with thin films that had different ratios of complexant to metal. By adjusting this ratio, the optical data revealed varying amounts of trapped electrons. To confirm these findings, another experiment was done with K and C222 without the use of a solvent. Thin films of alkali metals and complexant were co-deposited on a sapphire substrate at -40° C , under high vacuum (10^{-8} torr) (Hendrickson, 1994). The same "plasma edge" was observed in the optical spectrum. In addition, the conductivity of the electride films indicated that defect electrons or holes might be responsible for the highly conducting nature of this compound. Initial microwave power absorption studies of powdered $K^+(C222)e^-$ prepared from $NH_{3(l)}$, suggested that

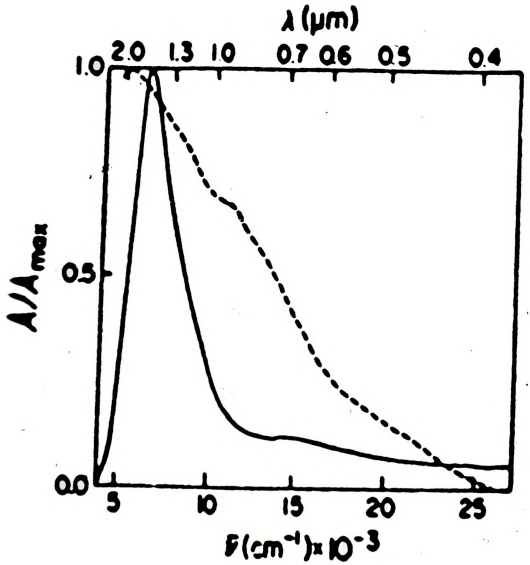

Figure 1.3: Optical aborption spectra of solvent free electride films. The solid line represents $Cs^+(18C6)2e^-$ and the dashed line represents $K^+(C222)e^-$.

$K^+(C222)e^-$ is metallic (DaGue *et al.*, 1979). This high microwave conductivity was confirmed by measuring the power absorbed by the crystalline samples (Moeggenborg *et al.*, 1991). Most electrides show little or no difference from an empty quartz tube, but $K^+(C222)e^-$ behaved as finely divided metal powders. This highly microwave conducting effect was also evidenced when high field EPR experiments in the far infrared region (250 GHz) were attempted*. The highly conductive nature of these samples did not permit a high enough transmission to obtain a signal.

Measurements made with a superconducting quantum interference device (SQUID) magnetometer, showed a decrease in the susceptibility as the temperature approached zero K, suggesting that there was either thermally induced electron pair dissociation or the population of a triplet state (Huang *et al.*, 1988). If the triplet state were populated, the energy level difference could be probed by using EPR techniques. EPR studies of photoexcited or thermally excited $K^+(C222)e^-$ and $K^+(C222)K^-$ were attempted but the results did not indicate any changes in triplet sub-level populations, if they exist, as no changes in the EPR spectra were observed after photoexcitation (Figure 1.4)†. In addition, there was no evidence of the $\Delta m_s = \pm 2$ transition or half-field line, which is often present in the EPR spectra of triplets. After some DC powder conductivity experiments

*Unpublished results from a collaboration with the Freed lab at Cornell University, Reidy-Cedergren *et al.*, 1993.
†Unpublished results in this lab, Reidy-Cedergren *et al.*, 1992.

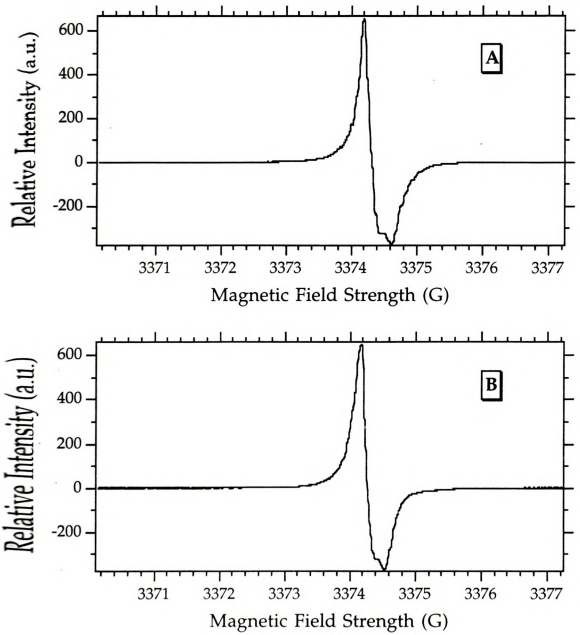

Figure 1.4: (A.) cw-EPR spectrum of $K^+(C222)e^-$ collected at 100 K, 0.04 G/pp modulation amplitude, 6.3e3 gain, 200 ms. time constant, 200 s. sweep time, 100 kHz modulation frequency, 9.4562 GHz microwave frequency. (B.) same as (A.) after photoexcitation with an 800 W projection lamp. The relative intensities of the two spectra are within experimental error of each other and no significant lineshape changes exist indicating no excitation into a triplet sublevel

showed activated conductivity (Moeggenborg *et al.*, 1991), it appeared that this electride was not, in fact, metallic but instead contained bound electrons with a very small band gap. The possibility that the barriers to electron movement were small, was considered.

The most recent optical and conductivity measurements made on films that were prepared with full stoichiometric and temperature control, suggested that *partial* decomposition of the films actually leads to an *increase* in conductivity. The conductivity either remains constant or increases until about one half of the material is decomposed at which point the electride rapidly becomes insulating (Hendrickson, 1994). These recent and surprising results coupled with those obtained previously, suggest that the conductivity is due to missing electrons or holes. According to this view, the pure electride is actually an insulator but even small quantities of defect holes can cause high conductivities. This lengthy chain of events illustrates the complexity that can be encountered with both alkalides and electrides.

The chemical and physical properties of alkalides and electrides are dependent on the nature of the trapping sites. The magnetic behavior can be probed by using magnetic resonance techniques. Isolated trapped electrons are paramagnetic, so EPR can be used to probe the charge distribution around the trapping sites. However, little information is gained just from EPR experiments with pure electrides. Because the

electron sites are so close together, rapid electron exchange can occur on the EPR time scale, resulting in an exchange narrowed line. Therefore, usually a single featureless line is observed. This is the case for most electrides; however, the electride $Li^+(C211)e^-$ exhibits lineshape changes with temperature that will be discussed at length in a later chapter.

Trapped Electrons

To avoid the dilemma of featureless EPR lineshapes, one turns to the "cousin" of electrides, alkalides. Magnetic susceptibility and EPR studies have shown that paramagnetic species almost always are present in these polycrystalline materials. The reason for this is the presence of defect trapped electrons in anionic vacancies in the alkalide crystals. Since alkalides are crystallized from solutions that contain alkali metal anions but also usually solvated electrons, electron trapping still occurs. Depending on the metal, solvent and the synthesis method, the concentration of defect electrons varies from sample to sample. Pure alkalides are intrinsically diamagnetic since they contain an alkali metal cation with an ns^o electron configuration (M^+) and an alkali metal anion with an ns^2 electron configuration (M^-). These materials, if pure would be EPR silent, but since there are trapped defect electrons at the anionic vacancies, an EPR resonance can nearly always be observed. In these crystallites, the electrons are much more separated than in pure electrides

so the problem of exchanged narrowed EPR lines is avoided. What is the nature of these trapping sites? These defect electrons occupy holes, (anionic sites) and such electron-occupied holes are called F-centers (Figure 1.5). The electrons in F-centers can generally be thermally excited to a conduction band, thus giving rise to an n-type semi-conductor. Another type of defect electron that could be present in these systems is an interstitial or Fraenkel defect (Figure 1.6). Initial studies indicated that both photoelectron emission and thermionic emission from alkalides and electrides resulted from the presence of weakly bound electrons. It was thought that the ground state of electrides or of electrons in F-centers in alkalides might lie very close to the vacuum level (Huang & Dye, 1990). However, more recent studies have shown that the most likely candidates for thermionic emission are defect electrons in shallow traps with energies near the vacuum level, produced by photo-excitation or other processes (Kuo, 1994).

One of the major aims of this research is to describe the nature of these trapping sites. Because of the wide range of behavior of the magnetic properties of electrides and alkalides, as well as their optical and electronic properties, these compounds can provide a probe to determine the nature of interactions of weakly bound electrons with each other and with surrounding ions and molecules. While the use of EPR methods can provide some insight into the nature of electron trapping sites, double

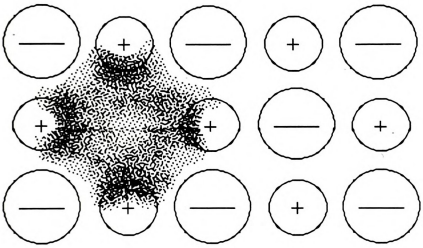

Figure 1.5: Picture of an *F-center* where the electron density occupies the anionic vacancy.

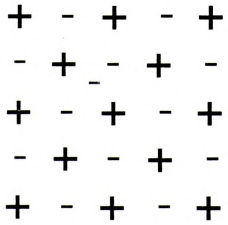

Figure 1.6: An *Interstitial Ion (Fraenkel defect)* is a distortion ina point because there is an atom in a position where it does not belong.

resonance techniques such as electron spin echo envelope modulation (ESEEM), and electron nuclear double resonance (ENDOR) can take on the challenge of mapping the unpaired electron density at various nuclei and the nature of the inter-electron coupling. These topics will be addressed in depth in a subsequent chapter.

The First Alkalide

The most extensively studied alkalide to date is $Na^+(C222)Na^-$ mainly because of its remarkable stability relative to the other alkalides and electrides. Even though most of these ionic salts are sensitive to air, moisture, temperature, and to certain reducing agents, $Na^+(C222)Na^-$ is stable under vacuum for several days at room temperature and indefinitely at low temperature. However, as with all alkalides and electrides, it is thermodynamically unstable towards decomposition. Crystalline alkalides and electrides are subject to an irreversible decomposition process that results from cleavage of the C-O ether bond (Cauliez *et al.*, 1991) as the temperature is raised. The decomposition usually accelerates at around 0°C although this is dependent upon the system. $Na^+(C222)Na^-$ crystals have a very brilliant gold-copper color resembling a metal. Surprisingly, it is not a metal but an intrinsic semiconductor with an apparent band gap of 2.4 eV. EPR studies (DeBacker *et al.*, 1990) as well as magnetic susceptibility studies (Jaenicke & Dye, 1984)

show that the pure $Na^+(C222)Na^-$ material is only weakly paramagnetic, whether in the form of a powder, thin film or microcrystal. The effect of light was studied by recording the EPR spectrum while the sample was illuminated in the cavity (DeBacker *et al.*, 1990). Illumination of the sample was provided by a 150 W tungsten lamp which was focused directly on the grid of the EPR cavity. Unfiltered visible light (UV excluded) or 630 nm light, produced an increase in the EPR signal. The results from the EPR measurements showed only the photoproduction of a low concentration of paramagnetic species. The *g*-value was measured to be 2.005 which is close to that of trapped electrons in solids of this type and no other paramagnetic species were observed. The lifetime at room temperature of the paramagnetic species was long, with a half-life of about 30 seconds. The formation of EPR active material was thought to be due to the dissociation of defect electron pairs which were present before illumination of the $Na^+(C222)Na^-$. Optical data have accumulated over the years and while the system is becoming better understood, a quantitative description is not yet complete. The optical data show a typical absorption at 670 nm indicating Na^-. In addition, the presence of a shoulder on the high energy side of the Na^- peak could be attributed to excitation of an electron from the ground $3s^2$ state of Na^- to the broad conduction band (Hendrickson, 1994, Hendrickson *et al.*, 1996). Upon

photolysis with high intensity laser pulses, two additional bands are observed. One possible explanation for these features is that Na^- transfers energy to two unknown bands, one at a low energy and one at a high energy. It is believed that Na atoms or a sodium film are responsible for the higher energy peak and trapped electrons give rise to the low energy peak. If sodium atoms were responsible, it seems likely that the Na atoms would recombine with the electron to form Na^-. Also, if Na atoms are present, they would have to be immobilized. EPR measurements of irradiated samples show no evidence for Na atoms. Another possibility is that a uniform film of Na metal could be forming but this also should result in the formation of $Na^+(C222)Na^-$ since this is how it is produced to begin with! Only if a conformational change occurred upon irradiation would the recombination be slow. Finally, it is possible that an exotic new species is being formed that consists of an electron pair trapped for every Na^+ trapped. Current experiments are in progress to help understand the behavior upon photolysis.

Important Theoretical Considerations

Over the years, because of the unconventional nature of these compounds, there has been considerable scrutiny of the alkalides and particularly the electrides from a theoretical point of view. The current hypotheses stem from the experimental findings; however, theoretical

conclusions that agree with these hypotheses have been questioned (Golden & Tuttle, 1988) but with highly doubtful arguments.

The experimental data suggest that electrides are ionic compounds with most of the unpaired electron density located outside of the complexed cation. Various theoretical treatments and models have been used to describe electrides, particularly $Cs^+(18C6)_2e^-$ and $Cs^+(15C5)_2e^-$. Given the knowledge of the crystal structure, and therefore the location of the atoms, the dimensions of the electron traps can be obtained by modeling the atoms as van der Waals spheres. Experimental evidence from nuclear magnetic resonance (NMR) studies revealed that the atomic character on the Cs atom of the $Cs^+(18C6)_2e^-$ is only 0.033% (Dawes, 1986, Dawes *et al.*, 1987). This indicates that the 6s electron density originally centered on the cesium nucleus has a much smaller density at the Cs nucleus in the electride. These conclusions were based on the magic angle spinning (MAS) NMR spectrum, which consists of one peak, paramagnetically shifted to +81 ppm from that of other $Cs^+(18C6)_2$ compounds (Dawes *et al.*, 1987). This effect is more readily explained by contact with the unpaired electron rather than a tight coordination of Cs^+ by the 18C6 molecule. The paramagnetic shift is derived from the Knight or contact shift that results from strong local magnetic fields, generated from paramagnetic electron density at the cesium nucleus, and is given by,

$$K(T) = (8\pi/3N_A)<|\psi(0)|^2>\chi(T) \qquad (1.10)$$

where N_A is Avagadro's number, $<|\psi(0)|^2>$ is the average electron density at the nucleus, and $\chi(T)$ is the molar magnetic susceptibility. From Eq. 1.10 and the measured temperature dependence of the chemical shift and susceptibility, the contact electron density for $Cs^+(18C6)_2e^-$ was calculated to be $8.75x10^{21}$ cm^{-3}. The 6s orbital has non-zero electron density at the nucleus, and is the lowest energy occupied orbital in the atom. The fractional atomic character, F, can thus be calculated from,

$$F = <|\psi(0)|^2> / <|\psi(0)|^2>_{atom} \qquad (1.11)$$

where $<|\psi(0)|^2>_{atom}$ is the electron density at the nucleus for an isolated gas atom, which is $2.645x10^{25}$ e cm^{-3} (Edwards & Sienko, 1982). Therefore, $8.75x10^{21}$ $cm^3/2.645x10^{25}$ cm^{-3} = $3.3x10^{-4}$ or 0.033%. To put this number into perspective, the percent atomic character of the gaseous cesium atom is 100%, that of cesium metal is 59%, cesium dissolved in isopropylamine is 27% and in cesium-ammonia solutions it is 3-8%, depending on concentration (Dawes *et al.*, 1987, Edwards & Sienko, 1982). The positive charge on cesium seems to be very well shielded by its interactions with the lone pairs of electrons on the crown ether oxygens. The low percent atomic character has been attributed to the location of the electron density, presumably in or around the anionic vacancy. In addition, a strong

coulombic attraction to eight nearest neighbor complexed cesium cations helps to localize the electron charge (Dawes *et al.*, 1987). The overall electron density in the electride was determined to be $1.1x10^{21}$ $e{\cdot}cm^{-3}$ at 216K. These results triggered theoretical interest from Golden and Tuttle (Golden & Tuttle, 1992). They disputed Dawes' interpretation of the contact density at the Cs nucleus. After further examination of the ^{133}Cs NMR results and from their hypothesis of electron distributions, they claimed that this number is consistent with the assumption that the maximum electride electron density is simply in the very near proximity of the Cs nucleus.

Allan and co-workers (Allan *et al.*, 1990) tried to reason the stability of the unconventional situation given by electrides by using self-consistent tight binding Hartree-Fock calculations. They found that the complexed Cs cation is repulsive to the excess electron while the holes in the structure yield an attractive potential. They also found that the calculated trapped electron wave function was vanishingly small at the Cs site, which agrees with the very small percent atomic character determined from NMR results. These results are directly contradictory to the conclusions of Golden and Tuttle.

Another group of theoreticians (Renscok *et al.*, 1993) also refuted the arguments described by Golden and Tuttle. Initially, the question of

charge isolation was addressed by this group. Their calculations sought to answer the conundrum of why the electron density at the cesium cation is so small when the electronic wave function, presumably centered in the trap, should be able to penetrate into the complex and have a higher density at the cation than is observed. They surmised that since the oxygen atoms are in van der Waals contact with the Cs^+, the crowns are permanently polarized since the oxygens are negative and the hydrogens are positive. This charge distribution could possibly form a potential barrier to an electron between the inside of the complexed cation near the Cs, and the outside. The calculations led the authors to the conclusion that most of the unpaired electron density was moved outside of the complexed Cs cation radius. The model presented by Rencsok represents only the isolated molecule; nevertheless it supports the conclusion derived from the experimental evidence that the unpaired electron density in the cavity is separated from the cation. They also provided convincing evidence to refute the arguments of Golden and Tuttle [Rencsok, 1995 #405]. In addition, high level quantum calculations and interesting results and pictures were reported by these authors on the unpaired electron density distribution in the smaller (and fictitious) electride molecule $Li^+(9C3)_2e^-$ (Rencsok *et al.*, 1993).

Another theoretical treatment that is independent of the others referenced here, consisted of local density approximation (LDA)

calculations (Singh *et al.*, 1993). These *ab initio* self consistent calculations were carried out on $Cs^+(15C5)_2e^-$. The behavior of the self consistent potential surprisingly revealed that the electron's potential energy at the center of the cavity was a maximum and not a minimum, but the total energy, potential plus kinetic, was a minimum. One usually assumes that the electron seeks a potential energy minimum; thus, according to this conclusion, electrides are an exception. Interaction with the core electrons of the cation and the complexant electrons consistent with the Pauli exclusion principle, along with the space available at the vacancy combine to trap the electron in the region of the potential energy maximum. The total energy is minimized by spreading the electron density throughout the large cavity thereby reducing its kinetic energy.

An Overall Message...

The major take-home lesson is that isolated complexed cation structure stabilizes the solid, preventing recombination with the trapped electron. We believe that, to a first approximation, the electride electrons should be treated as if they are distinct from all other electrons in the electride, just as is usually done with F-center systems, metals and solvated-electron systems. The motivation behind the research described in this thesis stems from this notion and from the desire to acquire experimental evidence to help clarify various explanations of electride

behavior. However, because of the extreme difficulty of viewing the trapped electrons in the electride directly by X-ray diffraction, we can only put forth our best efforts to lend support to the idea that the unpaired electron density does move away from the complexed cation and into the cavity.

The compilation presented in this chapter touches on only some of the issues inspired by alkalide and electride research. Professor Dye has changed the way that scientists think about chemistry, given the chemical significance of the research. Not only is there a unique situation to learn and to characterize a new class of compounds, but there are potentially important uses for these compounds. For example, alkalides and electrides are exceptional reducing agents and have been used to prepare nanoscale particles of metals and alloys (Tsai & Dye, 1993). They are also enticing where very strong reducing agents are necessary, as occurs occasionally in organic synthesis. What has been learned over the years from alkalide and electride research has been used to develop new compounds, similar in nature, for potentially important use. For example, this lab and others have attempted to produce large organic globular electron acceptors (LOGEAs). Echegoyen and co-workers (Echegoyen *et al.*, 1991) introduced the prototype of such compounds called *cryptatiums*. The lowest unoccupied molecular orbital (LUMO) of these molecules are at low energies, so that there is a potential for adding extra electrons to the

system. The driving force of research on LOGEAs is the possibility of producing materials that are superconducting. For the last few years, many of us in the Dye group as well as other collaborative groups, have tried to synthesize organic superconductors, by using the techniques developed in alkalide and electride research, but we have so far obtained only hints of superconductivity that probably results from other causes. The Dye research group will continue to face more challenges and to learn more chemistry.

Finally, it is worthwhile to list the current alkalides and electrides synthesized in the Dye group, together with their crystal systems (Table 1.3).

Table 1.3
Current Structural Data of Alkalides and Electrides

Compound	Crystal System	ref	Compound	Crystal System	ref
$Cs^+(18C6)_2e^-$	Monoclinic	a	$Rb^+(18C6)Rb^-$	Monoclinic	l
$Cs^+(15C5)_2e^-$	Triclinic	b	$Cs^+(C222)Cs^-$	Monoclinic	i
$Li^+(C211)Na^-$	Orthorhombic	j	$K^+(HMHCY)Na^-$	Orthorhombic	p
$Na^+(C222)Na^-$	Rhombohedral	c	$Rb^+(HMHCY)Na^-$	Orthorhombic	r
$Na^+(C221)Na^-$	Monoclinic	d	$Cs^+(HMHCY)Na^-$	Orthorhombic	p
$K^+(C222)Na^-$	Orthorhombic	e	$Rb^+(18C6)Na^-$ $MeNH_2$	Orthorhombic	j
$K^+(12C4)_2Na^-$	Monoclinic	d	$K^+(18C6)(12C4)Na^-$	Orthorhombic	o
$Rb^+(15C5)_2Na^-$	Monoclinic	f	$K^+(18C6)(12C4)K^-$	Orthorhombic	o
$Cs^+(18C6)_2Na^-$	Monoclinic	f	$K^+(18C6)(12C4)K^-$ $.(18C6)$	Monoclinic	o
$Cs^+(15C5)_2Na^-$	Triclinic	g	$Li^+_2(TMTCY)_2$ $(MeNH)Na^-$	Orthorhombic	q
$Cs^+(15C5)_2K^-$	Monoclinic	h	$Li^+_2(TMTCY)$ $(DMTCY)^-$ $MeNH_2Na^-$	Orthorhombic	s
$Rb^+(15C5)_2Rb^-$	Monoclinic	h	$Li^+(18C6)Na^-$ $(MeNH_2)_2$	Monoclinic	q
$Cs^+(18C6)_2Cs^-$	Orthorhombic	i	$Li^+(18C6)Na^-$ $(MeNH_2)_2.(18C6)_3$	Rhombohedral	q
$Li^+(C211)e^-$	Orthorhombic	j	$K^+(18C6)Na^-$ $(MeNH_2)_2.(18C6)_3$	Rhombohedral	d
$K^+(C222)e^-$	Monoclinic	k	$Rb^+(C222)Rb^-$	Triclinic	l
$K^+(C222)K^-$	Triclinic	l	$Cs^+(21C7)Na^-$	Triclinic	t
$Cs^+(15C5)$ $(18C6)e^-$	Rhombohedral	m	$Cs^+(C322)Na^-$	Monoclinic	d
$Li_2^+(TMPAND$ $Na^-)_2(MeNH_2)$	Monoclinic	d	$Rb^+(12C4)(18C6)$ Na^-	Monoclinic	o
$Li^+(C211)Cs^-$	Monoclinic	n	$K_2^+(21C7)Na_2^-$ $MeNH_2$	Monoclinic	t
$Rb^+(12C4)(18C6)$ Rb^-	Orthorhombic	o			

References correspond to the following:

a. (Dawes *et al.*, 1986)
b. (Ward *et al.*, 1990b).
c. (Tehan *et al.*, 1974).
d. (Huang & Dye, 1996a)
e. (Ward *et al.*, 1990a).
f. (Dawes *et al.*, 1989).
g. (Huang & Dye, 1996a)
h (Ward *et al.*, 1990a)
i. (Huang *et al.*, 1987).
j. (Huang *et al.*, 1996b)
k. (Huang *et al.*, 1988).
l. (Huang *et al.*, 1989)
m. (Wagner *et al.*, 1994)
n. (Huang *et al.*, 1996a)
o. (Huang, 1994a)
p. (Kuchenmeister & Dye, 1989)
q. (Huang & Dye, 1996b)
r. (Huang, 1994a)
s. (Huang *et al.*, 1990)
t. (Huang, 1994)

BIBLIOGRAPHY

Allan, G., DeBacker, M. G., Lannoo, M., & Lefebvre, J. (1990) *Europhysics Letters 11*, **Why Do the Electrons Play the Role of Anions in the Electrides?**, 49-53.

Cauliez, P. M., Jackson, J. E., & Dye, J. L. (1991) *Tetrahedron Letters 32*, **An Unusual Reduction of Ethylene Occurring during the Thermal Decomposition of Alkalides and Electrides**, 5039-5042.

DaGue, M. G., Landers, J. S., Lewis, H. L., & Dye, J. L. (1979) *Chemical Physics Letters 66*, **Alkali Metal Anions and Trapped Electrons Formed by Evaporating Metal-Ammonia Solutions which Contain Cryptands**, 169-172.

Dawes, S. B., **Structural and Magnetic Properties of the Electrides of Cesium Complexed by 15-crown-5 and 18-crown-6.**, 1986.

Dawes, S. B., Ellaboudy, A. S., & Dye, J. L. (1987) *Journal of the American Chemical Society 109*, **Cesium-133 Solid State Nuclear Magnetic Resonance Spectroscopy of Alkalides and Electrides**, 3508-3513.

Dawes, S. B., Ward, D. L., Fussa-Rydel, O., Huang, R.-H., & Dye, J. L. (1989) *Inorganic Chemistry 28*, **Crystal Structures and Properties of Two Sodides and an Electride**, 2132-2136.

Dawes, S. B., Ward, D. L., Huang, R. H., & Dye, J. L. (1986) *Journal of the American Chemical Society 108*, **First Electride Crystal Structure**, 3534-3535.

DeBacker, M. G., Mkadmi, E. B., Sauvage, F. X., Lelieur, J. P., McMills, L. E. H., Eglin, J. L., Kim, J., Guadagnini, R., Wagner, M., Concepcion, R., & Dye, J. L. (1994) *Journal of the American Chemical Society 116*, **Lithium-Ethylamine and Lithium-Sodium-Ethylamine Systems: A Nonmetallic Liquid Electride and the Lowest Melting Fused Salt**, 6570-6576.

DeBacker, M. G., Sauvage, F. X., & Dye, J. L. (1990) *Chemical Physics Letters 73,* **Interaction of Light with $Na^+C222\ Na^-$. A Laser Flash Photolysis and EPR Investigation,** 291-297.

Dye, J. L. (1977) *Scientific American 237,* **Anions of the Alkali Metals,** 92-105.

Dye, J. L. (1979) *Angewandte Chemie International Edition in English 18,* **Compounds of Alkali Metal Anions,** 587-598.

Dye, J. L. (1987) *Scientific American 257,* **Electrides,** 66-75.

Dye, J. L. (1991) in *Metals in Solution, Journal de Physique IV, Colloque C5* (Damay, P., & Leclerq, F., Eds.) pp 259-282, Les Editions de Physique, Les Ulis, France.

Dye, J. L. (1993) *Chemtracts-Inorganic Chemistry 5,* **Alkalides and Electrides,** 243-270.

Dye, J. L., & Ellaboudy, A. (1984) *Chemistry in Britain 20,* **Crystalline Alkalides and Electrides,** 210-215.

Echegoyen, L., DeCian, A., Fischer, J., & Lehn, J.-M. (1991) *Angewandte Chemie International Edition in English 30,* **Cryptatium: A Species of Expanded Atom/Radical Ion Pair Type from Electroreductive Crystallization of the Macrobicyclic Sodium Tris (Bipyridine) Cryptate,** 838-840.

Edwards, P. P., & Sienko, M. J. (1982) *Accounts of Chemical Research 15,* **The Transition to the Metallic State,** 87-93.

Golden, S., & Tuttle, T. R., Jr. (1988) *Journal of the Chemical Society Faraday Transactions 84,* **Spectral-Moment Constrained Density Matrices of Maximum Entropy for the Solvated Electron,** 1913-1922.

Golden, S., & Tuttle, T. R., Jr. (1992) *Physical Review B 45,* **Spectral-Moment Constraints on Electride-Electron Locations in the Crystalline Electride [Cs(18-Crown-6)$_2$],** 913-918.

Greenwood, N. N., & Earnshaw, A. (1984) **Chemistry of the Elements,** Vol. 75-110, Pergamon Press, New York.

Hendrickson, J. E., **Optical and Electrical Properties of Vapor-Deposited Thin Films of a Sodide and an Electride**, 1994.

Hendrickson, J. E., Xu, G., Pratt, W. P., Jr., & Dye, J. L. (1996) *Manuscript in preparation*, **Photolysis of Na^+(Cryptand[2.2.2])Na^-: Photobleaching of Absorbance and Quenching of Fluorescence**, .

Huang, R. H., & Dye, J. L. (1990) *Chemical Physics Letters 166*, **Low Temperature (-80°C) Thermionic Electron Emission from Alkalides and Electrides**, 133-136.

Huang, R. H., & Dye, J. L. (1996a) *unpublished results.*

Huang, R. H., & Dye, J. L. (1996b) *Manuscript in preparation*, **Synthesis and Structure of Five Compounds that Contain the Sodium Anion**, .

Huang, R. H., Faber, M. K., Moeggenborg, K. J., Ward, D. L., & Dye, J. L. (1988) *Nature (London) 331*, **Structure of K^+(Cryptand[2.2.2]) Electride and Evidence for Trapped Electron Pairs**, 599-601.

Huang, R. H., Wagner, M. J., & Dye, J. L. (1996a) *unpublished results.*

Huang, R. H., Wagner, M. J., Gilbert, D. J., Reidy-Cedergren, K., Ward, D. L., Faber, M. K., & Dye, J. L. (1996b) *Submitted for Publication*, **Synthesis, Structure and Properties of the "Spin-Ladder-Like" Electride, Li^+(Cryptand[2.1.1])e^-**, .

Huang, R. H., Ward, D. L., & Dye, J. L. (1989) *Journal of the American Chemical Society 111*, **Alkali-Metal-Anion Dimers and Chains in Alkalide Structures**, 5707-5708.

Huang, R. H., Ward, D. L., & Dye, J. L. (1990) *Acta Crystallographica C46*, **Structures of Alkalides and Electrides. IV. Structure of Li^+(TMTCY)[Li^+(DMTCY$^-$)·CH_3NH_2]Na^-**, 1835-1837.

Huang, R. H., Ward, D. L., Kuchenmeister, M. E., & Dye, J. L. (1987) *Journal of the American Chemical Society 109*, **The Crystal Structures of Two Cesides Show That Cs^- is the Largest Monatomic Ion**, 5561-5563.

Huang, S., **Single Crystal X-ray Diffraction and Alkali Metal NMR Studies of Alkalides, Electrides and Model Compounds**, 1994.

Jaenicke, S., & Dye, J. L. (1984) *Journal of Solid State Chemistry 54*, **Photoelectron Emission from Solid Sodides**, 320-329.

Kaplan, T. A., Rencsok, R., & Harrison, J. F. (1994) *Physical Review B 50*, **Valence-electron distribution of cesium crown-ether electrides.**, 8054-8058.

Kevan, L. (1981) *Accounts of Chemical Research 14*, **Solvated Electron Structure in Glassy Matrices.**, 138-145.

Kraus, C. A. (1907) *The Journal of the American Chemical Society 29*, **Solutions of metals in non-metallic solvents.**, 1557-1571.

Kraus, C. A., & Lucasse, W. W. (1921) *The Journal of the American Chemical Society 43*, 2529.

Kraus, C. A., & Lucasse, W. W. (1922) *The Journal of the American Chemical Society 44*, 1941.

Kuchenmeister, M. E., & Dye, J. L. (1989) *Journal of the American Chemical Society 111*, **Synthesis and Structures of Two Thermally Stable Sodides with the Macrocyclic Complexant Hexamethyl Hexacyclen**, 935-938.

Kuo, C.-T., **Optical Studies of Alkalides and Electrides**, 1994.

Lehn, J.-M., Sauvage, J. P., & Dietrich, B. (1970) *Journal of the American Chemical Society 92*, **Cryptate Cation Exchange Rates**, 2916-2918.

Moeggenborg, K. J., Papaioannou, J., & Dye, J. L. (1991) *Chemistry of Materials 3*, **Powder Conductivities of Three Electrides**, 514-520.

Mott, N. F. (1956) *Canadian Journal of Physics 34*, 1356.

Patterson, T. A., Hotop, H., Kasdan, A., Norcross, D. W., & Lineberger, W. C. (1974) *Physical Review Letters 32*, 189-92.

Pedersen, C. J. (1967a) *Journal of the American Chemical Society 89*, **Cyclic Polyethers and their Complexes with Metal Salts**, 2495-2496.

Pedersen, C. J. (1967b) *Journal of the American Chemical Society 92*, **New Macrocyclic Polyethers.**, 391-394.

Pedersen, C. J. (1970) *Journal of the American Chemical Society 92*, **Crystalline Salt Complexes of Macrocyclic Polyethers.**, 386-394.

Pedersen, C. J. (1988) *Science 241*, **The Discovery of Crown Ethers**, 536-539.

Rencsok, R., Kaplan, T. A., & Harrison, J. F. (1993) *Journal of Chemical Physics 98*, **Electronic Structure of Li(9-crown-3)$_2$: A Molecule with a Rydberg-type Ground State**, 9758-9764.

Singh, D. J., Krakauer, H., Haas, C., & Pickett, W. E. (1993) *Nature (London) 365*, **Theoretical Determination that Electrons Act as Anions in the Electride Cs$^+$(15-crown-5)$_2$e$^-$**, 39-42.

Tehan, F. J., Barnett, B. L., & Dye, J. L. (1974) *Journal of the American Chemical Society 96*, **Alkali Anions. Preparation and Crystal Structure of a Compound Which Contains the Cryptated Sodium Cation and the Sodium Anion**, 7203-7208.

Thompson, J. C. (1976) **Electrons in Liquid Ammonia**, Vol. , Oxford Univ. Press, Oxford.

Tsai, K.-L., & Dye, J. L. (1993) *Chemistry of Materials 5*, **Synthesis, Properties, and Characterization of Nanometer-Size Metal Particles by Homogeneous Reduction with Alkalides and Electrides in Aprotic Solvents**, 540-546.

Wagner, M. J., & Dye, J. L. (1993) *Annual Review of Materials Science 23*, **Alkalides, Electrides and Expanded Metals**, 223-253.

Wagner, M. J., Huang, R. H., Eglin, J. L., & Dye, J. L. (1994) *Nature(London) 368*, **An Electride with a Giant 6-Electron Ring**, 726-729.

Ward, D. L., Huang, R. H., & Dye, J. L. (1990a) *Acta Crystallographica C 46*, **Structures of Alkalides and Electrides. V. Structure of Caesium Bis(15-Crown-5) Kalide and Rubidium Bis(15-Crown-5) Rubidide**, 1838-1841.

Ward, D. L., Huang, R. H., Kuchenmeister, M. E., & Dye, J. L. (1990b) *Acta Crystallographica C46*, **Structures of Alkalides and Electrides. II. Structure of Cesium Bis(15-Crown-5) Electride**, 1831-1833.

Weyl, W. (1864) *Annalen der Physik und Chemie 19*, 7601.

CHAPTER 2

SYNTHESIS OF CESIUM HEXAMETHYL HEXACYCLEN SODIDE:

$Cs^+(HMHCY)Na^-$

INTRODUCTION

Preparation of alkali metal solutions, alkalides and electrides would not be as tedious if the highly reactive nature of the solvated or trapped electron and alkali metal anions did not exist. Oxygen, water, alcohols and other reducible substances must be kept out of the reaction vessel. Furthermore, the reaction vessel must be immersed in a cold bath at temperatures around -40°C during synthesis and kept cold during use and storage of the alkalides and electrides. Presumably, the reason for this is that the complexants and solvents are themselves reducible substances. This ultimately leads to decomposition of the solid or solution. A solvent such as dimethyl ether (Me_2O) is a preferred solvent because of its resistance to reduction. Since dimethyl ether does not have ionizable protons or protons that are beta to the oxygen, this leads to resistance to reduction, resulting in a very robust solvent. Primary and secondary amines have ionizable protons, thus making them less desirable. Trimethylamine (TMA) and, to some extent, diethyl ether (Et_2O), even though it has beta hydrogens, also maintain a resistance towards reduction, and these two solvents serve as suitable co-solvents. In the case

where the alkalide dissolves in both of these solvents, n-pentane serves as a reasonable substitute. The combination of Me_2O and TMA however, provides the greatest resistance to reduction.

It was shown from gas phase NMR (Cauliez *et al.*, 1991) of the decomposed products of crown ether alkalides that the products are butane, ethane, ethylene and ring opened complexant minus the ethylene linkage. The oxygen atoms in the crown ether are highly electronegative and when there is a cation complexed to the oxygens, they become even more electronegative and form a strong dipole. This makes them very susceptible to attack by an electrophilic substance; thus, when the conditions are not right to stabilize the alkalide, the ring opens and the decomposition products are formed. In the case of HMHCY , all of the oxygens are replaced with nitrogens which are fully methylated, so there is no place for the electrophile to attack. This results in decomplexation rather than decomposition. When this occurs, the alkali metal cation that was complexed with the HMHCY recombines with the unpaired electron to form a fine metallic powder. This is evidenced in the HMHCY synthesis occasionally and must be avoided as the alkali metal also has an unpaired electron and will be observed in the EPR. To avoid this, the synthesis is completed in a speedy fashion, at a low enough temperature to prevent decomplexation but with enough care to grow crystals.

Preparation of $Cs^+(HMHCY)Na^-$

The glassware used to synthesize these compounds is very specific and it cannot be purchased, therefore it is glassblown in our glass shop. The cell, referred to as a K-cell, is shown in Figure 2.1. When synthesizing an alkalide, a Pyrex K-cell is used since the threat of exchanging the natural Na^+ in the borosillicate glass of Pyrex with cesium cation in the presence of M^- is minimal. Initially, the K-cell is cleaned rigorously to inhibit solution decomposition. The apparatus is first rinsed with a carefully prepared HF solution (5% concentrated HF, 35% concentrated HNO_3, 60% H_2O and a small amount of detergent) to remove contaminants from the walls of the glass. However, the soapy HF solution itself often is difficult to rinse away completely so an *aqua regia* solution composed of three parts HCl and one part HNO_3 is added to the vessel. This is allowed to stand for one day. The following day, the solution is poured out and washed six times with distilled water, followed by six rinses with conductance water, distilled water that had been deionized and redistilled through a high reflux ratio column so that less than 1 ppm of impurity remained. The K-cell is then placed in an oven at around 275°C to dry completely. Finally the K-cell apparatus is placed on the vacuum line overnight, with the proper 9 mm Ultra-Torr attachments at points 1 and 2, and evacuated to check for any faults in the glass as well

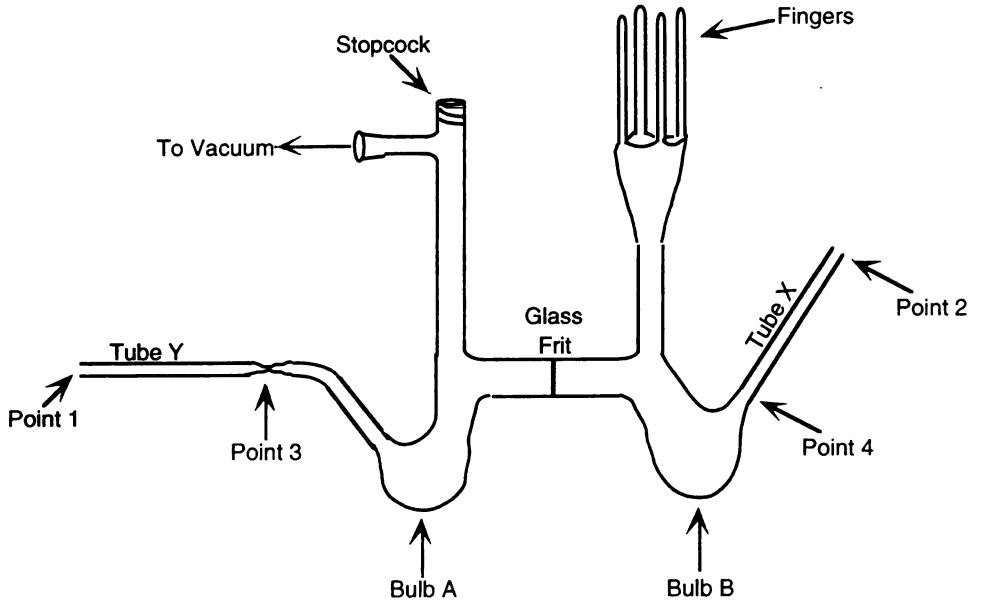

Figure 2.1: Pyrex® K-Cell used in the synthesis of alkalides and some electrides.

as to distill out any water that possibly remained in the K-cell. As is evident from this description, the cleaning ritual is very important and takes time and patience, so planning an experiment ahead of time is always advantageous.

Once the K-cell has been cleaned and could sustain a vacuum on the order of 10^{-6} torr, the K-cell, the appropriate length of a Cs metal ampoule†, a pipette and bulb, and a spatula are all placed in the Vacuum Atmosphere Company (VAC) Glove Box outer chamber to be evacuated to about 30 mtorr. Once the outer chamber has been evacuated, the equipment can be accessed through the port and brought into the glove box. The cesium ampoule is scored with a knife that is stored in the glove box and cracked. The portion of the cracked ampoule containing the metal is placed into tube Y so that the sealed part of the ampoule is facing towards the inside of the apparatus (this was done to help prevent any bumping of the cesium metal when it is distilled). If the ampoule is cracked in the middle of the Cs metal portion, both parts were placed in the side tube. The sodium metal and a knife to cut it is stored in the glovebox. A small portion of the metal is cut away to reveal a shiny unoxidized portion of the metal and some of the shiny metal is cut and

† To determine the appropriate length of cesium metal ampoule for each experiment, the conversion (85 mg/cm)(length of Cs ampoule in cm)(mmol/132.9mgCs)= mmol Cs, when the Cs metal is poured into 4 mm O.D. Pyrex® tubing.

weighed. The sodium is then placed in the refrigerator momentarily to cool the metal so that it will not stick to the walls of the sidearm during delivery into the K-cell. The Ultra-Torr attachment is then placed securely on the end of the side tube at point 1. Next the appropriate amount of complexant is pipetted through point 2 and into bulb B, and the ultra-torr attachment is attached to point 2. This sodide recipe calls for a slight excess of both metals to make sure that only sodide is made, with no electride. It is important to make sure the stopcock is closed and that both Ultra-Torr attachments are tightly secured before removing the K-cell from the glove box.

Once the apparatus is taken out of the glove box, it is imperative that no oxygen is allowed into the K-cell. At this point, the K-cell apparatus which contains a helium atmosphere, is directly attached to the vacuum line and evacuated. When the pressure has reached 10^{-6} torr, the apparatus is sealed with a torch at points 1 and 4. Since HMHCY is not a highly volatile complexant, it is not necessary to cool bulb B with a dry ice/isopropanol bath. When the two side-arms have been sealed-off, a freshly distilled Cs/Na mirror is deposited into bulb A by using a light flame at first to distill the cesium, then a hotter flame to distill the less volatile sodium. A nice gold-colored mirror always forms rather quickly. It is important not to distill the Cs too rapidly or else large balls of metal will form and deposit on the bottom of the bulb. This is not disastrous, but

the metal could react faster if there is a larger surface area. It is als important to prevent the metal from depositing too high on the neck of th vessel, approaching the stopcock. Applying heat near a stopcock is not good idea anyway, when the importance of a good vacuum is at stak After the metal has been completely distilled, the stem of the tube is seale at the narrowed portion of the glass, point 3.

About 10 mL. of dimethyl ether is distilled first into a flas containing Na/K alloy to react with any impurities, particularly wate then introduced into bulb B, which contains the HMHCY complexant, a about -35°C. It is crucial to improving the yield that the HMHCY dissolve completely before allowing the solution to contact the metal mirror. Thi actually is a rather difficult process because the dimethyl ether has a lov boiling point (-24.8°C) so the temperature of the bath cannot be raised to high, but high enough to dissolve the complexant. A constan temperature bath is used to maintain a temperature of about -35°C , whic is a good temperature for this process, which could take as long as tw hours. Once the complexant has dissolved, the solution is exposed to th mirror (bulb A) and the deep blue color, indicative of solvated electrons, i formed immediately. It is important to let the complexant react with all o the metal mirror to increase the yield of the final products. This proces usually took about a day. When all of the HMHCY has appeared to hav reacted, the co-solvent is added to bulb A at -78°C. In typical alkalid

syntheses, TMA or Et_2O is used as the co-solvent for crystallization of the product. However, this particular sodide nearly fully dissolves in this solvent system, so neither of these solvents acted as a good co-solvent. Instead, n-pentane is used. About 5 mL. of n-pentane is added to the existing solvent at about -40°C. At this point, the solution is brought to saturation by evaporation of Me_2O. This sometimes takes several hours. The solution is then poured through the frit to bulb A. The solid which precipitates out of solution when the saturated solution is made, is lost in the synthesis, but this assures that the impurities are left behind as well. The metal mirror is washed very well by using a cotton swab dipped in liquid nitrogen to distill over some clean solvent which is then used to dissolve any alkalide remaining in contact with the mirror. Crystal growth is effected by slow evaporation of the solvents through three additional frits, at -78°C over a period of about two days where every 15 hours an additional frit is opened. During this waiting time, the solution is carefully checked to monitor the progress of crystal formation. When a small amount of n-pentane remains in the bulb and crystals are present, the remaining solvent is used to wash carefully the crystals. This is accomplished by decanting the liquid from bulb B to bulb A, then distilling the solvent back into bulb B and washing the crystals. This is repeated several times with the hope that any uncomplexed HMHCY or other impurities will dissolve in the n-pentane and pass through the frit to

bulb A. Finally, the crystalline material is left to dry on the vacuum overnight by pumping at about 10^{-6} torr while the K-cell is kept in a ice/isopropanol bath.

It is important to note that the cleaning ritual described earlie especially important in that it helped eliminate impurities. In addition avoiding a fast precipitation of the product, good crystalline materia usually produced. By going through this extra trouble, we are allowe produce crystalline material more consistently.

When the crystals were dry, the entire K-cell is taken off the vacu line and prepared for collection of the crystals. This is done by ge placing bulb A and the fingers in a large storage container of dry ic that this half of the apparatus was kept very cold. When the K-cel sufficiently cold, it is removed from the dry ice and flipped upside-dc and bulb B is gently tapped so that all of the crystals fall nicely into fingers, which are subsequently placed in liquid nitrogen and sealed fr the K-cell with a hot flame. This is done so that when the crystals com contact with the fingers, they will not be exposed immediately to a wa surface. Instead, there is no temperature change since both parts of apparatus are in the same temperature environment.

When the time comes to transfer the material into an EPR tube, is performed in a glove bag equipped with a flow of nitrogen gas tha run through a column. A tall dewar containing the samples, a spatul

glass cutting knife, the EPR tube (Figure 2.2) and an agate mortar and pestle, are all placed inside the glove bag through the opening. Typically, about four liters of liquid nitrogen are poured into a large foam dewar

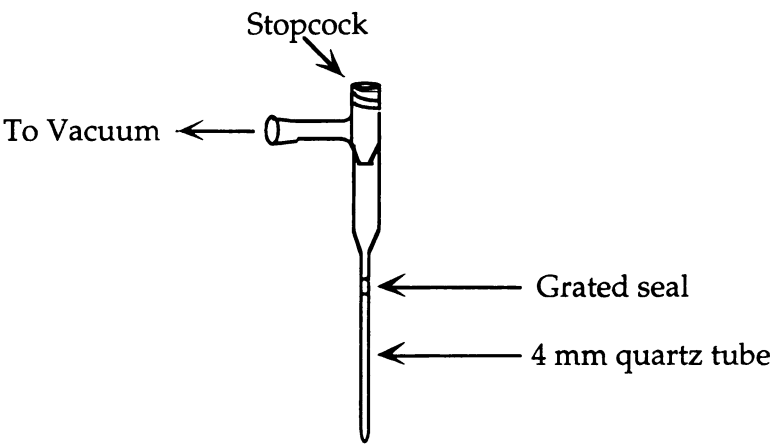

Figure 2.2: Quartz apparatus for loading electride or alkalide samples into EPR tubes.

in the glove bag to create a large positive pressure of the inert gas in the glove bag which will in turn drive out any air that remains in the bag during loading of the appropriate equipment. The glove bag is purged several times. Once the mortar has equilibrated and the temperature inside is cold (the temperature was checked with a thermocouple and was found to be -100°C), the sample tube is scored with a file and broken. The contents are poured immediately into the very cold mortar. The crystals

are then crushed with the *pre-cooled* pestle to a very fine powder. This can often take 30-40 minutes since even very small crystals can have orientational effects in the EPR spectrum when a powder pattern is desired. Some sample is then scooped with the cold spatula and funneled into the EPR tube until about 1 cm. of sample is collected at the bottom of the tube. Since the paramagnetism in this sodide originates from defect electrons, it is important to load a large amount of sample for EPR analysis. If very pure crystals are grown, there will be very few defect electrons and thus a small EPR signal, therefore a large amount of sample is needed to increase the number of paramagnetic centers. The stopcock is closed and the EPR tube is immersed in liquid nitrogen, removed from the glovebag and placed on the vacuum line. The quartz tube is evacuated, then sealed by using a very hot flame, and is subjected to EPR measurements.

BIBLIOGRAPHY

Cauliez, P. M., Jackson, J. E., & Dye, J. L. (1991) *Tetrahedron Letters 32*, **An Unusual Reduction of Ethylene Occurring during the Thermal Decomposition of Alkalides and Electrides**, 5039-5042.

CHAPTER 3

THEORETICAL TREATMENT OF ELECTRON MAGNETIC RESONANCE SPECTROSCOPY

Spectroscopy

When scientists applied the principles of quantum mecha
describe atoms and molecules, they found that discrete levels existe
with some characteristic energy. Spectroscopy† involves the
electromagnetic radiation to probe the energy levels of atoms or mo
that arise from a variety of interactions. Knowledge derived from
measurements allows an insight into the structure and the dynan
the particular sample under observation. In magnetic resonanc
probes the different energy states that result from the interaction
molecule's or atom's magnetic moment with an applied magnetic
Transitions between the resulting energy states occur upon the appli
of radiofrequency or microwave radiation.

Magnetic Interactions

Magnetic resonance is driven by the occurrence of magnetic d
which implies angular momentum (a charged particle that is mo
Electromagnetic radiation is composed of oscillating electric and ma
fields, perpendicular to one another. In optical spectroscopy, the

---

†For useful background of electron paramagnetic resonance spectroscopy, see: (Abr
Bleaney, 1970, Carrington & McLachlan, 1979, Wertz & Bolton, 1986)

interaction of light and the electric dipole moment in a molecule important. In EPR spectroscopy, a molecule with magnetic dipole interacts with the magnetic component of the radiation. In NMR, th nucleus has only spin angular momentum, however in EPR the electro possesses both spin and orbital angular momentum that contribute in vectorial sum. The magnetic dipole is measured via the magnetic dipo moment, μ. The energy of the interaction between the magnetic field an the electron dipole moment is shown in this classical equation,

$$E = -\vec{\mu} \cdot H$$

$$= -\mu H \cos\theta \qquad (3.1)$$

where μ is a proportionality constant between the applied field and th energy and θ is the angle between the magnetic field and the axis of th dipole. This can be described pictorially by three arrangements, Figur 3.1. The dipole-dipole interactions are a direct consequence of directiona interactions of two *electronic* dipoles, in optical spectroscopy and *magneti* dipoles in EPR spectroscopy. One can relate the linear momentum for a electron, $\vec{p}$, to the magnetic moment, $\vec{\mu}$, by,

$$\vec{\mu} = \gamma \vec{p} \qquad (3.2)$$

as in a system with angular momentum that possess a magnetic moment

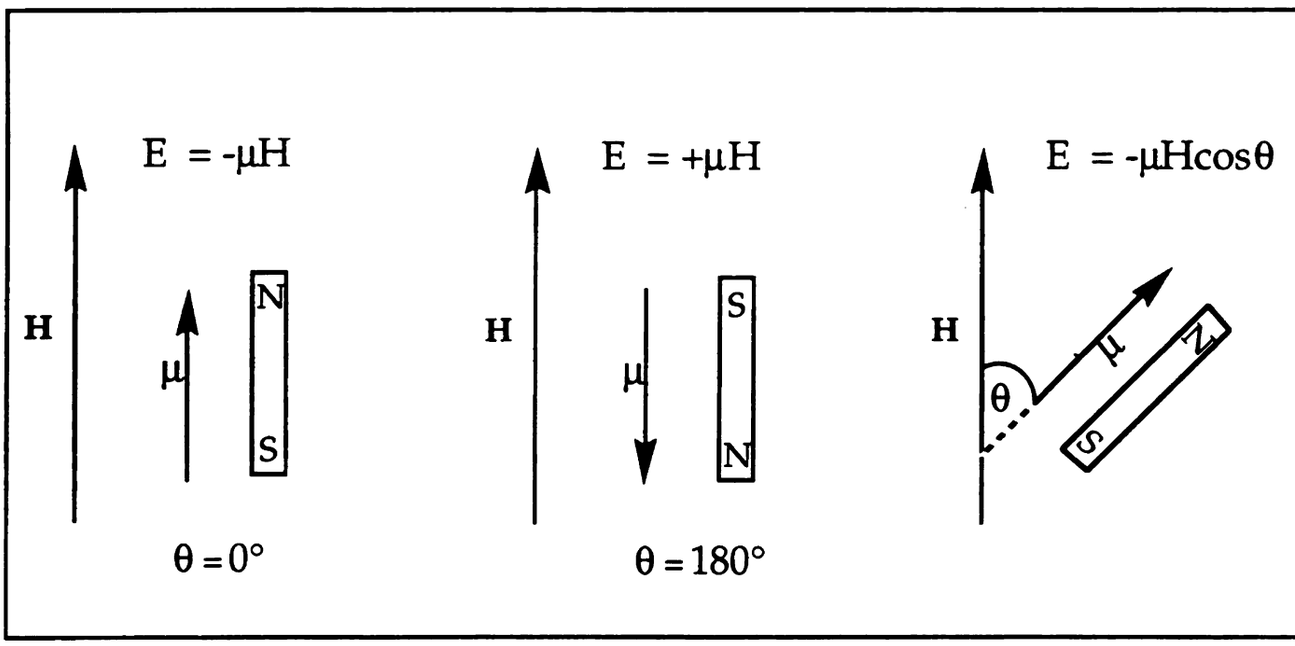

Figure 3.1: Classical picture of the energy of a dipole in a magnetic field as a function of the angle between the dipole moment vector and the magnetic field.

colinear with $\vec{p}$. The constant γ is the magnetogyric ratio, $e/2mc$, whe
e is the charge of the electron, m is the mass of the electron, and c is th
speed of light.

Since electrons and nuclei obey *quantum*, not *classical* mechanic
magnetic moments are always quantized, therefore only a finite number
discrete energy levels exists. The magnetic moment of an electron aris
from the "spin" or the intrinsic angular momentum. The energ
associated with the electron spin magnetic moment is also quantized. B
continuing the classical description above, consider the electron spi
angular momentum, $\mathbf{S}\hbar$, and m_s, the projection of the electron spi

angular momentum. The electron can have the allowed projectio

$= \pm 1/2$. Assuming quantization for an electron along the field dir

$$p_z = m_s h/2\pi \qquad (3.3$$

Relating the dipole moment of the electron to the spin angular

and the quantum number m_s, from Equation 3.2,

$$\mu_z = (-eh/4\pi mc)m_s \qquad (3.4$$

So far, the orbital angular momentum has not been acknowledged

equations. This is done by introducing the factor, *g*,

$$\mu_z = -g(eh/4\pi mc)m_s \qquad (3.5$$

where *g* is the Landé *g*-factor and can be described by,

$$g = 1 + \frac{J(J+1) + S(S+1) - L(L+1)}{2J(J+1)} \qquad (3.6$$

where J is the spin-orbit coupling, L is the orbital angular momen

S is the spin angular momentum. For a free electron, the *g*

2.00000, J=S, L=0. If the quantity $(e\hbar/2mc)$ is designated as a con

$$\mu_z = -g\beta m_s \qquad (3.7$$

and substituting Eq. 3.7 into 3.1,

$$E = -g\beta \mathbf{S} \cdot H \qquad (3.8$$

The Spin Operator

The task in quantum mechanics is to rewrite classica expressions like Eq. 3.1 in terms of operators. Since this sys discrete energy levels which are described by well defined q numbers, an eigenvalue equation can be written. Consider a where λ_i represents an eigenvalue of an operator and ϕ_i repres corresponding eigenfunction. An eigenvalue equation can be w follows,

$$\hat{O}\phi_i = \lambda_i\phi_i \qquad (3.9$$

where $\hat{O}$ is the operator for the system. Spin operators are nec account for the delicate points that the classical description cann as the analogy for the coupling between the electron spin and the spin. Since EPR incorporates spin angular momentum, a spin op appropriate here. This spin operator will operate on a specifically defining a spin state. Spin operators can be used to energy levels of an electron in a system. Equation 3.7 can be w relate the electron dipole moment with the spin magnetic momen

$$\mu_z = -g\beta m_s \qquad (3.1$$

and by replacing **S** with $\hat{S}$, the use of the spin operator can cha the energy in the form of a hamiltonian,

$$\mathcal{H} = g\beta \vec{H} \cdot \hat{S} \tag{3.11}$$

$\vec{H} \cdot \hat{S}$ can be expanded,

$$\vec{H} \cdot \hat{S} = \hat{S}_x H_x + \hat{S}_y H_y + \hat{S}_z H_z \tag{3.12}$$

Assuming quantization along the z-axis, the vector components of t magnetic field (H) are $(0,0,H_o)$, therefore Eq. 3.9 can be written as,

$$\mathcal{H} = g\beta H_o \hat{S}_z \tag{3.13}$$

When the hamiltonian operates on the wavefunction, the eigenvalue generated when it is an eigenstate of the hamiltonian. This will be appli later within this chapter to a real system with an electron and interacting nucleus.

The Spin Hamiltonian

The Electronic Zeeman Interaction

The time independent hamiltonian shown above, Equation 3.1 describes the interaction between an electron with the applied magne field, and is called the *Electronic Zeeman* term. The eigenfunctions of t hamiltonian are,

$$\phi\alpha = |\alpha\rangle \quad \text{and} \quad \phi\beta = |\beta\rangle$$

With the corresponding eigenvalues being $m_s = +1/2$ and $m_s = -1$ respectively. The lowest energy state corresponds to $m_s = -1/2$ or assuming a positive *g*-value. The transition energy between the two st can be described by,

$$E = \pm 1/2\, g\beta H$$

$$\Delta E = g\beta H \qquad (3.14)$$

$$h\nu = g\beta H \qquad \text{(the "resonance" condition)}$$

where $h\nu$ is the quantum of energy supplied to the system (h is Plan constant, ν is the frequency of electromagnetic radiation). Furt consideration of the *g*-value[§] shows that there is hidden informat within this factor. Orbital angular and spin angular momenta are fol into the *g*-factor. In other words, the electron *g*-factor describes how spin angular momentum couples to the magnetic field. In addition, nature of the *g*-value gives an idea of which orbital holds the unpai electron and is a measure of the deviation from the free electron va which has only spin angular momentum.

The Nuclear Zeeman Interaction

This term in the hamiltonian, once again assuming that the sys is in a magnetic field that is defined as the z-axis, can be described as,

---

[§]The *g*-value is often treated as a scalar, but strictly speaking, it is a tensor.

$$\mathcal{H}_{NZ} = -g_N\beta_N H\hat{I}_z \qquad (3.15)$$

where $\hat{I}_z$ is the nuclear spin operator, β_N is the nuclear magneton and
is the nuclear *g*-value. This term describes the interaction of the nucl
moment with a magnetic field. It is opposite in sign and smaller
magnitude than the electronic Zeeman term. The spin quantum numb
$m_I = \pm 1/2$ are defined such that $m_I = +1/2$ is of lowest energy (when g_N
positive).

The Hyperfine Interaction

The interactions discussed thus far have been between an electr
or nucleus and a magnetic field. If this were the only effect measured
using EPR, all spectra would be relatively indistinguishable as they wou
consist of only one line. The only useful feature would be the *g*-value. T
g-value does not however reveal much information about the molecu
structure of the sample. The resonance can be perturbed by the magne
fields *within* the paramagnetic substance since the unpaired electron
sensitive to its local surroundings. These fields arise from the magne
nuclei interacting with the electron spin. Some nuclei possess an intrin
spin angular momentum and thus have a magnetic moment associat
with it them. The interaction between the local magnetic field of t
nucleus and the electron is the known as the *nuclear hyperfine interacti*

This interaction can be either orientation dependent with respect to the laboratory field (anisotropic), or independent of the orientation of the field (isotropic).

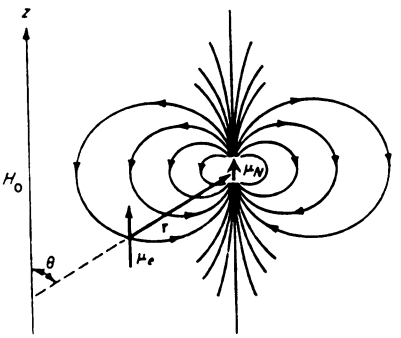

Figure 3.2: The interacting dipoles, μ_e and μ_n, are connected by the vector r where θ is the angle between r and the applied magnetic field. Since $\mu_e >> \mu_n$, when referring to the electron-nuclear hyperfine interaction, it is actually the effect of the nuclear field at the electron that is being considered, since the nucleus has a magnetic moment. The effective fields that the electron experiences is the lab field plus the induced hyperfine field.

The hyperfine interaction is composed of two parts, the isotropic or Fermi contact interaction (Eq. 3.19), and the anisotropic or a special case, the dipolar interaction (Eq. 3.21). The Hamiltonian describing the hyperfine interaction follows,

$$\mathcal{H}_{hfi} = \mathcal{H}_{iso} + \mathcal{H}_{dip} \qquad (3.16)$$

The Fermi contact interaction is a through bond interaction where there exists a non-zero probability of the electron being at the nucleus.

This only occurs in s-orbitals and can be seen easily by looking at the wavefunctions of the *1s*, *2p* and *3d* orbitals (Figure 3.3). The *2p* and *3d* orbitals have a node at the origin; therefore, the probability of the electron being located at the nucleus is zero. The isotropic hyperfine interaction can be described by the equation,

$$A_{iso} = \frac{8\pi}{3} |\psi(0)|^2 \mu_e \mu_n \qquad (3.17)$$

where $|\psi(0)|^2$ is the wavefunction evaluated at the nucleus. By replacing the magnetic moments with their corresponding operators, Eq. 3.15 becomes,

$$A_{iso} = \frac{8\pi}{3h} g_e \beta_e g_n \beta_n |\psi(0)|^2 \hat{S}_z \hat{I}_z \qquad (3.18)$$

$$A_{iso} = hA_0 \hat{S}_z \hat{I}_z \qquad (3.19)$$

where A_o is the isotropic hyperfine coupling constant, $\hat{I}_z$ is the nuclear spin operator, $\hat{S}_z$ is the electron spin operator and the measurement of the interaction energy between the electron and the nucleus is hA_o. For example, in an I=1/2 system, the single EPR absorption is split into two peaks, $\pm H_1$ (the local magnetic field produced by the nucleus at the electron), Figure 3.4.

In fixed systems, it is necessary to consider the classical interaction between an electron dipole and a nuclear dipole,

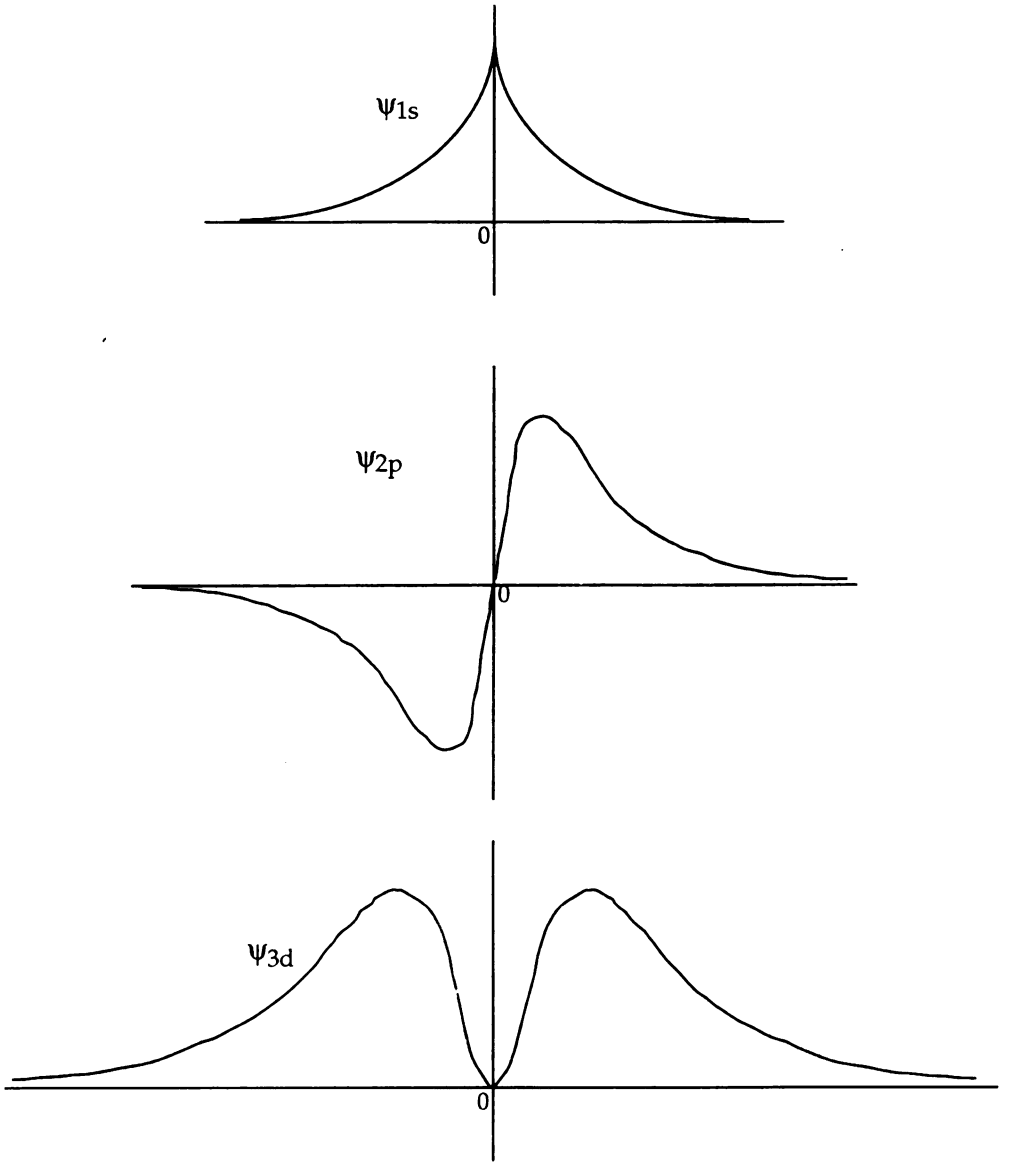

Figure 3.3: Radial dependence of the *1s*, *2p* and *3d* wavefunctions of the hydrogen orbital. Note that the electron density at the *1s* orbital is non-zero, unlike the *2p* and *3d* orbitals, which have a node at the nucleus.

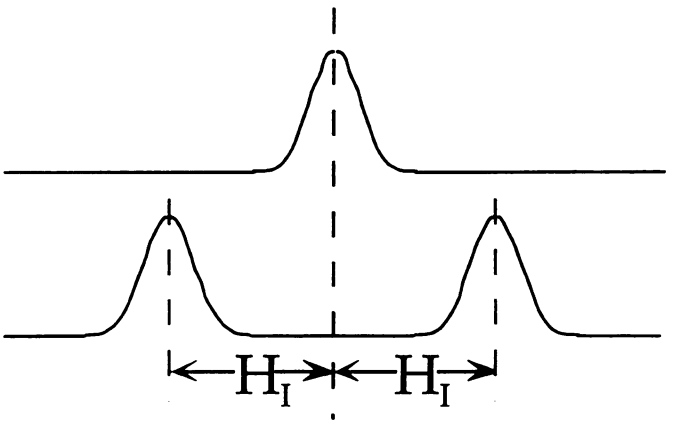

Figure 3.4: The H_1 field adds to or opposes the laboratory magnetic field, depending on the alignment of the moment of the nucleus. When H_1 adds to H_0, less magnetic field strength is needed from the laboratory field and therefore the resonant field is lowered by H_1. The opposite is true when H_1 opposes the lab field.

$$E = \frac{\vec{\mu}_e \cdot \vec{\mu}_n}{r^3} + 3\frac{(\vec{\mu}_e \cdot \vec{r})(\vec{\mu}_n \cdot \vec{r})}{r^5}$$

where: $\vec{\mu}_e = g\beta\hat{S}$

$\vec{\mu}_n = g\beta\hat{I}$ (3.20)

By making substitutions with the quantum mechanical counterpart,

$$\mathcal{H}_{dip} = -g_e\beta_e g_n\beta_n \left\{\left(\frac{\hat{S} \cdot \hat{I}}{r^3}\right) - 3\frac{(\hat{S} \cdot \vec{r})(\hat{I} \cdot \vec{r})}{r^5}\right\} \quad (3.21)$$

The dipolar tensor can be seen by expanding the vectors in Eq. 3.21. The anisotropic or dipolar component results from the two dipoles interacting. The strength of this interaction can be described, to a first approximation,

$$A_{dip} = \frac{(1-3\cos^2\theta)}{r^3}\ \mu_e\mu_n \qquad (3.22)$$

The dipolar matrix is traceless; thus the contribution of the observables
the limit of fast motion†, goes to zero. In solutions where all values of
are equally probable, the term $(1-3\cos^2\theta)$ vanishes and therefore th
dipolar part of the hyperfine also vanishes. In solids, all possib
orientations of θ are observed, but they are observed unequally and th
more probable the orientation, the more it contributes to the EP
absorption. Thus the total hamiltonian for an isotropic system is given b

$$H = g\beta H\cdot \hat{S} - g_N\beta_N H\cdot \hat{I} + h\hat{S}\cdot \underset{\sim}{A}\cdot \hat{I} \qquad (3.23)$$

where $\underset{\sim}{A} = A_o\mathbf{1} + \mathbf{T}$, and $\mathbf{T}$ is the hyperfine tensor.

The isotropic g-value is a scalar, but a rigid system can b
anisotropic also, where the more probable orientation, perpendicula
contributes largely to the absorption while the parallel orientations do n
contribute as strongly to the EPR absorption, as illustrated in Figure 3.5.
the field in the x-direction has the same effect as the field in the
direction, they both contribute to the perpendicular component of th
g-tensor. The field in the z-direction is then different from the x and the
is known to have *axial* symmetry.

† Fast motion is the limit of coupling; i.e. Consider a dipole-dipole interaction of 1 MHz. F
motion is when the molecule is rotating quickly with respect to 1 MHz. The time scale for f
motion is on the order of the energy of the interaction.

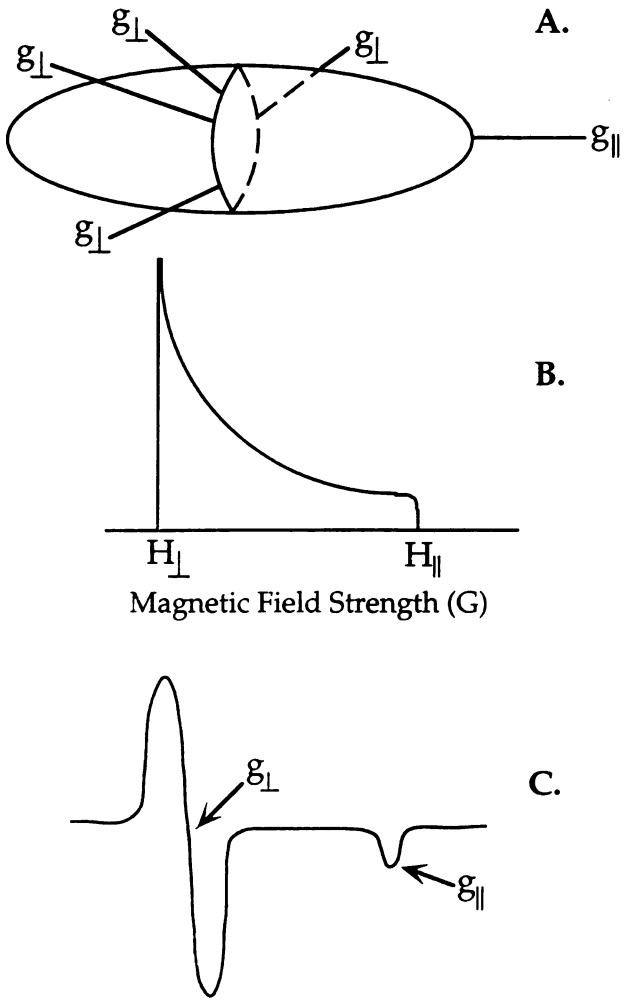

Figure 3.5: A.) A large number of systems with axes nearly perpendicular to the field direction, Z, results in a larger contribution to the EPR lineshape. This is in contrast to the less likely instance of systems aligned nearly parallel to the field direction. B.) The powder pattern absorption indicating the two turning points, parallel and perpendicular where the field values $H_\parallel$ and $H_\perp$ represent field extrema and therefore the highest probability of observing a line. There is no hyperfine interaction illustrated here. C.) First derivative line of B. The inflection in the line represents the perpendicular turning point where the more probable orientations contribute the greatest to the lineshape.

The EPR Experiment

In a system with one unpaired electron, the electron spin can possess one of two values, $m_s=\pm 1/2$. In the absence of a magnetic field, these states are degenerate. In a strong magnetic field, the degeneracy of these states is split as described by the resonance condition shown above, and illustrated Figure 3.6. Resonance is achieved when the frequency of the radiation times h is equal to the energy level separation. Due to instrumental constraints, (the sample probe is an RLC circuit operated at its resonant frequency), the frequency is held constant throughout the experiment thus the technology does not permit one to sweep the frequency and the magnetic field is swept instead.

The energy separation needed to satisfy the resonance condition in EPR is very small compared to that same splitting in optical spectroscopy. A typical value of ΔE in optical spectroscopy is 10^{14} Hz while that in EPR is on the order of 10^{10} Hz. Therefore, there are four orders of magnitude difference in frequency units between the two. The quantity kT at room temperature is 6×10^{12} Hz so in optical spectroscopy, the population of the upper level is small since the splitting is huge compared to kT. This results in high sensitivity even with nanomolar concentrations. The population difference between the levels in EPR is very small since the splitting is less than kT; consequently the sensitivity is reduced to μmolar concentrations. For example, at room temperature and at X-band (9-10

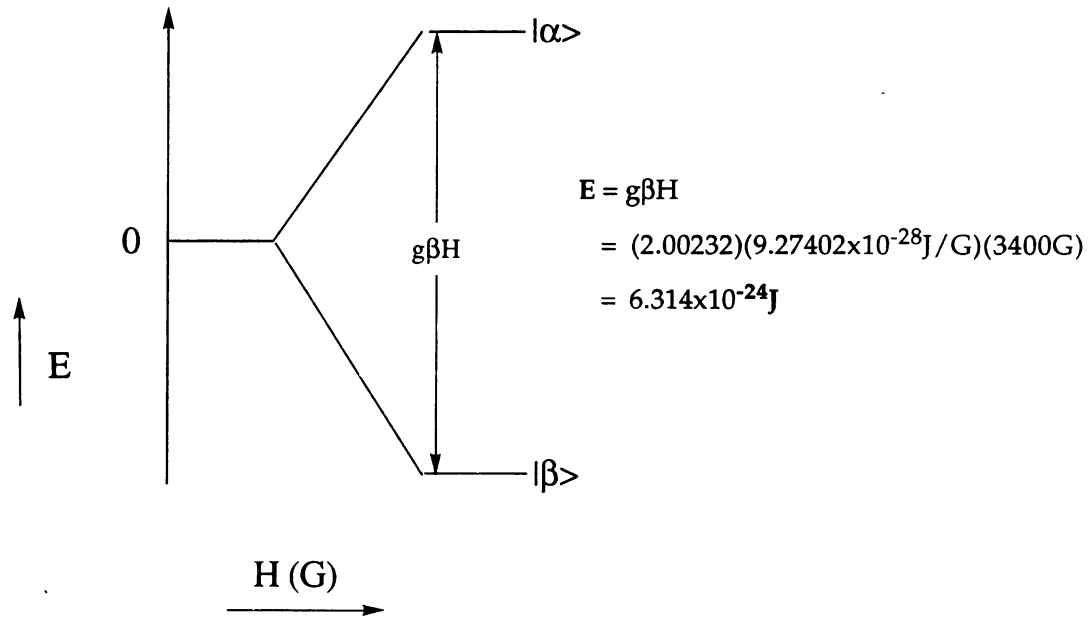

Figure 3.6: Electron spin levels in a magnetic field. The degeneracy of the two levels is split when a magnetic field is applied. Resonance is achieved when the frequency of the incident radiation matches the frequency corresponding to the energy level separation. For a typical laboratory magnetic field of 3400 G, ΔE is on the order of 10^{-24} J, thus the frequency of the electromagnetic radiation used for this spectroscopy is around 9.5 GHz or the microwave region (X-band).

GHz), the population difference between the α and β states ca
described by a Boltzmann distribution as follows:

$$\frac{n_{+1/2}}{n_{-1/2}} = e^{-\Delta E/kT}$$

$$= e^{-g\beta H/kT}$$

$$= 0.998 \qquad (3.24)$$

Therefore, only a 0.2% difference in the population exists betwee
states $|\alpha\rangle$ and $|\beta\rangle$. A population difference is crucial for the experin
therefore if there is no difference in population between the two state
EPR resonance will be observed. The system is said to be *saturated* u
such conditions.

Overall, the interaction of a magnetic dipole with electromag
radiation can induce transitions between two Zeeman levels if the ph
energy (hν) equals the separation gβH, and the magnetic field compo
of the microwaves is directed perpendicular to the laboratory field.

Application of the Hamiltonian

Consider a nucleus that has an intrinsic nuclear spin, I=1/2.
nuclear hyperfine interaction splits each of the Zeeman levels into
levels. The observed transitions are those obeying the EPR selection r
$M_S = \pm 1$ and $M_I = 0$. The complete hamiltonian for such an isotr
system is,

$$\mathcal{H} = \beta\vec{H}\cdot\underset{\approx}{g}\cdot\hat{S} - g_n\beta_n\vec{H}\cdot I + hA_o(\hat{S}_x\hat{I}_x + \hat{S}_y\hat{I}_y + \hat{S}_z\hat{I}_z) \tag{3.25}$$

For first order energies and assuming quantization along the z-axis, $\hat{S}_x\hat{I}_x$ and $\hat{S}_y\hat{I}_y$ vanish. These terms become important if second order hyperfine interactions are present. To determine the energies provided in the hamiltonian, a basis set is employed, consisting of four possible combinations of electron and nuclear spin functions.

$$\phi_1 = |\alpha_e, \alpha_n\rangle \qquad \phi_3 = |\beta_e, \alpha_n\rangle \tag{3.26}$$

$$\phi_2 = |\alpha_e, \beta_n\rangle \qquad \phi_4 = |\beta_e, \beta_n\rangle$$

$\hat{S}_z$ operates only on the electron spin function and $\hat{I}_z$ operates only on the nuclear spin function,

$$\hat{S}_z\,|\alpha_e, \beta_n\rangle = 1/2\,|\alpha_e, \beta_n\rangle \tag{3.27}$$

$$\hat{I}_z\,|\alpha_e, \beta_n\rangle = -1/2\,|\alpha_e, \beta_n\rangle \tag{3.28}$$

Thus the energies for these states can be obtained by solving the hamiltonian matrix, such as the matrix element where the scalars, $g\beta H$, have been pulled out of the equation,

$$E_{\alpha_e\beta_n} = \langle\alpha_e, \beta_n|\,\mathcal{H}\,|\alpha_e, \beta_n\rangle \tag{3.29}$$

$$= \langle\alpha_e, \beta_n|\,g\beta H\hat{S}_z - g_N\beta_N H\hat{I}_z + hA_o\hat{S}_z\cdot\hat{I}_z\,|\alpha_e, \beta_n\rangle$$

$$= 1/2g\beta H + 1/2g_N\beta_N H + 1/4hA_o$$

and the energies for the other states are obtained similarly,

$$E_{\alpha_e\alpha_n} = +1/2g\beta H - 1/2g_N\beta_N H + 1/4hA_o$$
$$E_{\beta_e\alpha_n} = -1/2g\beta H - 1/2g_N\beta_N H - 1/4hA_o \qquad (3.30)$$
$$E_{\beta_e\beta_n} = -1/2g\beta H + 1/2g_N\beta_N H + 1/4hA_o$$

The interactions between an electron and a nucleus (I = 1/2), are easiest viewed in an energy level diagram (Figure 3.7). Other interactions such as the nuclear quadrupole interaction and the spin-spin interaction are important in some systems but are negligible in the systems presented in this dissertation, so they will not be discussed.

Relaxation

Discussed in this chapter are a few factors that influence the EPR linewidths. The resonance lineshape can be broadened by the uncertainty in the lifetime. The spin-lattice relaxation time, referred to as T_1, can occur from interactions between a paramagnetic center and thermal vibrations in the lattice. It is the characteristic time for the spins to equilibrate with the lattice and can be described by a 1/e time. If T_1 is sufficiently long, one can observe an EPR spectrum at room temperature. Generally, as the temperature is decreased, T_1 is increased. The spin-spin relaxation time, T_2, occurs due to interactions originating from small local magnetic fields that exist on some paramagnetic nuclei. These local fields cause a shift in

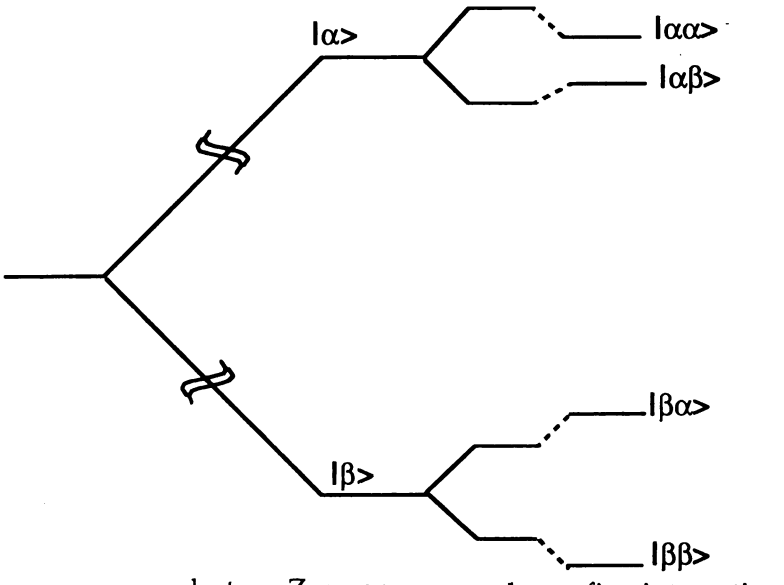

$$\mathcal{H} = \beta \underset{\sim}{H} \cdot \underset{\approx}{g} \cdot \hat{S} - g_N \beta_N \underset{\sim}{H} \cdot \hat{I} + A\hat{I} \cdot \hat{S}$$

Figure 3.7: Energy level diagram for a S=1/2, I=1/2 system.

the total field at the paramagnetic center. The distribution of energies serves to broaden the line.

Consider the system where the spins in a sample experiences a heterogeneous magnetic environment made up of the lab field and weak local fields arising from magnetic nuclei. When the motion is very rapid, the spins sample the full gamut of the heterogeneity thus local fields will add to or subtract from the lab field by inducing a spread in the resonance frequency, giving rise to a broadening of the resonance lineshape. This is known as *homogeneous broadening*. This takes place when rapid motion occurs with respect to the EPR time scale, such as in liquids.

In solids, a more complicated situation occurs. The motion is slow, coming mainly from vibrations, and the spins in general will only be affected by a small portion of the heterogeneity. When the unpaired electron is subjected to slightly different effective magnetic fields, as any given time, only a small portion of spins are sampled. This results in a superposition of individual spin packets, each shifted slightly from one another. Each individual spin packet has a lorentzian lineshape and is homogeneously broadened while the envelope of the spin packets is the *inhomogeneously broadened line*. Figure 3.8 illustrates this point.

When the system is at thermal equilibrium, the magnetization is along the z axis. A vector sum of the individual moments or spins are precessing at some frequency ω_o, about the lab field B_o. Relaxation times

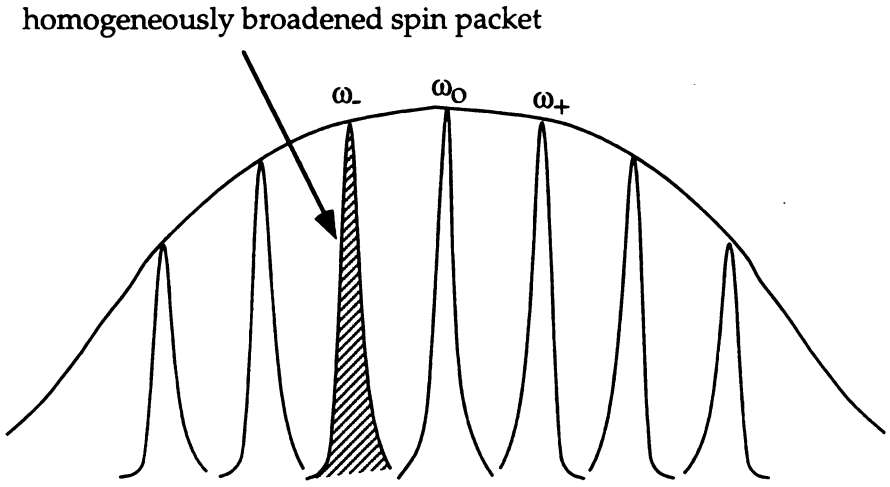

Figure 3.8: Inhomogeneously broadened line

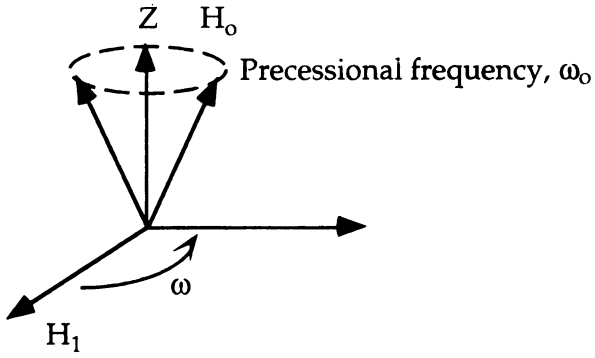

Figure 3.9: Rotating frame

that describe the gain or loss of magnetization can be described by T_1. Along x or y, T_2 describes the loss of coherence (torque the cone when the B_1 field is turned on so that there is some non-zero projection in the xy plane). As B_1 is turned off, there is a loss and the time it takes for the frequency to randomize is T_2.

Electron Spin Echo Envelope Modulation

Often there are weak superhyperfine couplings between the paramagnetic center and nearby magnetic nuclei that are unresolved due to inhomogeneous broadening. Modulations, or a periodic variation of amplitude, can occur which are associated with small splittings of the resonance line. This modulation effect can be used to measure splittings that are unresolvable in the presence of inhomogeneous broadening. A method to probe these interactions used today is Electron Spin Echo Envelope Modulation (ESEEM). The typical two-pulse sequence and the time evolution of the echo decay trace is outlined in Figure 3.10.

The principles of ESEEM are based on an inhomogeneously broadened line originating from anisotropic interactions. The unpaired electron is subjected to slightly different magnetic fields thus only a small fraction of the spins are sampled. A superposition of the different spin packets exists which are all slightly shifted from the resonance frequency,

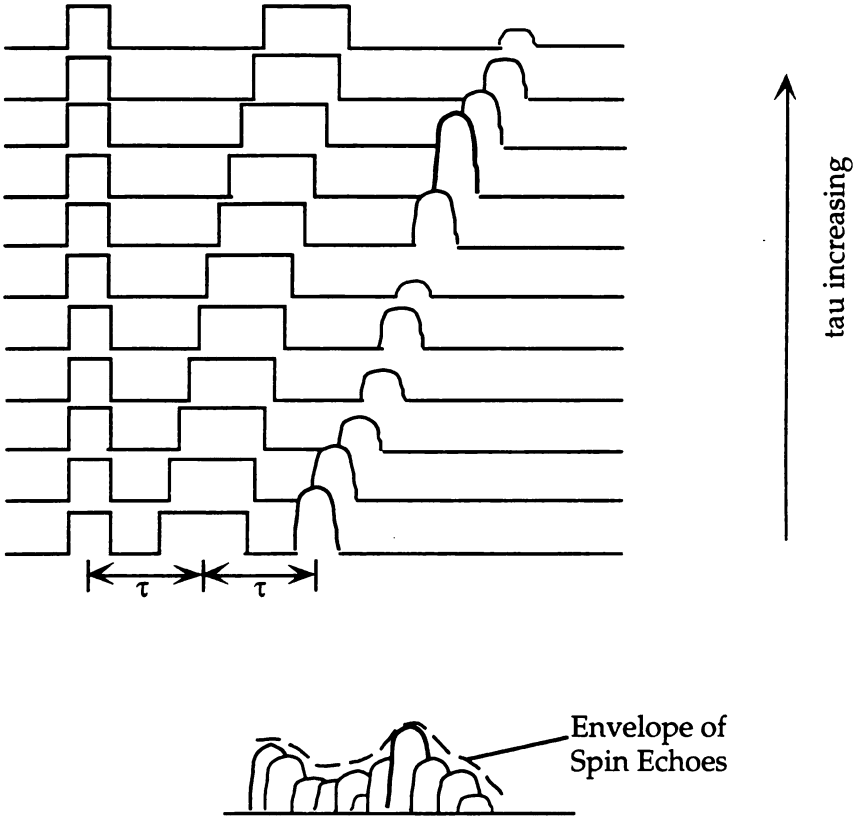

Figure 3.10: Diagram showing the time evolution of the echo decay envelope. The envelope is modulated by the couplings between the electron spin and the neighboring nuclei. The two pulse experiment is a function of the spacings between the pulses (τ). In the three pulse experiment, the spacing between the second and third pulses, T, is varied while τ is set to a fixed value.

ω_o. All spin magnetic moments belonging to the same spin packet precess with a characteristic precessional frequency (Figure 3.11).

When the first $\pi/2$ pulse is applied, the spin packets dephase immediately. After a certain time τ, on the order of nanoseconds, the second π pulse is applied which flips the magnetization 180°. The same

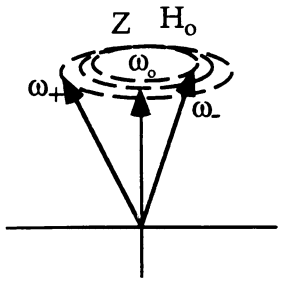

Figure 3.11: Precessional frequencies of the individual spin packets. The magnetization is along the z-axis.

time τ occurs while the precessional frequencies remain unaltered. After this time τ is applied a second time, the spin packets refocus in the -y direction and this buildup of magnetization is known as the spin echo, primary echo or Hahn echo. The vector scheme for the two pulse experiment is described in Figure 3.12.

The echo decay trace features the integrated intensity of the echo as a function of the spacing between the pulses. Fourier transformation of

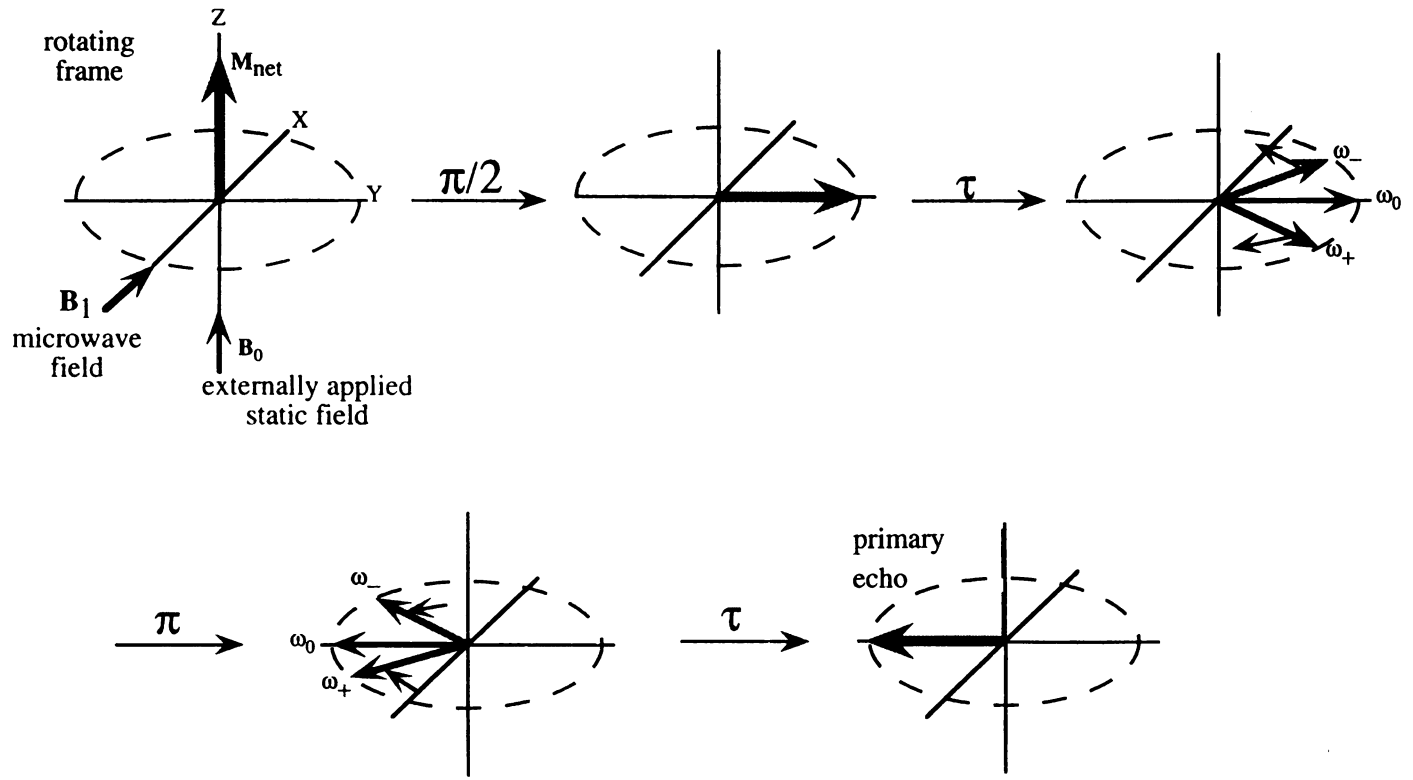

Figure 3.12: Vector scheme for the 2-pulse ESEEM experiment.

the time domain trace allows one to observe the frequencies easier. The decay is not monotonic since the decay is modulated by interactions with nearby magnetic nuclei. The electron spin packets relax via a T_2 or T_M (phase memory time) relaxation process, the time it takes for the echo amplitude to decay to 1/e of its initial value. If the echo amplitude decays exponentially, $T_2=T_M$. This relaxation time is generally short thus the echo and modulations decay very rapidly.

In a 3-pulse experiment, the pulse sequence is changed slightly. In this case a $\pi/2$ pulse is followed by a time τ, then another $\pi/2$ pulse occurs to flip the magnetization into the -x direction. After a time T, a final $\pi/2$ pulse occurs so that the magnetization vectors are in the xy plane but they are dephased with frequencies $\pm \omega$. After the same time τ the spins refocus and the magnetization vector is aligned along the -y direction yielding the spin echo or stimulated echo. The pulse sequence schemes for the 2-pulse echo modulation and 3-pulse echo modulation is shown in Figure 3.13. The 3-pulse echo decays via a T_1 mechanism.

Nuclear Modulation Effect

The inhomogeneous broadening that is required for the spin echo effect to occur can mask the hyperfine structure in the EPR spectrum resulting in a loss of resolution. The decay is not a monotonic decay but instead is modulated by the hyperfine frequencies. To understand better

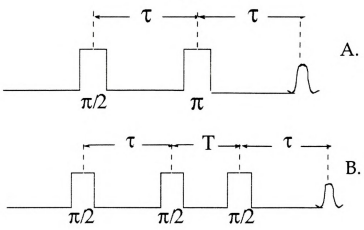

Figure 3.13: ESEEM pulse schemes for the A.) 2-pulse and B.) 3-pulse experiments.

the origin of these modulations, we turn to the classical description of nuclear modulation. Consider a four level system with S=1/2 and I=1/2, Figure 3.14. The states are mixed by anisotropic hyperfine interactions therefore all four transitions can be induced by a single microwave pulse. Branching occurs as a result of microwaves inducing transitions beginning at one energy level but ending at a different energy level. If the system were isotropic, only the allowed EPR transitions 1-4 & 2-3 would occur, but because of the anisotropic nature of the interaction, the nuclear spin states are mixed and the semi-forbidden transitions a & d are allowed to some extent. Short microwave pulses yield a large frequency spread, thus all four transitions can be excited coherently. After the first $\pi/2$ pulse, the magnetization is split into many components with different

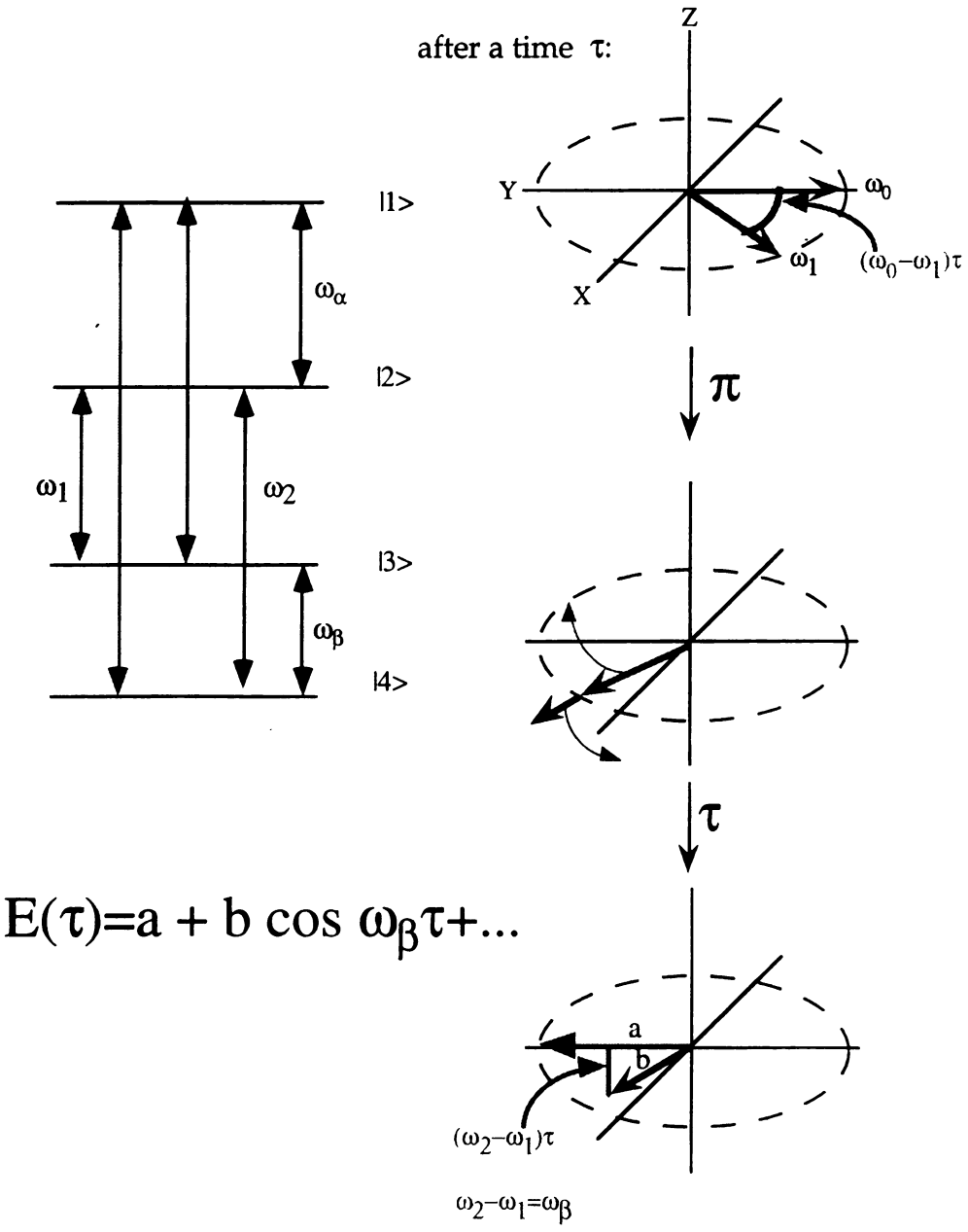

Figure 3.14: Nuclear modulation effect for the 2-pulse echo scheme. The evolution of the spin packets is shown after the first $\pi/2$ pulse. The first two terms of the modulation function [$E(\tau)$] are shown.

resonance frequencies. Assume *a* precesses at the frequency of the rotating frame and *b* does not. After the $\pi/2$ pulse and during a time τ, *b* starts to dephase with respect to the rotating frame. After the π pulse, *a* is inverted to the -y direction but because of branching, a second component is formed with frequency ω_2', from *a*. The original *b* component will refocus as usual after a time τ after the π pulse. The projection of the magnetization of the *b'* vector onto -y is given by $\cos(\omega_2-\omega_1)\tau$ thus it will not contribute fully to the echo. The same is applied for spin *b* and all other combination of spin packets formed by branching of transitions. Therefore all hyperfine frequencies are expected to appear in the echo envelope.

The Density Matrix Formalism

The goal of this section of the chapter is to understand the theoretical framework and the use of the density matrix formalism developed by Mims (Mims, 1972a, Mims, 1972b). This treatment is a convenient method for computing the modulation function of the ESEEM pattern. The expressions are obtained by partitioning the matrices which describe the time evolution of the quantized system. This review is not meant to be a comprehensive treatment and can be supplemented by quantum mechanics texts (Cohen-Tannoudji *et al.*, 1977, Slichter, 1990). It

is recommended that the reader works through the math as many steps have been left out for simplicity.

The general expression for the 2-pulse ESEEM modulation function with a dimensionality of 2I + 1 is derived.

$$E(t) = \mathrm{Tr}(Q_\tau^\dagger M^\dagger P_\tau^\dagger M Q_\tau M^\dagger P_\tau M) \tag{3.31}$$

In a system described by a wavefunction, ψ,

$$\psi(q,t) = \Sigma c_n(q,t)\phi_n(q) \tag{3.32}$$

ψ can be obtained from the solution to the Schröedinger equation. The density matrix, ρ, is defined by,

$$\rho_{nm} = c_n c_m^* = \langle n \mid \rho \mid m \rangle = \langle \phi_n \mid \rho \mid \phi_m \rangle \tag{3.33}$$

where ρ is the density operator. The physical observables are determined by,

$$\langle M \rangle = \mathrm{Tr}\{\rho,M\} = \mathrm{Tr}\{M,\rho\} \tag{3.34}$$

The density matrix can now be deduced by implementing the equation of motion.

$$d\rho/dt = i/h[\rho,\mathcal{H}] \tag{3.35}$$

therefore the density matrix can be rewritten as,

$$\rho = e^{(-i\mathcal{H}t/h)}\, \rho_{(0)}\, e^{(i\mathcal{H}t/h)} \tag{3.36}$$

In ESEEM, the hamiltonian, $\mathcal{H}$, describes the interaction of the static field ($\mathcal{H}_0$) and the resonance field ($\mathcal{H}_1$),

$$\mathcal{H} = \mathcal{H}_0 + \mathcal{H}_1 \tag{3.37}$$

To calculate the echo signal, E, Eq. 3.31 must be integrated to correlate the final density, ρ_E, with the initial density, ρ_0. Therefore,

$$E = \eta \, \mathrm{Tr}(\rho \mathcal{H}_1) \tag{3.38}$$

where η is a proportionality constant. All of the matrices in the general expression of the modulation function of the 2-pulse ESEEM are shown below:

$$P_\tau = \begin{pmatrix} e^{iw_a t} & 0 \\ 0 & e^{iw_b t} \end{pmatrix} \qquad Q_\tau = \begin{pmatrix} e^{iw_c t} & 0 \\ 0 & e^{iw_d t} \end{pmatrix} \tag{3.39}$$

which come from the time dependent Schröedinger equation. The general form of a unitary transformation is given by $M = M\alpha^{\dagger} M\beta$ where,

$$M = \begin{pmatrix} v & u \\ -u^* & v^* \end{pmatrix} \qquad M^{\dagger} = \begin{pmatrix} v^* & -u \\ u^* & v \end{pmatrix} \tag{3.40}$$

corresponding to the diagram in Figure 3.15. When the matrices are multiplied and the trace is taken, as described in Eq. 3.31, Eq. 3.41 is obtained.

$$E_{mod}(\tau) = |v|^4 + |u|^4 + |v|^2 |u|^4 [2\cos\omega_{ab}\tau + 2\cos\omega_{cd}\tau - \cos(\omega_{ab} - \omega_{cd})\tau - \cos(\omega_{ab} + \omega_{cd})\tau] \tag{3.41}$$

$|v|$ and $|u|$ are transition probability amplitudes, which also describe the extent of which branching of transitions is allowed or forbidden. If $|u| = 0$ or $|v| = 0$, (this will occur if one transition is fully allowed and the other fully forbidden) no modulations are present, but an echo will still be present. To determine the values of $|v|$ and $|u|$, the transformations can be described as rotations of the electron-nuclear coordinate system, (Figure 3.16).

What do the values of $|v|$ and $|u|$ represent? To understand this mathematically, solve the hamiltonian matrix with a rotation of the nuclear xy axis, which eliminates the I_y term.

$$\mathcal{H}_\alpha/\hbar = \omega_I I_z + 1/2(AI_z) + 1/2(BI_x) \qquad (3.42)$$

By applying the raising and lowering operators, the hamiltonian matrix is simplified and can be diagonalized by means of the rotation operators, $e^{-iI_y\eta}$ and $e^{-iI_y\xi}$. These rotation operators correspond to the transformation matrices M_α and M_β, and can be used to diagonalize the hamiltonian matrix. The use of trigonometric identities comes in handy when solving the matrix. The product of $|v|^2|u|^2$ is then given by,

$$|v|^2|u|^2 = 1/4[\sin^2(\eta-\xi)] \qquad (3.43)$$

A.

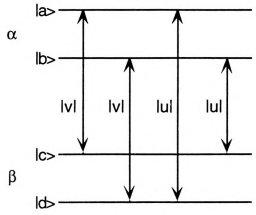

B.

$$\left.\begin{array}{l} |a\rangle \rightleftarrows |c\rangle \\ |b\rangle \rightleftarrows |d\rangle \end{array}\right\} \text{ on the order of } |v|$$

$$\left.\begin{array}{l} |a\rangle \rightleftarrows |d\rangle \\ |b\rangle \rightleftarrows |c\rangle \end{array}\right\} \text{ on the order of } |u|$$

Figure 3.15: A.) This scheme describes the two electron levels α and β, split by the coupling with an I = 1/2 nucleus. B.) The transition matrix elements connecting the states are shown.

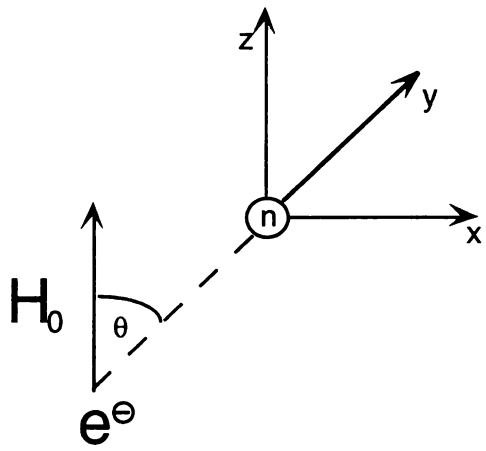

Figure 3.16: Transformation rotation where θ describes the relationship between the two axes.

This equation can then be related to the frequencies ω_I, ω_α and ω_β. More algebraic manipulations and trigonometric substitutions using half angle formulas result in,

$$E_{mod}(\tau)= 1 + 1/4\ (\omega_I B/\omega_\alpha\omega_\beta)^2\ [2\cos\omega_{ab}\tau + 2\cos\omega_{cd}\tau - \cos(\omega_{ab}- \omega_{cd})\tau - \cos(\omega_{ab} + \omega_{cd})\tau] \qquad (3.44)$$

where $(\omega_I B/\omega_\alpha\omega_\beta)^2$ is the modulation depth parameter, k. This term B within k contains in it the dipolar component of the hyperfine interaction. In addition,

$$w_\alpha = w_{ab} = \left[(A/2 + w_I)^2 + B^2/2)^2\right]^{1/2}$$
$$w_\beta = w_{cd} = \left[(A/2 + w_I)^2 + B^2/2)^2\right]^{1/2} \qquad (3.45)$$

This equation is the functional form of the modulation expression. The expression describing the 3-pulse modulation function,

$$E_{mod}(\tau+T)= 1 - (2\omega_I^2B^2/\omega_{ab}^2\omega_{cd}^2) \{\sin^2\omega_{ab}\tau/2 [(1-\cos\omega_{cd}(\tau + T)] + \sin^2\omega_{cd}\tau/2[(1-\cos\omega_{ab}(\tau+T)]\} \quad (3.46)$$

It can be seen that if the nuclear zeeman interaction, ω_I, is equal to the hyperfine interaction, then the maximum modulation depth will occur. Note also that there are sum ($\omega_{ab} + \omega_{cd}$) and difference ($\omega_{ab} - \omega_{cd}$) frequencies that do not appear in the modulation function for the 3-pulse modulation function (Mims, 1972b).

EPR Instrumentation

cw-EPR

The first detection of an EPR signal was in 1945 by the Russian scientist, Zavoiskii. The effect was known for many years, but the technology was not developed until World War II and the development of radar. Upon the arrival of microwave technology, components became available to design and build spectrometers. There are three major components in a spectrometer: the microwave source, the sample cavity and the detector. The microwave radiation source is the klystron and it is housed in the microwave bridge. As opposed to a conventional light source, the klystron (resonant source) puts out a narrow frequency range

only. Gunn-diodes, an alternate microwave source, have an extended wavelength range and are more tunable, but they are quite noisy. The sample cavity in general, is a gold plated silver box (which contains a set of Helmholtz coils) that helps amplify weak signals from the sample. The microwave diode detector is used to detect the reflected microwaves which are then converted to an electrical current. A reference arm supplies the detector with extra microwave power or bias. Some of the power originating from the source is funneled into the reference arm, where the attenuator controls the power level and thus consequently the diode current, for optimal performance. Other components consist of a magnet, the signal processing and signal enhancement electronics and an isolator which keeps back reflections from coming into the klystron, and separates the source from the rest of the circuit. The laboratory magnetic field is modulated by coils inside of the cavity to yield a second AC field. When the resonance condition is satisfied, microwave power is absorbed by the sample. Because the experiment is carried out with a fixed source frequency, the spectrum is generated by measuring the microwave power absorbed by the sample as a function of the magnetic field strength. When the sample absorbs the microwave energy, the Q is lowered since the samples absorb due to an increase in loss and consequently the impedance of the cavity. Microwaves are then reflected back into the microwave bridge (Figure 3.17), resulting in an EPR signal.

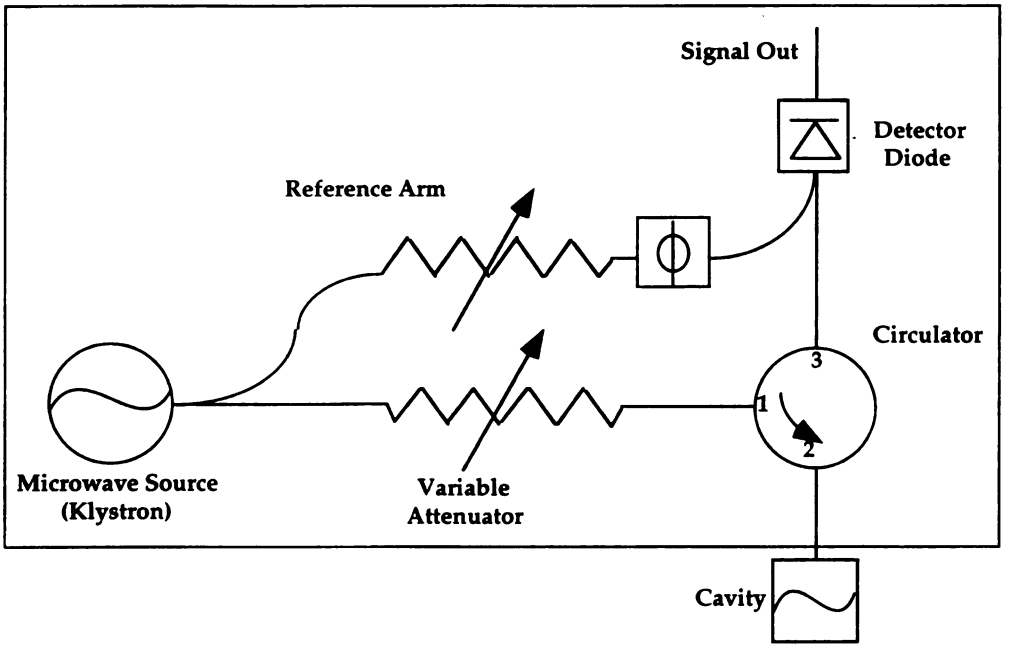

Figure 3.17: Basic diagram of the microwave bridge components.

The Michigan State University ESEEMometer

The instrument was built in 1990 by John McCracken. Over the years there have been some modifications made to the instrument by Professor McCracken as well as by Dr. Hong-In Lee. Explicit details were published elsewhere (Lee, 1994, McCracken *et al.*, 1992).

The source for the instrument is a Gigatronics model 610 microwave synthesizer which runs at GHz frequencies. There are two pulse channels consisting of a high-speed diode switch and phase

modulator. A directional coupler divides the source output so that 10% of the microwave power is directed to the two pulse arms while 90% is directed to a reference arm. The pulse widths and phases of each channel are controlled by a logic box, home built by Dr. Lee, with capabilities of up to six pulses. The instrument is controlled by a Mac II microcomputer with data collection written in the C (Symantec) computer language. Sophisticated software for data analysis is written in the MATLAB® language via a SPARC SUN workstation. The spectrometer is currently being switched over to an Apple Power Computing 150 microcomputer to run with LABVIEW® software. The computer is interfaced to a SRS model SR245 I/O module and a model DG 535 delay generator which controls accurate timing signals, the pulses and their spacings.

One of the great things about building your own instrument is the versatility it can have. This ESEEM spectrometer currently has the capabilities of performing 2-pulse, 3-pulse, and 4-pulse experiments. It can perform Hyperfine sublevel correlated spectroscopy (HYSCORE), pulsed ENDOR, both Mims and Davies, single crystal rotation studies, double electron-electron spectroscopy.

BIBLIOGRAPHY

Abragam, A., & Bleaney, B. (1970) **Electron Paramagnetic Resonance of Transition Ions**, Vol. , Dover, New York.

Carrington, & McLachlan (1979) **Principles of Magnetic Resonance**, Vol. , 2 ed., Wiley, New York.

Cohen-Tannoudji, C., Diu, B., & Laloë, F. (1977) **Quantum Mechanics**, Vol. I & II, 1 ed., John Wiley & Sons, New York.

Lee, H.-I., **Electron Spin Echo Envelope Modulation Studies of Some Transition Metal Model Complexes.**, 1994.

McCracken, J., Shin, D.-H., & Dye, J. L. (1992) *Applied Magnetic Resonance 3*, **Pulsed EPR Studies of Polycrystalline Cesium Hexamethyl Hexacyclen Sodide**, 305-316.

Mims, W. B. (1972a) *Physical Review B 6*, **Amplitudes of Superhyperfine Frequencies Displayed in the Electron-Spin Echo Envelope.**, 3543-3545.

Mims, W. B. (1972b) *Physical Review B5*, **Envelope Modulation in Spin Echo Experiments**, 2409-2419.

Slichter, C. P. (1990) **Principles of Magnetic Resonance**, Vol. 1, 3 ed., Springer-Verlag, New York.

Wertz, J. E., & Bolton, J. R. (1986) **Electron Spin Resonance: Elementary Theory and Practical Application.**, Vol. , 2 ed., Chapman and Hall, New York.

Chapter 4

Interesting Magnetic Behavior of the Electride: $Li^+(C211)e^-$

Evidence for 1-Dimensional Spin Waves

Introduction

The interest in the paramagnetic films or powders left behind after rapid evaporation of liquid ammonia from solutions of alkali metals and cryptands, has lead to extensive studies[†]. Following this observation, the pursuit for *crystalline* electrides with well-defined properties has been long and arduous. The solutions of interest contain lithium cations encapsulated in a cryptand [2.1.1] cage, C211, with the remaining unpaired electrons solvated. Many participants of the Dye group have studied electrides over the years to try to understand better the elusive electrons in electrides. Li^+ has an ionic radius of 0.6 Å and the diameter of C211 is 1.2 Å so one might predict good complexation. $Li^+(C211)e^-$ has a history of being very thermally unstable and was therefore very difficult to synthesize without decomposition. It wasn't until Dr. Rui Huang mastered this synthesis, that crystals were made and the structure was determined. With the advent of good crystal growth, it was necessary to repeat the studies, and here we try to obtain an understanding of the magnetic behavior and see if a correlation can be made with the crystal structure. It turns out that each of the other four electrides have very

[†]For a recent review article of alkalides and electrides, see (Wagner & Dye, 1996) and the references therein.

different properties from one another, so it was thought that this electride may also have unique properties. Since the nature of the electron density distribution is important to the magnetic properties of electrides, EPR results played an important role.

Previous Studies

The electride, $Li^+(C211)e^-$, was first studied in 1981 as the residue obtained by evaporating ammonia from solutions with various ratios of lithium to C211 (Landers *et al.*, 1981) Initially, the magnetic susceptibility, optical absorption and EPR properties of $Li^+(C211)e^-$ were performed on powders of stoichiometry $(Li)_x(C211)$, where x ranged from 0.6 to 2. The samples were made by rapid solvent evaporation from solutions of Li and C211 in liquid ammonia at 195 K. These data demonstrated the presence of at least two major electron-trapping sites in various samples. These sites were distinguished by magnetic susceptibility data that revealed either a single peak at ~ 20 K, or alternatively, a broad maximum at 50-60 K. The EPR signal intensity showed that the latter samples contained both the "20 K site" and the second site. The difference in behavior was again attributed to differences in the mole ratio of lithium. It was not clear however whether or not a single phase had two electron sites, or if two different phases were responsible. Figure 4.1 shows the difference in optical spectra with mole ratios at the extrema of 0.60 and 1.57.

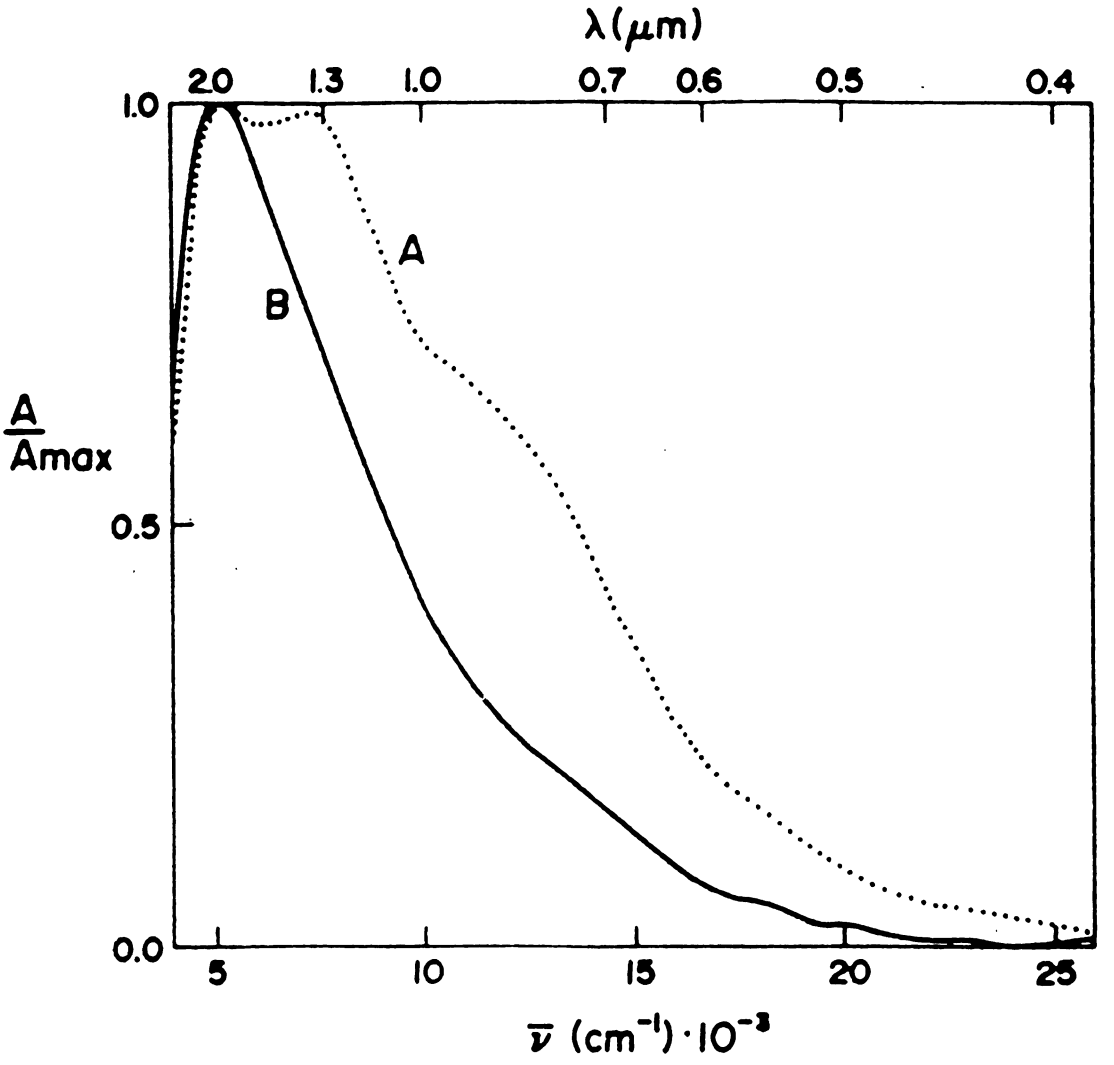

Figure 4.1: Optical spectra of Li+(C211)e- from liquid ammonia solutions of Li:C211 ratios of A) 0.60 and B) 1.57. When this ratio is up to 1.15, the optical spectrum was the same as spectrum A.

Synthetic Considerations

There are a few fine points that deserve mentioning regarding the synthesis of this thermally unstable electride. Most alkalide and electride syntheses are quite similar in nature, except the solvents and starting materials change accordingly. They all require specialized glassware and in this synthesis, a three chamber quartz K-cell is used. The quartz insures that there is little chance for sodium (natural in Pyrex®) to exchange with the lithium, resulting most likely in a sodide. The third chamber was used to dissolve the lithium metal. The other alkali metals can all be distilled with a torch under vacuum to form a nice mirror on the surface of the bulb, but lithium must be dissolved. A fine quartz frit is used between the third, metal dissolving chamber, and the reaction chamber, to filter out any possible impurities such as iron or lithium nitrides that may have formed in the glove box. The complexant, C211, was obtained from Aldrich (98%) and was vacuum-distilled prior to use. A lithium ingot (under argon) from AESAR (99.9%) was kept in a helium-filled glove box and subsurface samples were used to provide weighed, shiny samples of lithium metal. Initially, $MeNH_2$ or NH_3, was used to dissolve the lithium (I personnaly preferred $MeNH_2$). If one was feeling brave, the third chamber was sealed off and removed from the cell, but this was not a necessary step. The dissolved metal was then reacted with the

complexant in the first bulb and left to react for a few hours. There was a trade off in this reaction time as the longer the reaction occurs, the better the yield, but the greater the chance for decomposition. The $MeNH_2$ was removed followed by several rinses with Me_2O to ensure that all of the $MeNH_2$ was evaporated. This was important because a number of lithium sodides have been made with the solvent $MeNH_2$ included in the crystal structure. A final portion of Me_2O was added to the vessel to dissolve the electride. The second solvent, Et_2O, was used to make a saturated solution and the solution was then poured over to the center bulb containing the collection fingers. Only about 36 hours were needed to evaporate the solvent through 2-3 frits. One important point is that the whole experiment should only take about two and a half days. This will help minimize the chances of decomposition.

The crystals have a shiny appearance and have either a "blocky" or needle-like morphology. This procedure usually resulted in the growth of crystals up to 0.5 mm edge length when the initial solution was poured through the frit, leaving behind any precipitate. When precipitate was formed in the crystal growing chamber prior to distillation, an amorphous powder with no apparent crystallinity was present, along with crystals. Moreover, when samples were prepared by rapidly evaporating the saturated solution, the powdered material was usually produced. Because this electride is extremely subject to irreversible decomposition,

the temperature was always kept at or below 223 K during synthesis and handling. In addition, NMR spectra of decomposed material showed that this electride also decomplexes.

One question arises with regard to this synthesis. In a traditional alkalide/electride synthesis, the stoichiometry is very important, but in this synthesis, one can change the ratio of Li:C211 drastically and still make only electride. To date, there has never been a *lithide* synthesized in the Dye group. The reaction,

$$Li^- \rightleftharpoons Li^+ + 2e^-_{solv} \qquad (4.1)$$

lies far to the right which would minimize the presence of Li^- in solution, a requirement for a lithide synthesis . This equilibrium may be due to the large solvation energy of Li^+. In addition, the relative stability of crystalline lithides compared to electrides, has been extimated to have a positive $\Delta G°$ (Wagner & Dye, 1996).

Structural Facts

Due to the new synthesis methodology, the source of the two kinds of magnetic behavior recently became clear. It seems that the properties and magnetic behavior of the two distinct phases of this electride originate from one form, the crystal structure, and another powder phase of unknown structure. The data throughout this chapter will support this

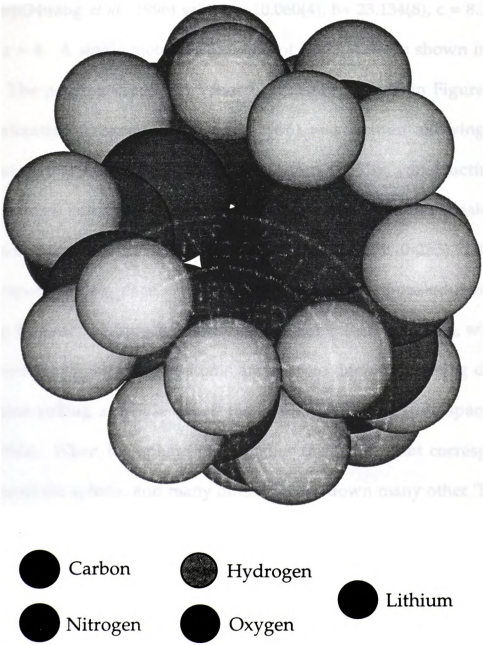

Figure4.2: Space-filling model of one molecule of $Li^{+}(C211)e^{-}$.

assumption. This electride crystallizes in the orthorhombic crystal system(Huang *et al.*, 1996) with a = 10.060(4), b= 23.134(8), c = 8.380(4) Å and z = 4. A single molecule drawing of $Li^+(C211)e^-$ is shown in Figure 4.2. The packing diagram of four unit cells is shown in Figure 4.3. A visualization program (Dye *et al.*, 1996) was written allowing one to envision the empty regions within a crystal by constructing a 3-dimensional cubic grid. The distance to the nearest van der Waals atomic or molecular surface is given a number (between 0-255) defining a corresponding distance. The crystal structure is imported directly by using Biograf® or Biosym® software and some 8-27 unit cells, where the van der Waals radii of the atoms are used to devise a packing diagram. Imagine rolling a sphere down the "halls" of the negative space in the electride. When the sphere just touches the "wall", that corresponding radius of the sphere, and many other spheres down many other "halls", is mapped out. In other words, the location of a sphere that would just touch the atomic surface, is charted. An isosurface routine is used to display the 3-dimensional contour diagram. To find distance parameters, the distance number is changed until the feature just disappears to determine the maximum diameter of a sphere that would just pass through the *channel*, or just fit inside of the *cavity* (Figure 4.4). That parameter is then used to calculate a real width. Interior details can be obscurred when a smaller distance parameter is chosen, but it is a more

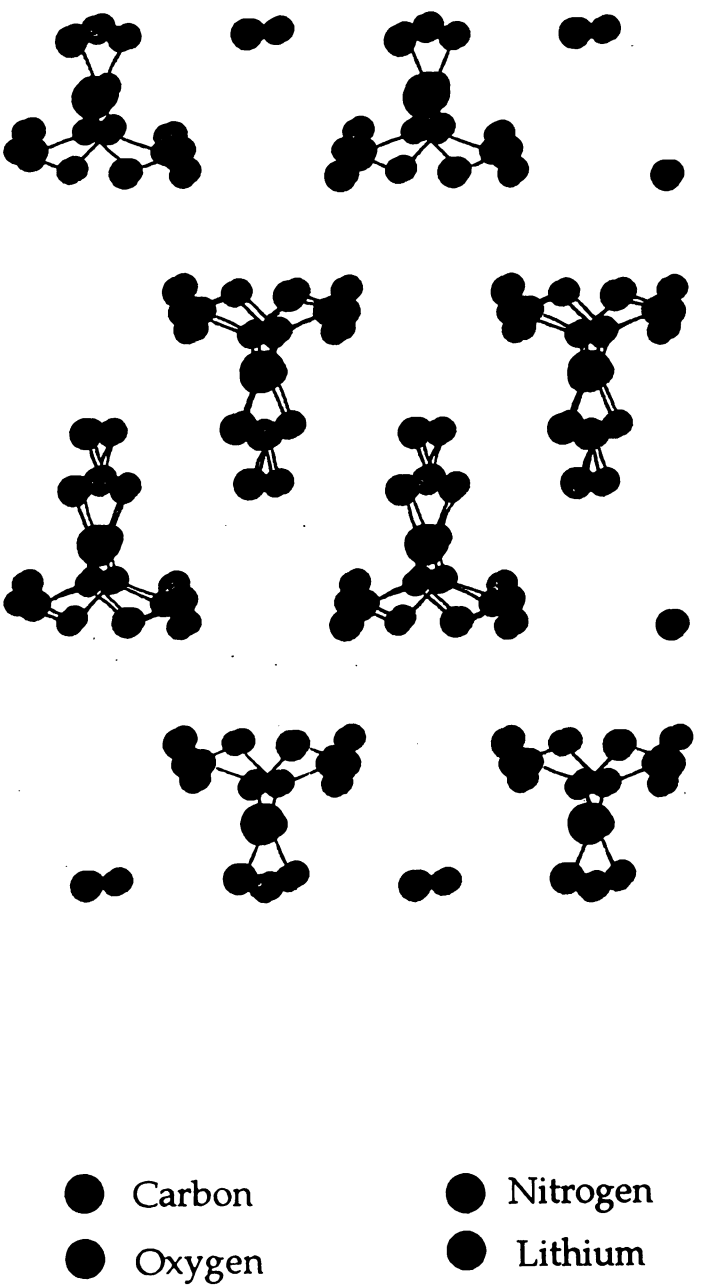

Figure 4.3: Representation of the packing of four unit cells of $Li^{+}(C211)e^{-}$.

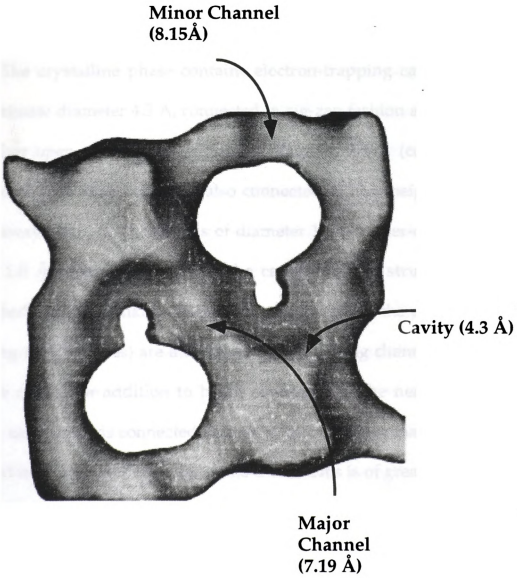

Figure 4.4: Channel and cavity diagram of $Li^{+}(C211)e^{-}$.

realistic view of the channel and cavity shape. As a compromise, a larger distance parameter is chosen resulting in some minor distortions in the cavities and channels, but the interior view is much more apparent.

The crystalline phase contains electron-trapping cavities, each of approximate diameter 4.3 Å, connected in zig-zag fashion along the *c* axis by rather open channels of minimum diameter 2.4 Å (center-to-center distance 7.9 Å). Each cavity is also connected to next-neighbor cavities, 8.2 Å away along *c*, by channels of diameter 1.5 Å. Inter-chain channels are < 1.0 Å in diameter so that the cavity-channel structure is well-described as "ladder-like". The structure shows that the excess electron trapping sites (cavities) are interconnected by zig-zag channels to form an infinite chain. In addition to being connected to the nearest neighbor cavity, each cavity is connected further by a somewhat smaller channel to the next nearest neighbor cavity in the chain. This is of great interest since the structure suggests essentially 1D magnetic coupling between not only the nearest neighbors in the linear chain, but also to next-nearest neighbors.

Properties of Newly Synthesized $Li^+(C211)e^-$

The packed powder dc conductivity of $Li^+(C211)e^-$ from 120 K to 230 K followed semiconductor-type behavior with an apparent band gap of 0.44 eV (Huang *et al.*, 1996, Wagner, 1994). The ^7Li NMR spectra (Huang

et al., 1996, Wagner, 1994) of a number of samples confirm the presence of two types of samples that have different environments for Li^+. NMR studies of finely crushed crystals of $Li^+(C211)e^-$ display an inverse relationship between the chemical shift and the temperature. The chemical shift varies from +70 ppm at 170 K to +56 ppm at 230 K. The percent atomic character of ^7Li due to contact density of the unpaired electron at the lithium nucleus is 0.16%, obtained by using an unpaired electron density for the gaseous lithium atom of 1.56×10^{24} $e \cdot cm^{-3}$ (O'Reilly, 1964). The powder phase of $Li^+(C211)e^-$ has a different ^7Li NMR. The chemical shift shows a linear relationship with inverse temperature with 0.08% atomic character. The optical spectra of thin, solvent-free films of $Li^+(C211)e^-$ obtained by slow evaporation of ammonia and shown in Figure 4.1, have been reproduced but the origin of the different spectra is understood better. It now appears that the sample labeled B (R = 1.57) in that work is what we now refer to as the 'powder' sample. It shows a single optical absorption peak at 2.0 μm and may have contained both powder and crystalline phases. Films obtained in the present work by evaporating dimethyl ether from a solution of the electride showed a broad peak at 1.5 μm and an extended "tail" through the visible. The DSC measurements revealed the onset of decomposition at about 270 K. The decomposition was very exothermic and exhibited

"runaway" behavior, typical of autocatalytic decomposition. No thermal transitions were observed in the electride between 173 and 270 K.

Brief Magnetism Primer

Since the magnetic moment of an electron is three orders of magnitude greater than a proton, magnetic effects arise mainly from the electrons. The unpaired electrons of a paramagnetic system can occupy certain orbital arrangements and the magnetic behavior as a result of this, can be described by measuring the magnetic polarization. Various behaviors are illustrated in Figure 4.5. The magnetic induction, B can be used to describe the behavior of a system in a magnetic field.

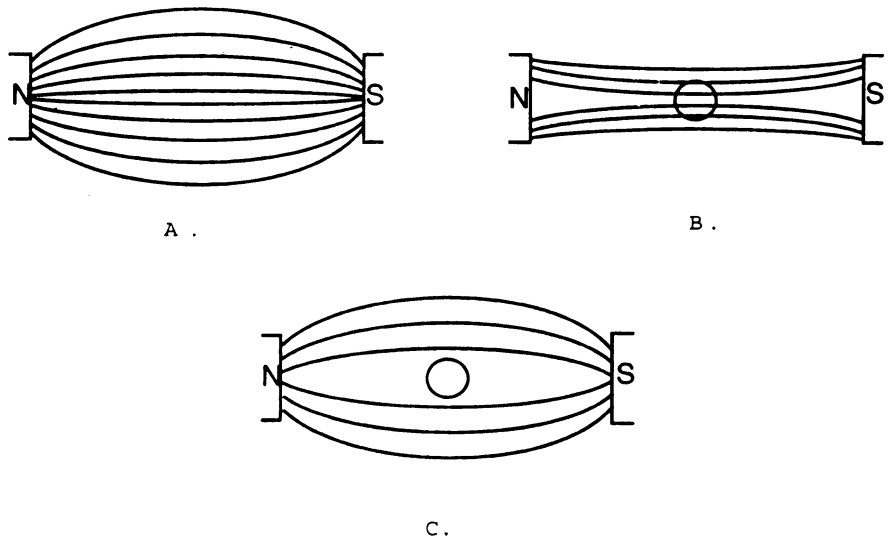

Figure 4.5: Magnetic flux lines in A) a vacuum, B) paramagnetic substance in a magnetic field, C) diamagnetic substance in a magnetic field.

$$\vec{B} = \vec{H}_o + 4\pi\vec{M} \qquad (4.2)$$

where $\vec{H}_o$ is the applied magnetic field strength and $\vec{M}$ is the magnetization. Dividing* both sides by $\vec{H}_o$,

$$\frac{B}{H_o} = 1 + \frac{4\pi M'}{H_o} \qquad (4.3)$$

where M'/H_o is by definition the magnetic susceptibility per unit volume, χ_v. Therefore, $\chi_v = M'/H_o$ is a dimensionless unit. Subsitituting the volume susceptibility in the equation and knowing the mass of the material, the molar susceptibility χ, can be obtained. There are several different types of magnetism: diamagnetism, paramagnetism, antiferromagnetism (AF) and ferromagnetism, to name a few. By convention, χ is negative for diamagnetic substances and positive for paramagnetic substances. The susceptibility behavior is often studied as a function of the temperature (Figure 4.6). Due to small susceptibilities, AF materials were originally believed to be anomalous paramagnets (Jakubovics, 1987). Some paramagnetic solids do go through a phase transition as the temperature is lowered, in which large domains of spins align with parallel or anti-parallel orientations. When the spins alternate

*After the division, only the magnitude appears after the directional properties of the vectors are factored out.

their respective orientation, they are locked in an arrangement of low magnetization to produce an AF phase. The characteristic temperature at which the spins lock into that arrangement is known as the Neél temperature.

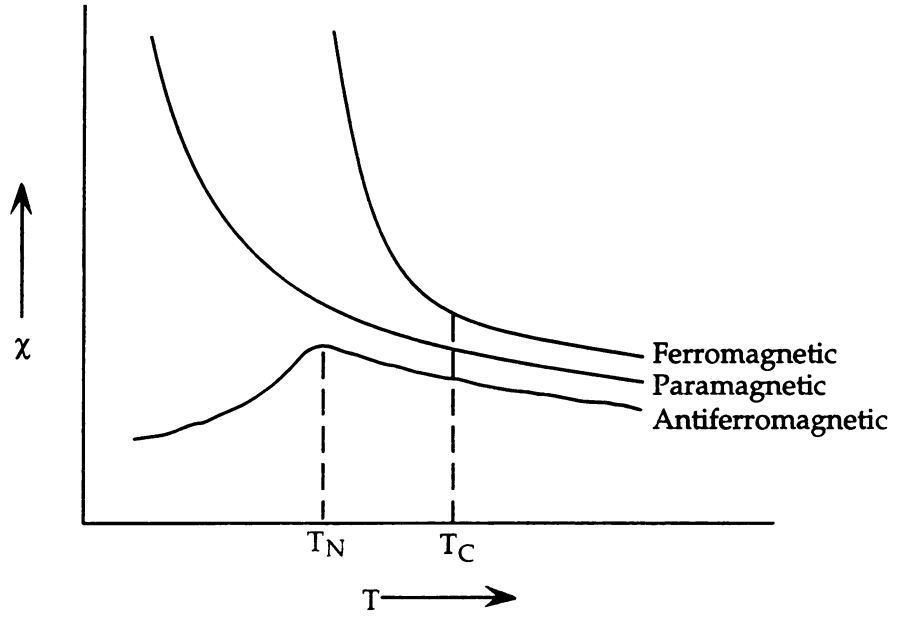

Figure 4.6: Susceptibility as a function of the temperature for antiferromagnetic, paramagnetic and ferromagnetic materials. T_N represents the temperature at which the maximum occurs in antiferromagnetic material and T_C is the temperature at which the break occurs in ferromagnetic material.

The susceptibility is derived from the force an applied field exerts on a sample and it measures the degree by which the measuring field tends to align the spin system with it. When one refers to the dimensionality of a system, it is not necessarily the space dimensionality. The spin dimensionality arises from the interaction of the spins of several

interacting ions. It can be defined by the expansion of the exchange term in the spin Hamiltonian,

$$\mathcal{H} = -2J\sum_i \mathbf{S}_i \cdot \mathbf{S}_{i+1} \qquad (4.4)$$

and can be expanded for an infinite chain of identical Heisenberg spins with first and second nearest neighbor interactions,

$$\mathcal{H} = -2J_1\sum_i \hat{S}_i\hat{S}_{i+1} - 2J_2\sum_i \hat{S}_i\hat{S}_{i+} \qquad (4.5)$$

where J measures the strength of the interaction between the spins. A magnetic linear chain is often restricted to adjacent sites and is a summation over all of the lattice sites i and j. This Hamiltonian is expanded to give,

$$\mathcal{H}_S = -2J\ \mathbf{S}\ (\alpha S_{iz}S_{jz} + \beta[S_{ix}S_{jx} + S_{iy}S_{jy}]) \qquad (4.6)$$

Ising found that a system considered infinitely long undergoes long-range order only at absolute zero (Ising, 1925). Likewise, a Heisenberg (isotropic) system does not order at finite temperatures. All known 1-dimensional (1D) systems do, in reality, interact and undergo long-range order, since interchain interactions become more important as the temperature approaches absolute zero. There are three different combinations of α and β and each has its own model to describe the particular arrangement of spins. The model that is considered in this text

is the Heisenberg model. The Heisenberg model has no exact or closed-form solution for a linear chain Heisenberg AF with S=1/2. Extrapolations however, can be made to fit the expression (Estes *et al.*, 1978),

$$\chi_m = \frac{Ng^2\mu\beta^2}{kT}\left[\frac{0.25 + 0.14995y + 0.30094y^2}{1 + 1.9862y + 0.68854y^2 + 6.0626y^3}\right] \qquad (4.6)$$

where $y = |J|/kT$. This equation is then modified to correct for temperature independent paramagnetism and the "Curie tail".

The spin-Peierls Transition

Most magnetic systems enter a phase of long-range order, such as antiferromagnetism or ferromagnetism at a particular temperature. When the system is lowered through this temperature, the transition occurs. If this system follows an ideal one dimensional model where the interactions are short range, order can occur but only if the temperature is equal to zero (Bray *et al.*, 1983). Quasi one-dimensional systems are those that have non-zero transition temperatures due to weak interchain interactions. Exchange coupled spins on a rigid lattice are best described by the quasi one-dimensional model. If the lattice is somewhat flexible, a new type of ordering can occur at low temperatures. This more ordered transition is called a **spin-Peierls** transition in antiferromagnetic

materials. This transition marks the onset of a progressive spin-lattice dimerization in a system of quasi-1D AF chains. A uniform AF chain has been shown to be unstable towards dimerization into an alternating antiferromagnet (de Jongh, 1988). When the temperature is greater than the onset temperature (T_{sp}), the system behaves as an assembly of uniform AF chains. When the temperature is lowered below the transition temperature, elastic distortions in the lattice progress leading to an energy gap which becomes > 0 at T_{sp}. When T = 0, the energy gap is a maximum.

Suseptibility Data

The temperature and field dependence of the susceptibility were determined by Dr. Deborah Gilbert, with a Quantum Design SQUID magnetometer. $Li^+(C211)e^-$ samples, in a dry nitrogen glove bag at about 200 K, were crushed in a cold mortar, then carefully loaded into specially assembled Kel-F® covered buckets. The bucket dimensions were chosen so that it fit within a plastic straw sample holder and threads were attached to the bucket to hold it in a fixed position. Samples were maintained in the absence of air at 223 K or below at all times. The SQUID measurements of $Li^+(C211)e^-$, clearly show a drastic downturn in the susceptibility as the temperature is decreased below about 14K. A maximum in the susceptibility of this sample occurs at around 58 K

Figure 4.7: Magnetic susceptibility of A) crushed crystals and B) "powder" of $Li^+(C211)e^-$ as a function of the temperature. The solid line represents a fit by Equation 4.6 modified for the TIP and a "Curie tail". The inset shows an expansion of the low temperature region.

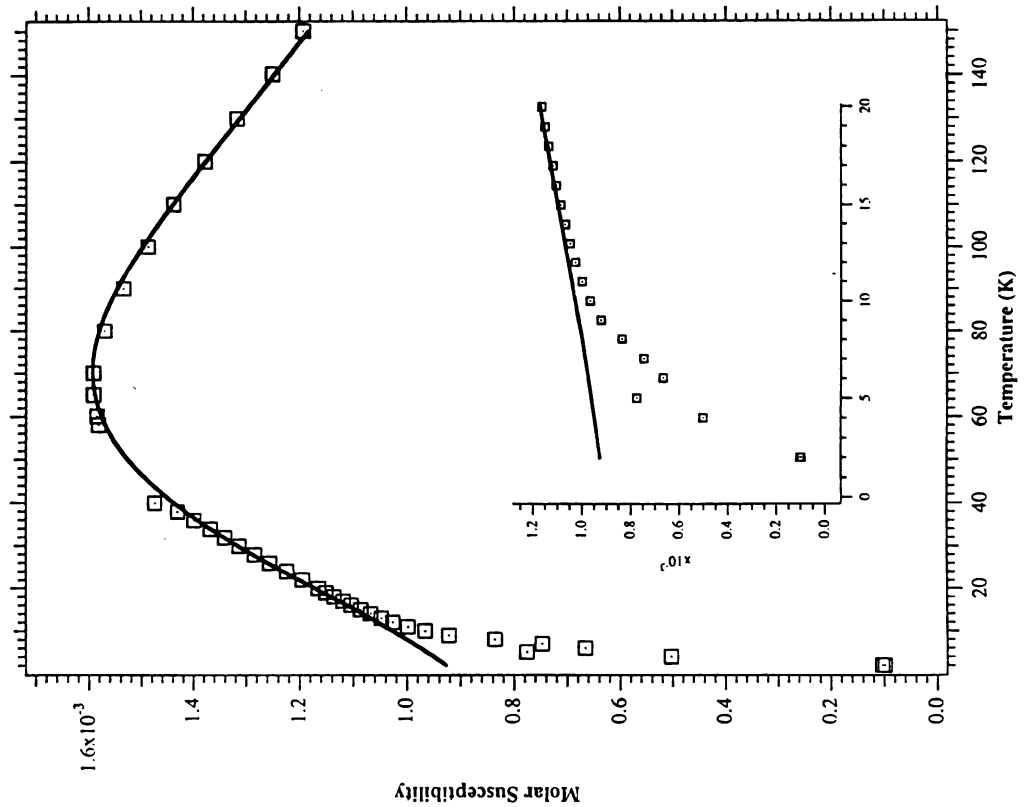
Molar Susceptibility
1.6x10⁻³
1.4
1.2
1.0
0.8
0.6
0.4
0.2
0.0
20
40
60
80
100
120
140
Temperature (K)
x10³
1.2
1.0
0.8
0.6
0.4
0.2
0.0
0
5
10
15
20

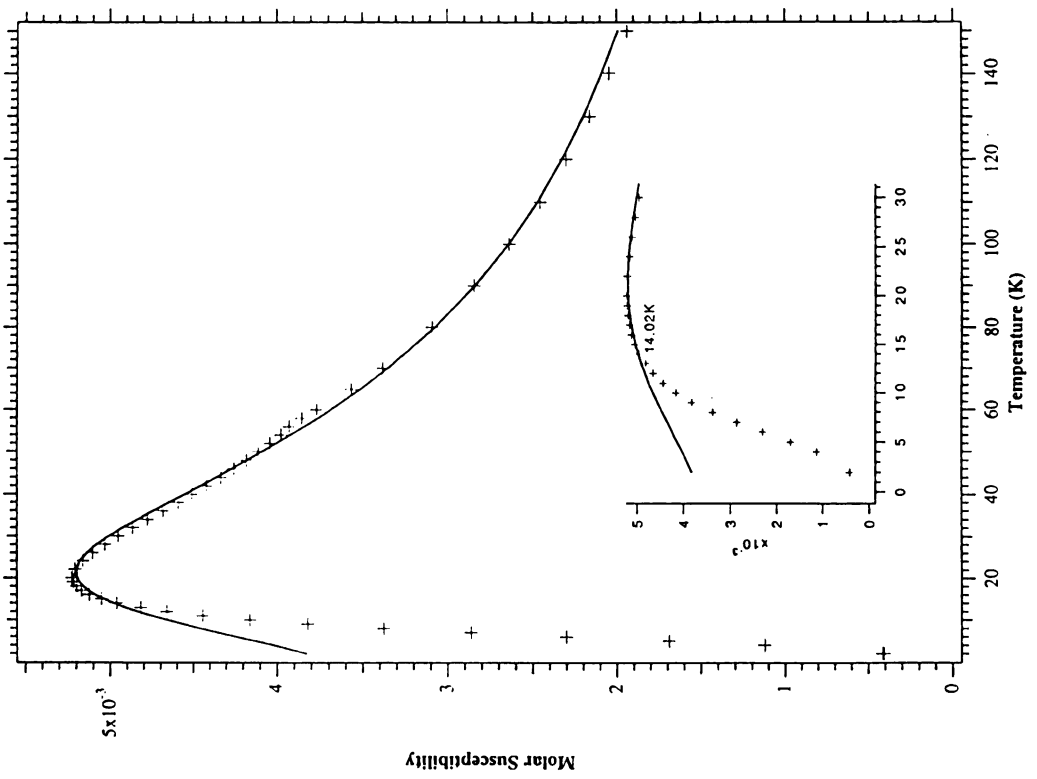
Molar Susceptibility
5x10⁻³
4
3
2
1
0
20
40
60
80
100
120
140
Temperature (K)
x10³
5
4
3
2
1
0
0
5
10
15
20
25
30

(Figure 4.7a). This is consistent with some data obtained previously. Another sample however showed a similar downturn in the susceptibility at 14 K, but the maximum in the susceptibility occurred at 20 K (Figure 4.7b), (also similar to data formerly obtained). After carefully scrutinizing the sample and the preparation, it became evident that these data corresponded to the *crystal* phase and the *powder* phase, respectively. In reality, the data obtained from the four other investigators over the last 15 years was basically the same as that collected recently. Knowing the crystal structure and realizing that there are two possible phases has lead us to the correlation of the presence of "powder-type" and/or "crystal-type" phases. The crystalline samples were checked by using X-ray diffraction before grinding them with a mortar and pestle; thus we were finally able to determine the properties of the form with known crystal structure. This also permitted determination of the magnetic properties of the powder phase, although its structure is not known. It is now apparent that the synthesis can lead to one or both phases of the solid and that very subtle differences in the synthesis methods are responsible.

EPR

The EPR data were collected with a Bruker ESP-300E series spectrometer, operating at X-band. The temperature was controlled to within ±0.1 K with an Oxford 900 series continuous flow cryostat along

with an ITC-4 temperature control unit and a GFS-gas-shielded helium transfer tube. The *g*-value was determined by direct measurement of the magnetic field strength and microwave frequency with an ER-035M NMR gaussmeter and an EIP-25B counter which operates at 3-12 GHz. The $Li^+(C211)e^-$ was checked with a small amount of crushed crystals, ~ 5 mg. The small sample size was necessary to prevent overload of the cavity, making absolute intensity measurements very difficult.

The EPR spectra of $Li^+(C211)e^-$ crystalline samples that are finely crushed exhibit line shapes that depend on the temperature at which the data are collected. At very low temperatures (from 4-10 K) the spectra have broad, weak, featureless line shapes with peak to peak linewidths that range from 1.3 to 1.6 G centered at $g = 2.0021$ (Figure 4.8). At ~10 K, a shoulder appears on the low-field side of the line and this axial lineshape feature becomes more pronounced as the temperature is increased, becoming most well defined at about 25 K. As the temperature was raised above the spin-pairing temperature (14 K) to 25 K, a 100-fold increase in signal strength was found. At this temperature, $g_{//} = 2.00282$ and $g_{\perp} = 2.00246$. As the temperature is increased, the two features begin to coalesce until a single asymmetric line is observed at about 55 K. At and above the susceptibility maximum at 57 K, the signal was exchange narrowed to yield a simple derivative shape with $g = 2.00274$ and a peak-to-peak linewidth of 0.329 G. As the temperature is raised to about 170 K

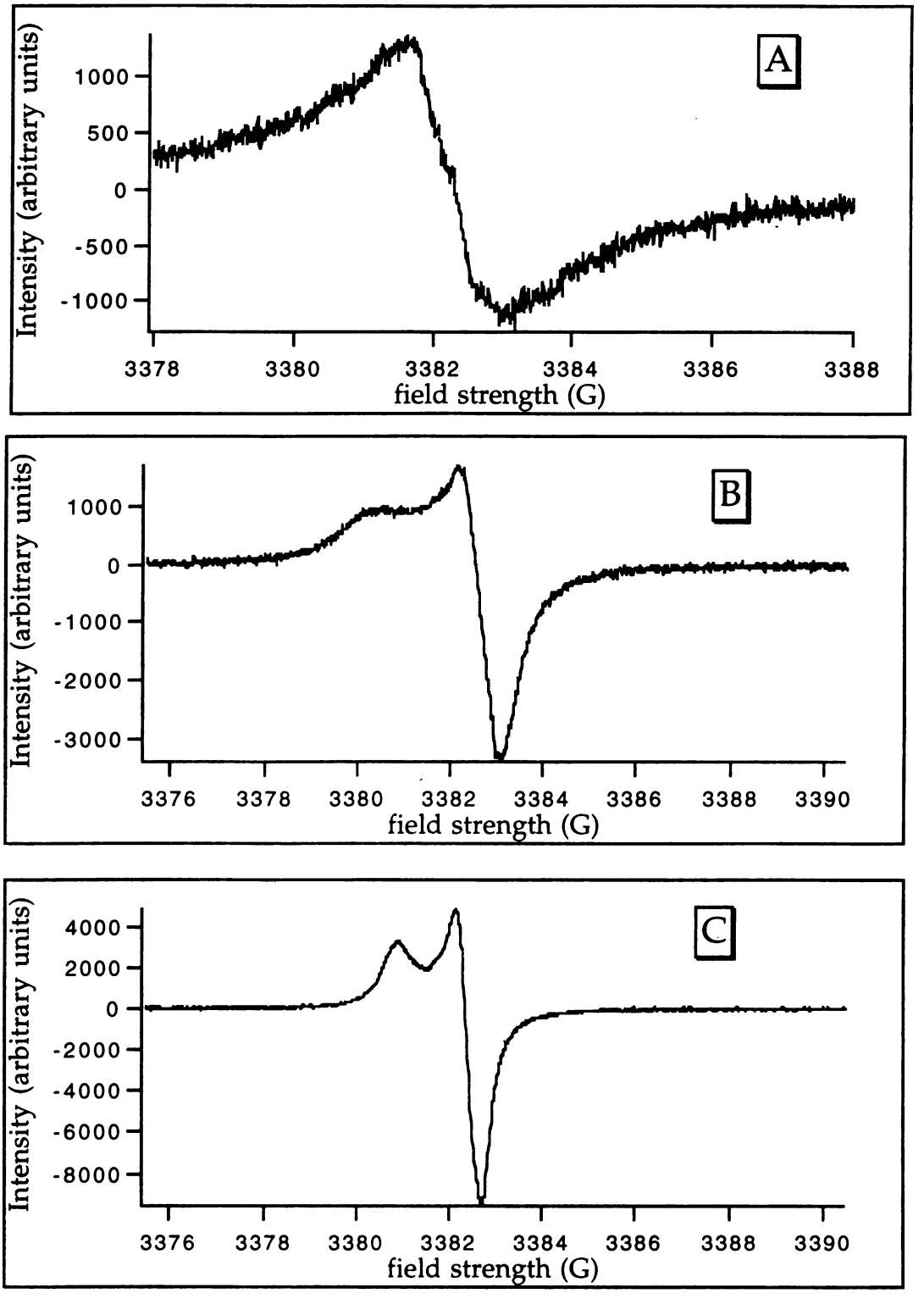

Figure 4.8: EPR spectra collected at 0.04 G/pp MA, 1.56 kHz MF, 0.200 mW microwave power, 1.2 ms tc, A) 4.2 K, $2x10^4$ gain, B) 10.2 K, $1x10^3$ gain, C) 20.5 K, $1x10^3$ gain.

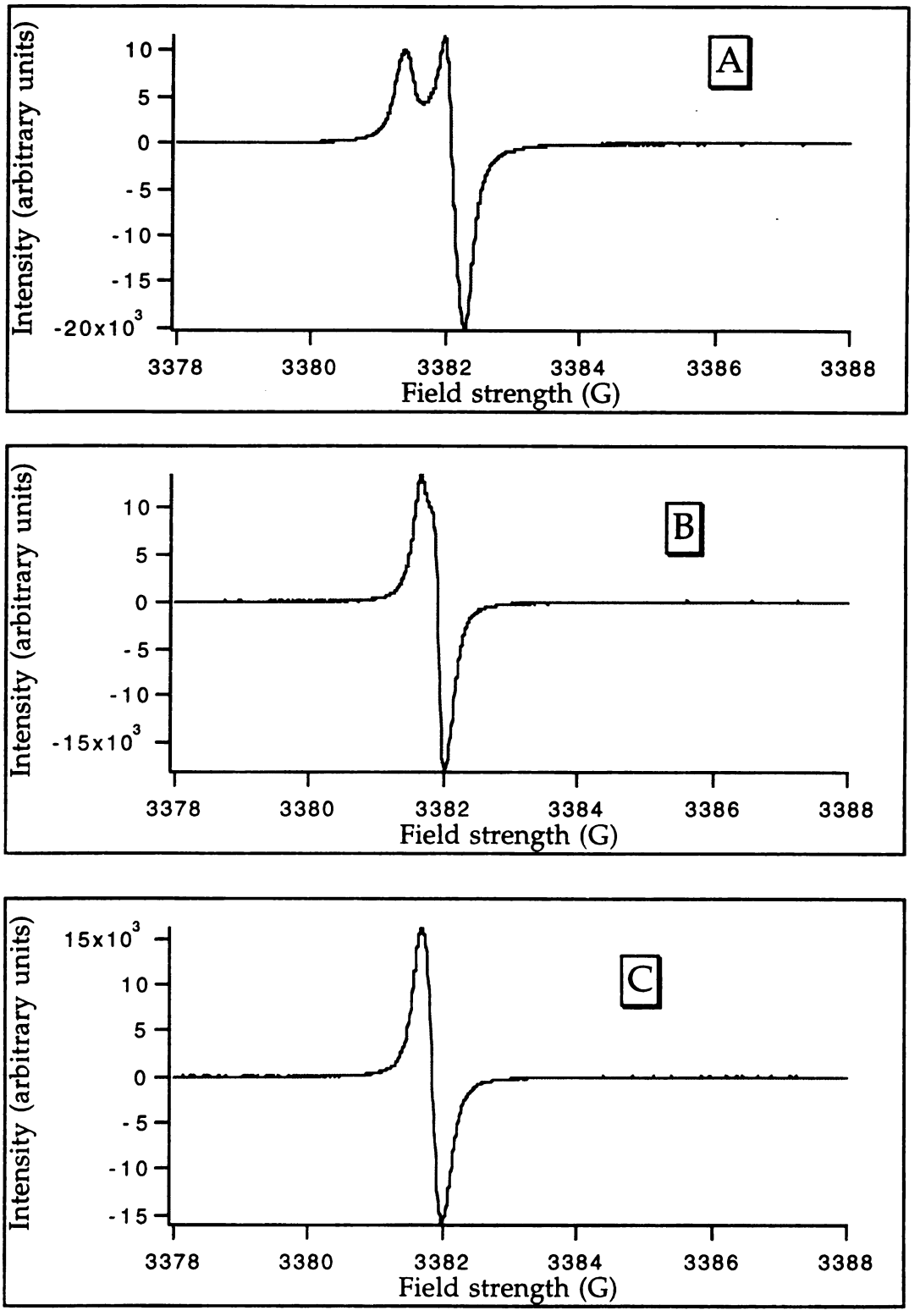

Figure 4.9: EPR spectra collected at 0.04 G/pp MA, 1.56 kHz MF, 0.200 mW microwave power, 1.2 ms tc, A) 26.9 K, $6.3x10^2$ gain, B) 52.3 K, $2.5x10^2$ gain, C) 63.5 K, $2.5x10^2$ gain.

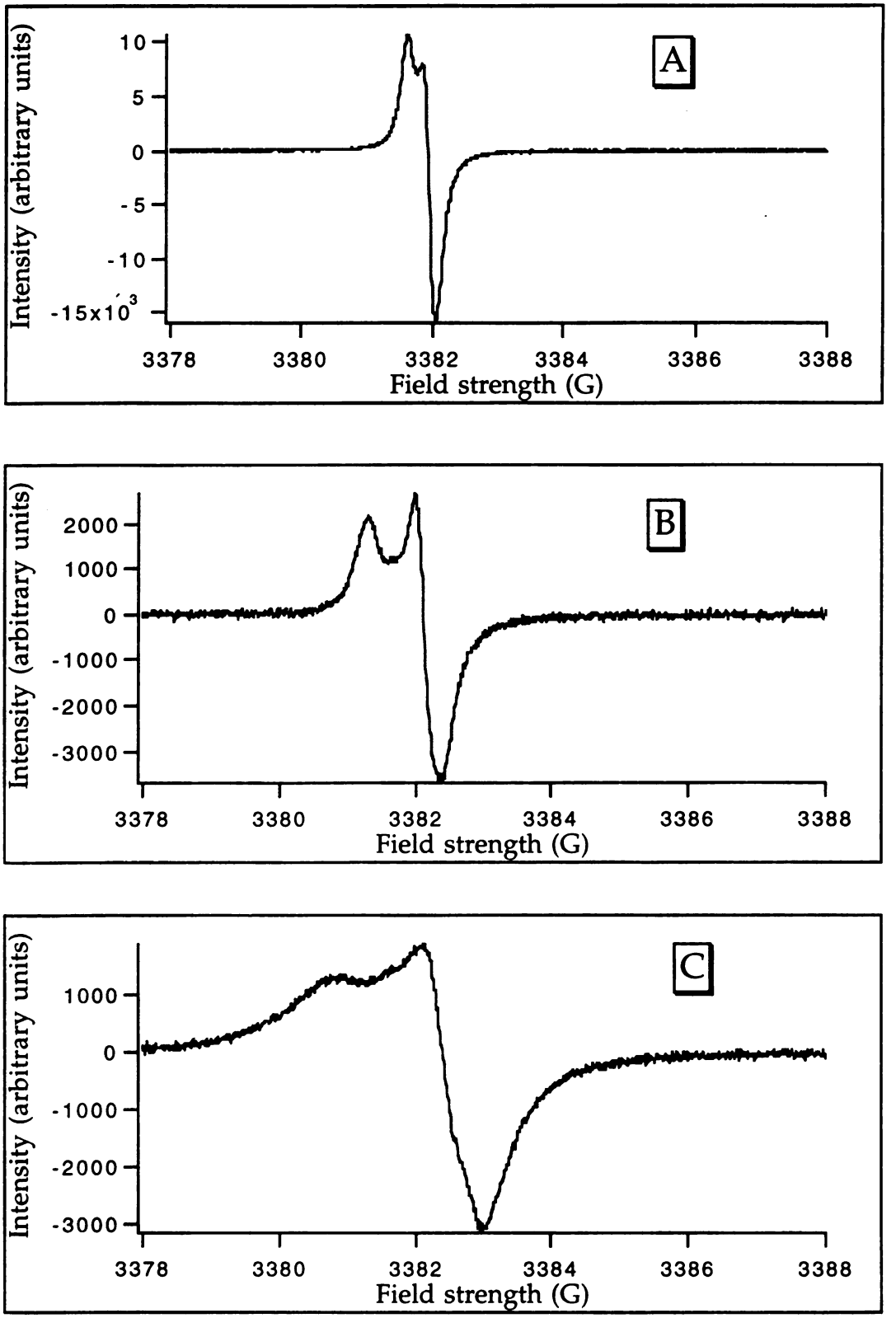

Figure 4.10: EPR spectra collected at 0.04 G/pp MA, 1.56 kHz MF, 0.200 mW microwave power, 1.2 ms tc, A) 50.1 K, $25x10^2$ gain, B) 17.2 K, $2.5x10^2$ gain, C) 10.4 K, $1x10^3$ gain.

(Figure 4.9), the line shape does not change appreciably, but the intensity slowly decreases. When the temperature is then decreased, the axial lineshape begins to form again (Figure 4.10) at a temperature of about 50 K, and at ~23 K the parallel and perpendicular components of the *g*-tensor become the most pronounced with the same *g*-values as reported above. At ~10 K, only a small shoulder remains and this feature is completely lost below this temperature. The peak-to-peak linewidth is once again around 1.39 G. These results demonstrate that the changes in the EPR spectra are reversible.

Double integration of each EPR spectrum and correction for instrument gain yields the relative spin susceptibility as a function of temperature. Such data for the crystalline material and for powder samples are shown in Figure 4.11. These data show that the spin susceptibilities have the same temperature and sample dependence as the bulk susceptibilities obtained from the SQUID measurements.

Pulsed-EPR Measurements

Surprisingly, this electride was able to produce a spin echo, unlike any of the other electrides. For a spin echo to occur, the cw-EPR line must be sufficiently inhomogeneous, as is true when there is resolvable *g*-anisotropy. The ESE-detected EPR spectrum†, revealed a very large

† The electron spin echo (ESE) detected EPR signal is similar to cw-EPR but there is no field modulation. The amplitude of a 2-pulse spin echo is detected as a function of the magnetic field.

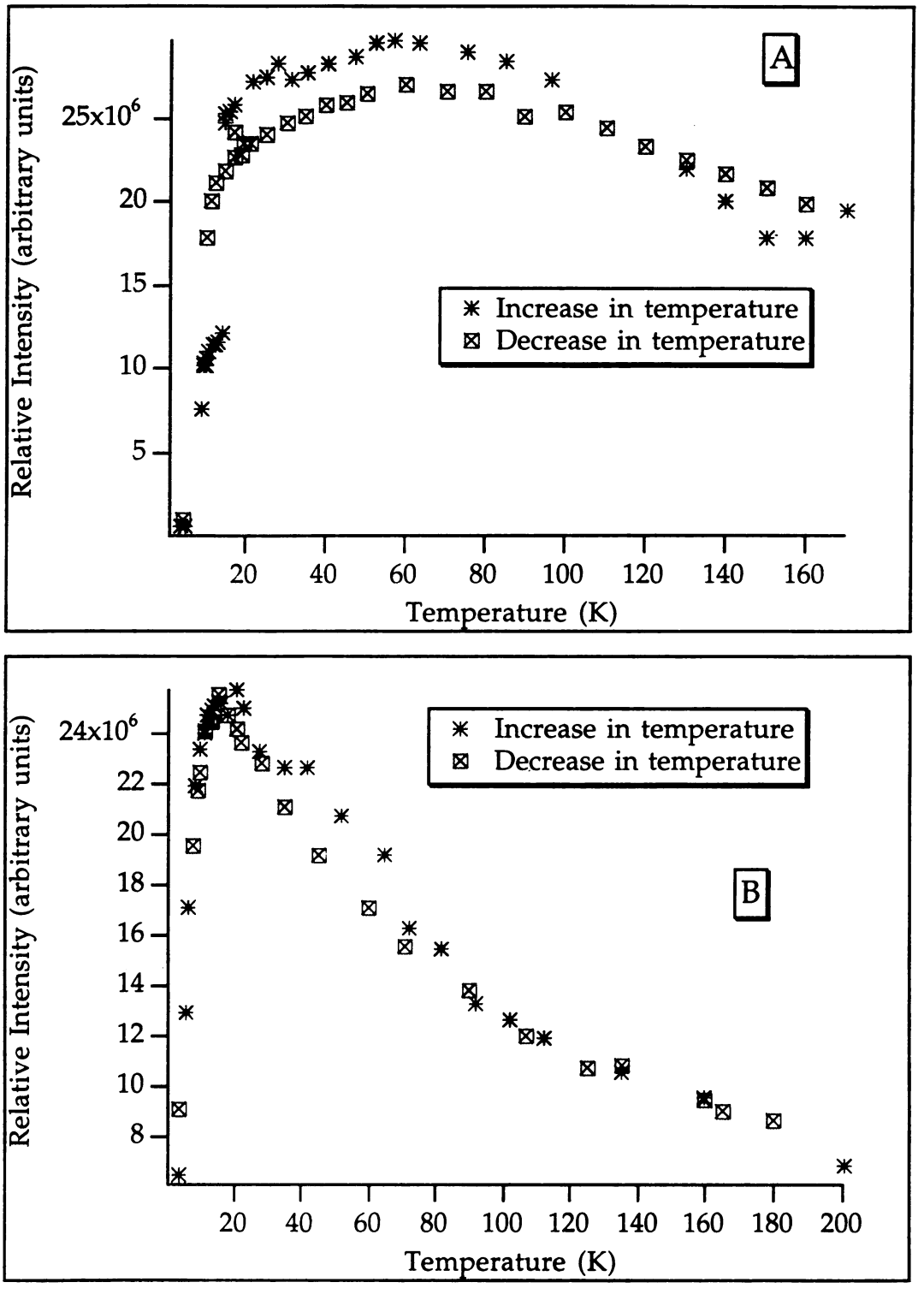

Figure 4.11: Relative intensity of the EPR resonance as a function of the temperature for A) cruched crystals and B) powder samples. These data are reflective of the spin susceptibility and can be related to the bulk susceptibility measured inthe SQUID susceptometer.

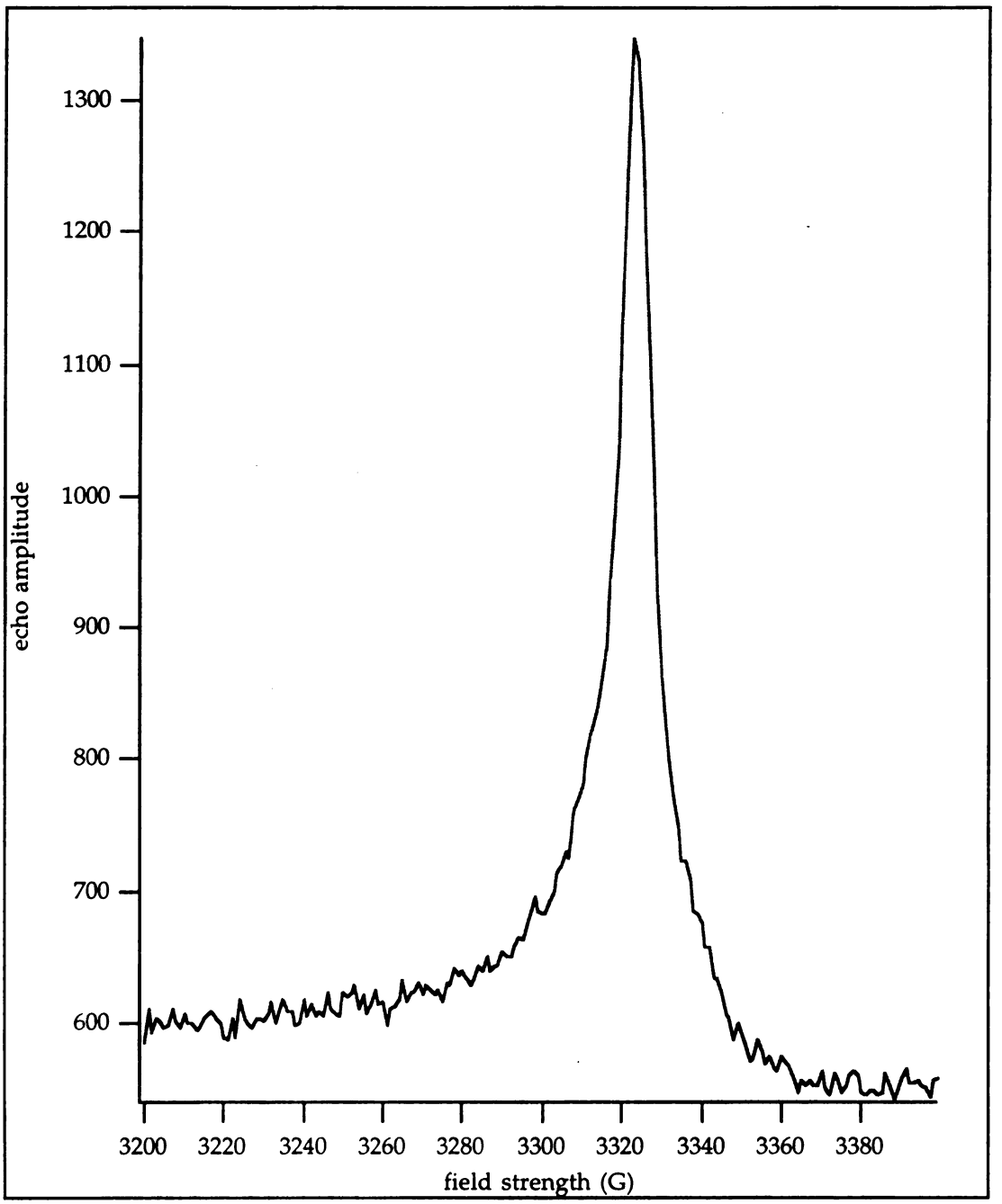

Figure 4.12: ESE-detected EPR of $Li^{+}(C211)e^{-}$ spectrum collected at 9.2819 GHz; repetition rate 60 Hz; temperature 4.20 K; τ=180 ns;

spectral width relative to that obtained in the cw-EPR spectrum (Figure 4.12). The lineshape is slightly asymmetric with FWHM = 12 G and is ~85 G wide. There is no resolvable hyperfine interaction exhibited in this pattern, consistent with the cw-EPR data. However, since ESE-EPR is collected in the absorption mode, the flat region of the cw-EPR spectrum is not reflected in the ESE-EPR spectrum. This shows how broad the resonance actually is.

Three pulse stimulated echo ESEEM data show fairly shallow modulations, when a τ value of 220 ns is chosen (Figure 4.13a). When the τ value is changed to a value that suppresses the proton modulations, the ESEEM modulations become very weak with a modulation depth less than 6 % of the overall spin echo amplitude (Figure 4.14a). The fourier transform of each time domain trace is shown in Figures 4.13b and 4.14b. Spectrum 4.13b shows a strong proton matrix line at about 14 MHz. No other assignments can be made as no other peaks can confidently be taken out of the noise. Spectrum 4.14b shows a very weak peak at the larmor frequency of lithium, 5.6 MHz when the proton modulations have been suppressed. These data suggest that there is relatively strong coupling to the protons in the cryptand, but very little if any, to the lithium.

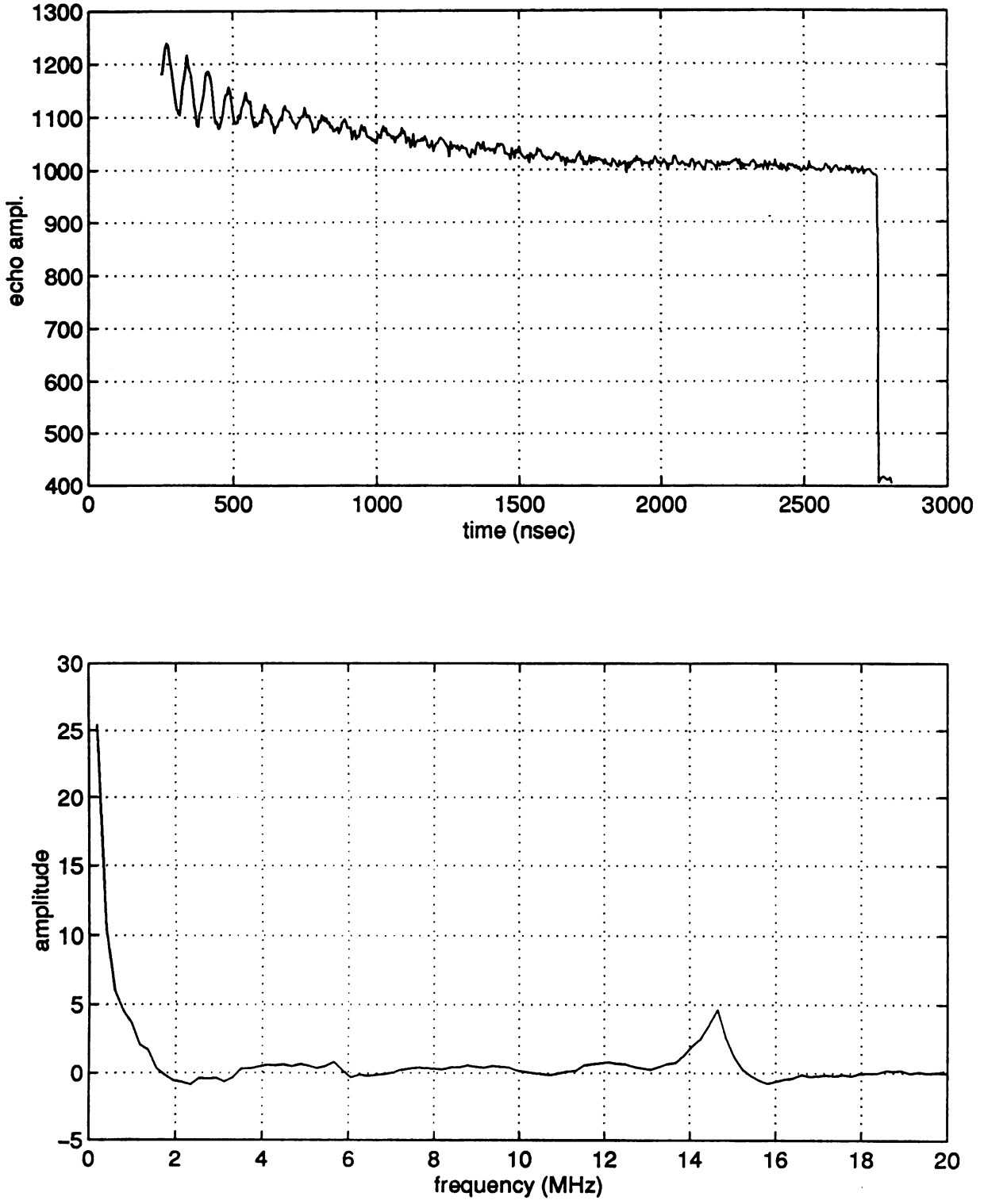

Figure 4.13: A) Time domain trace collected at 9.601 GHZ microwave frequency; 3480G field strength; τ=170 ns; T=40 ns; time inc.=10 ns; repetition rate=60Hz. B) Fourier transform spectrum of A.

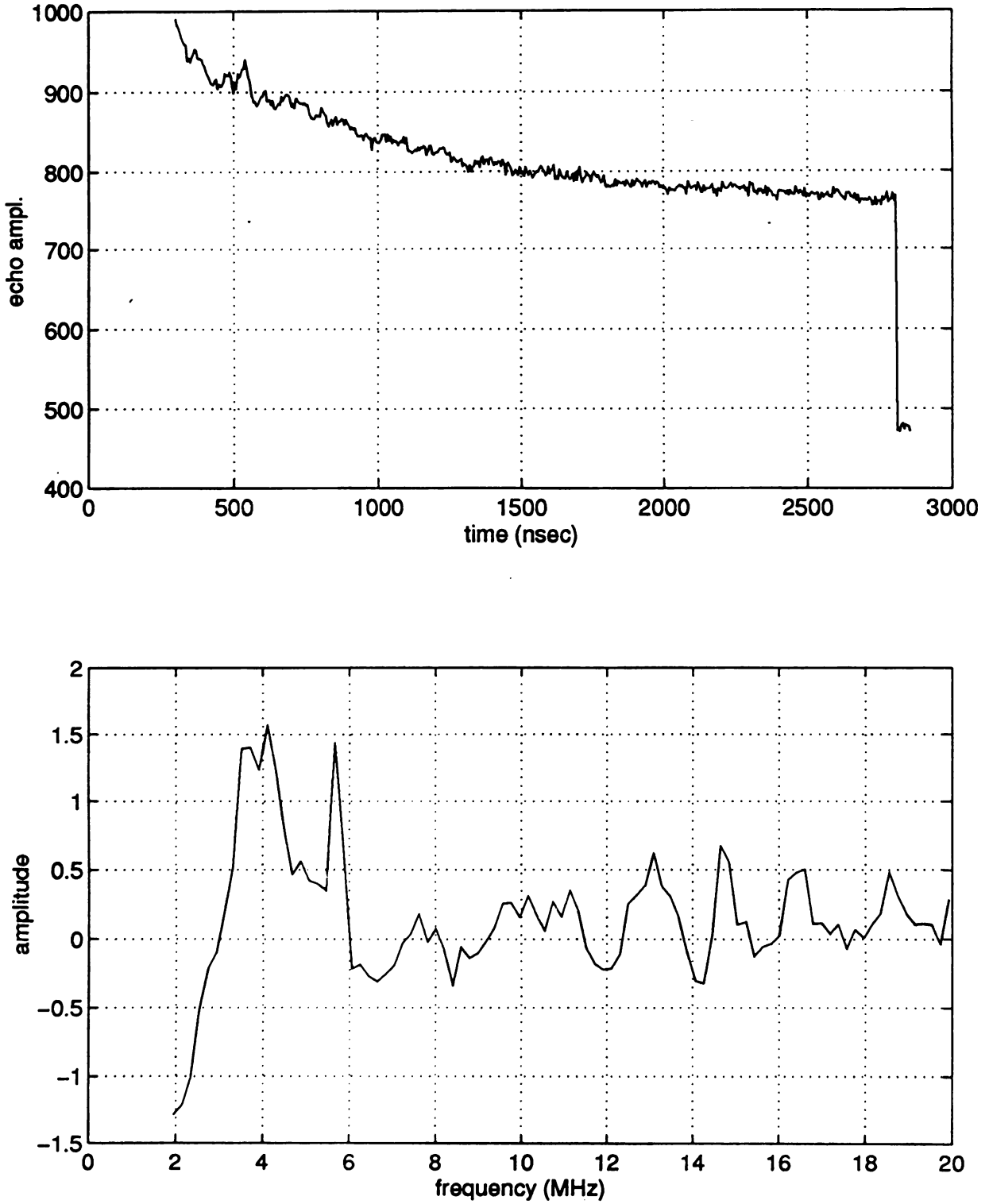

Figure 4.14: A) Time domain trace collected at 9.601 GHZ microwave frequency; 3480G field strength; τ=263 ns; T=37 ns; time inc.=10 ns; repetition rate=60Hz. B) Fourier transform spectrum of A.

Anamolous *rf*-Effect

A Bruker ESP 300E EPR spectrometer equipped with an E-360 DS ENDOR unit and an ENI model 3200L *rf* amplifier was used to collect the double resonance data. While trying to obtain ENDOR data, we quickly realized that the large signals the instrument was recording were not "normal" ENDOR spectra. It is useful to look at the energy level diagram for a system with S=1/2 and I=1/2 (Figure 4.15). The spin hamiltonian is the same as in EPR for such a system,

$$H/\hbar = \omega_o \hat{S}_z - \omega_I I_z + a\hat{S}_z \hat{I}_z \qquad (4.7)$$

where $\omega_o = g\beta H_o/\hbar$ and $\omega_I = \gamma H_o/\hbar$ and it is assumed that g and a are isotropic scalars. The selectron rules have changed in the ENDOR experiment, such that $\Delta m_s = 0$ and $\Delta m_I = 1$. In the experiment, an EPR transition is first irradiated resulting in a perturbation of the thermal Boltzmann distribution. The population difference as a consequence, becomes smaller and the transition is said to be *saturated.* At this point, a second *rf* field is applied coincidently resonant with the nuclear transitions. As a result of relaxation effects, the EPR resonance is desaturated with an increase in the EPR signal intensity. This change in EPR signal intensity is what is detected in the ENDOR experiment.

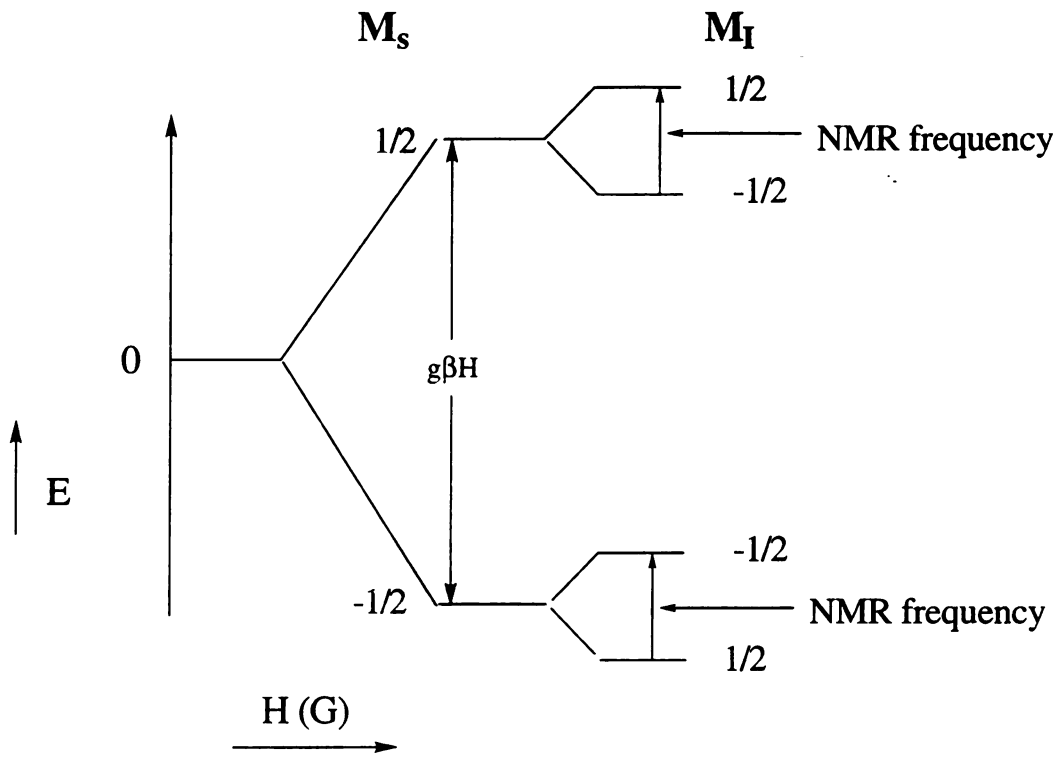

Selection Rules:

$\Delta M_I = \pm 1$
$\Delta M_s = 0$

Figure 4.15: Energy level diagram describing the effect of nuclear hyperfine interactions.

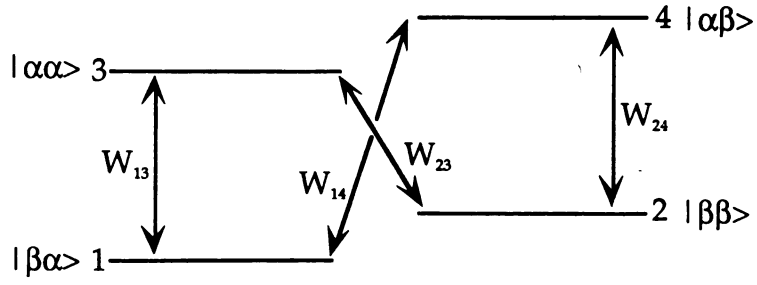

Figure 4.16: Relaxation pathways in a typical ENDOR experiment.

lines of the order <1 G are not usually good candidates for ENDOR spectroscopy due to the relaxation properties (Figure 4.16). Given the EPR linewidths of this electride, it is not expected that an ENDOR resonance would be observed.

Microwave power saturation studies were performed on this electride and revealed near saturation at power levels of 25 mW at both 25 K and 55 K (Figure 4.17). The initial ENDOR studies were collected at the 'knee" in the saturation curve. The maximum resolution in the EPR spectra were found at 25 K, thus initial ENDOR experiments were carried out at this temperature. When a static field was chosen at the maximum absorption in the EPR spectrum and sweeping the proton larmor frequency range, the spectrum did not reveal a typical ENDOR powder pattern, in fact no resonance was observed. However, in the frequency limits of 1-10 MHz, a very large *rf* absorption was observed that could not

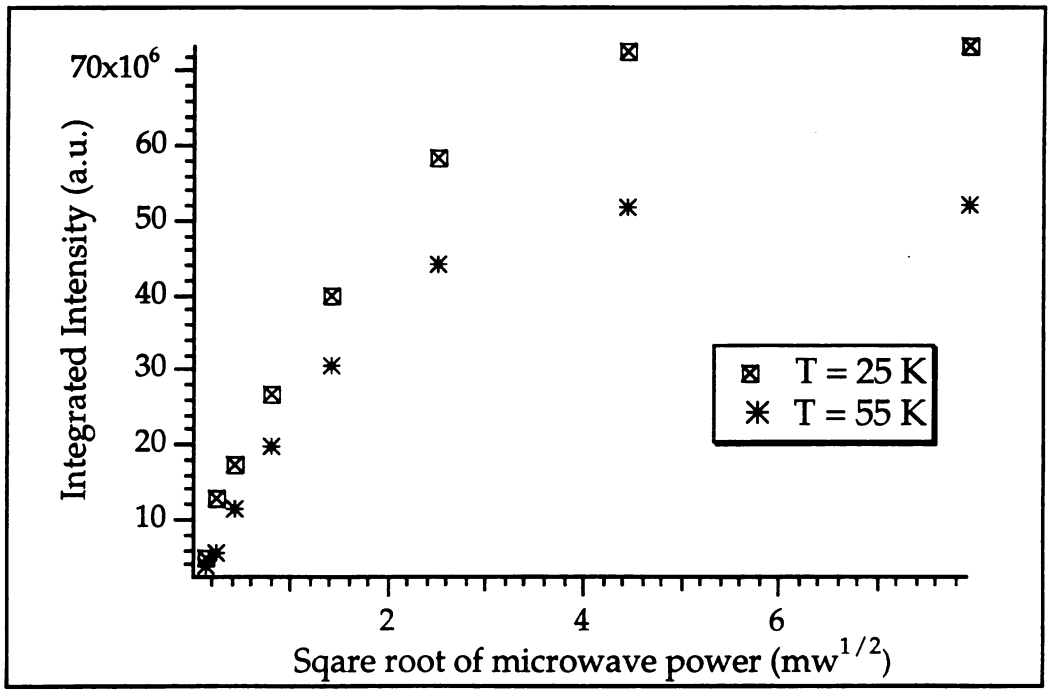

Figure 4.17: Microwave saturation study. The square root of the microwave power used is plotted as a function of the integrated intensity of the EPR line. The "knee" in the curve indicates near saturation.

be stabilized at power levels above 70W. As little as 5W of *rf* power was needed to detect the absorption. A significant portion of the absorption was below the detectable limits of the *rf* source of 1 MHz. For laboratory fields near the low field edge of the EPR resonance, a strong powder pattern lineshape that resembled the EPR resonance is detected. Progressive steps of the static magnetic field away from the EPR signal on either side resulted in an *rf* absorption that reproduced the EPR lineshape and was centered at an *rf* frequency that corresponded to the offset of the

static field from the EPR resonance. As the static field position is moved further downfield, the peak position of the 'ENDOR' resonance is shifted to a higher frequency (Figure 4.18). After a certain point off resonance, the *rf* is not broadcast effectively, resulting in a depletion of the electromagnetic radiation in the cavity. This results in a weakening of the resonance, and eventually, its disappearance. When a static field position on the high field side of the EPR resonance is chosen, an inverted resonance is observed with the same tracking characteristics as previously noted (Figure 4.19). As the static field position is moved further away from the EPR resonance field, the peak position of the 'ENDOR' resonance is shifted to higher frequencies (Figure 4.20) until it becomes undetectable above 45 MHz (low field side) or above 29 MHz (high field side) This effect was also observed at 4 K and 55 K, and in all cases, the *rf* lineshapes directly corresponded to the EPR lineshapes.

The intensity of the double resonance peaks was studied as a function of the *rf* power and showed a straight line, log-log relationship (Figure 4.20) consistent with a one *rf*-photon process. Thus there are two, one-photon processes governing this phenomenon. Similar, but weaker, microwave-*rf* absorption behavior was also observed for the electrides, $Cs^+(18C6)_2e^-$ and $Cs^+(15C5)_2e^-$ and the powder of unknown structure, $Na^+(C222)e^-$ (Ichimura et al., 1996). In addition, weaker peaks were also observed at 1/2, 1/3 and 1/4 of the fundamental *rf* frequency. Such

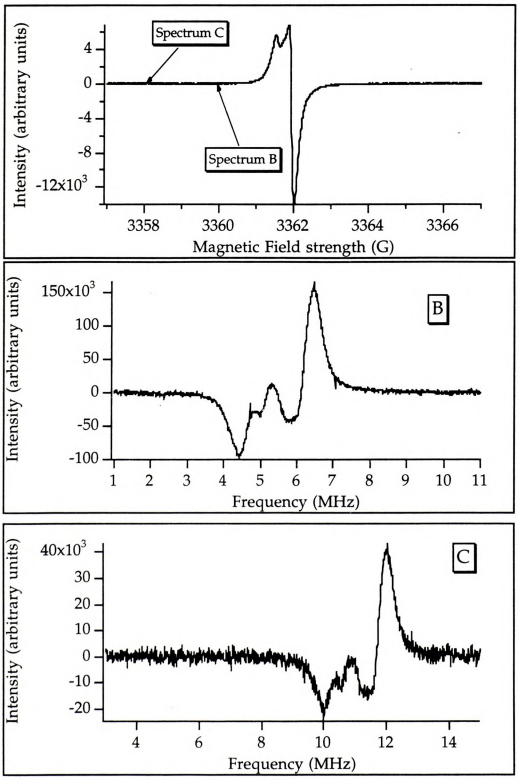

Figure 4.18: A) cw-EPR spectrum of $Li^{+}(C211)e^{-}$ collected at 25 K. 'ENDOR' spectra collected at B) 3360.0 G static field and 25 W rf power and C) 3358.0 G and 25 W rf power.

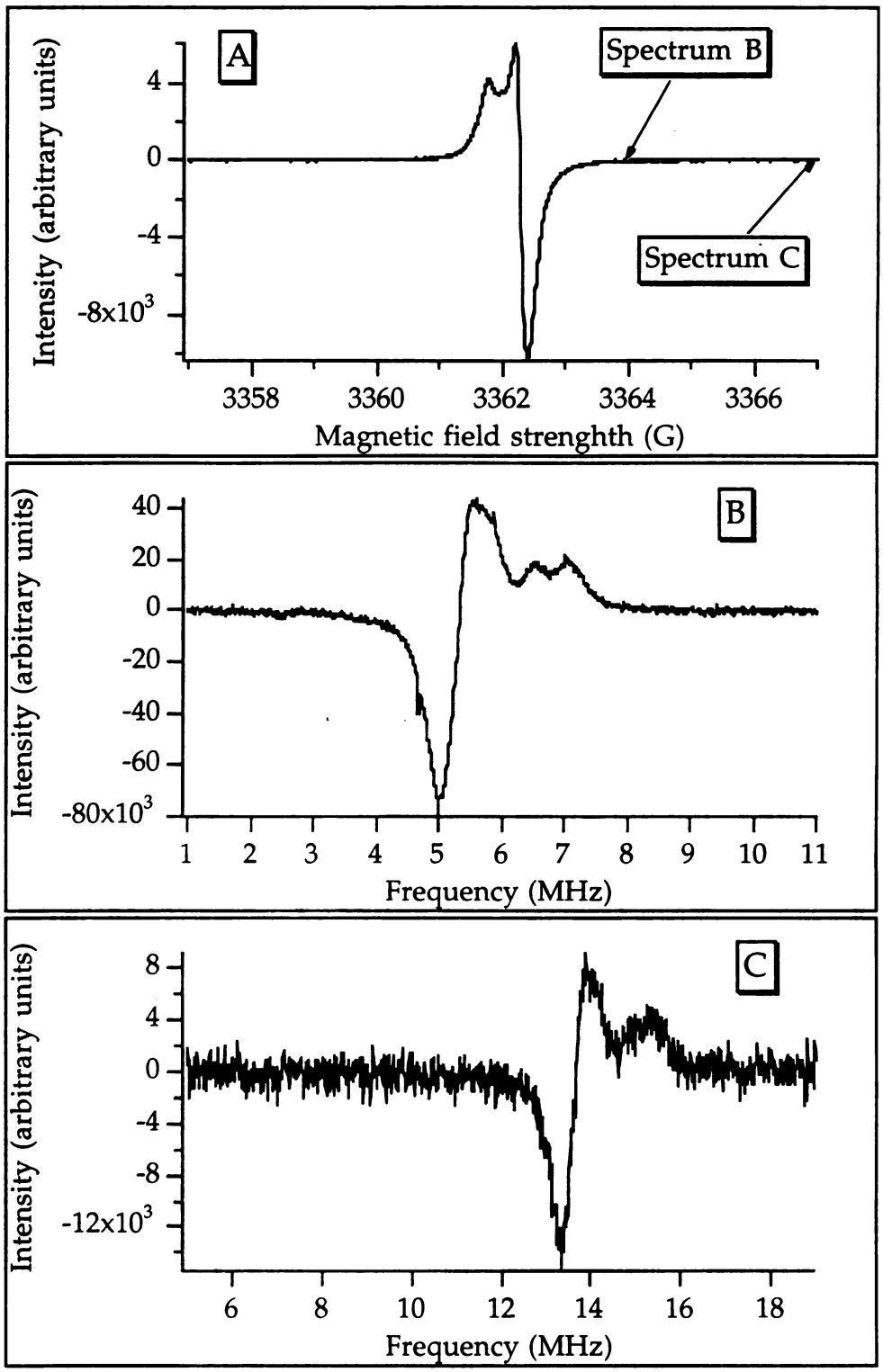

Figure 4.19: A) cw-EPR spectrum of $Li^+(C211)e^-$ collected at 25 K. 'ENDOR' spectra collected at B) 3364.0 G static field and 25 W rf power and C) 3367.0 G and 25 W rf power.

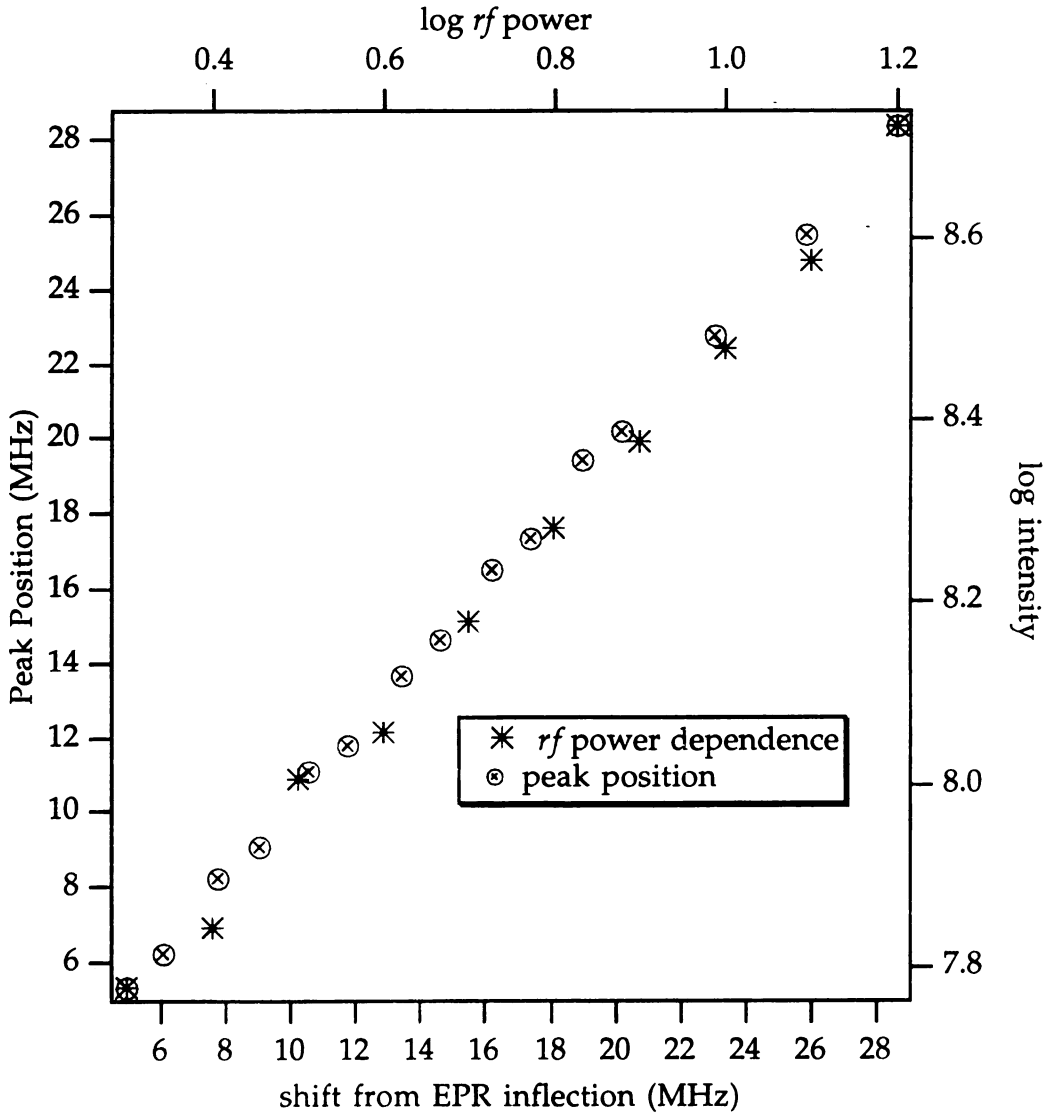

Figure 4.20: ⊗ Plot of the peak position of the 'ENDOR' effect as a function of the dc static field offset converted to MHz.
✳ The log-log relationship between the *rf* power and the integrated intensity of the 'ENDOR' line.

overtones were also observed in $Li^+(C211)e^-$, only at high *rf* power (between 200-300 W) and probably result from harmonics in the *rf* pulses. A control experiment was done with concentrated DPPH solutions, and only a proton matrix line was observed.

ENDOR-Induced EPR (EIE)

In organic free radicals, different radical species may be formed in solution at the same time. The EPR spectrum of such systems, particularly when the *g*-values are close, often consist of a superposition of spectra that can be difficult to analyze. Since there are fewer lines in an ENDOR spectrum than an EPR spectrum, the ENDOR will probably exhibit nonoverlapping signals corresponding to the individual species. Therefore, the individual EPR resonances can be recorded when a frequency position is chosen in the ENDOR, and the external magnetic field is swept. This technique, reported first by Hyde (Hyde, 1965), serves to separate two overlapping resonances. The EIE experiments were attempted with $Li^+(C211)e^-$ and the results are shown in Figure 4.21. The start frequencies (initial frequency position of the ENDOR resonance) ranged from 1 MHz to 25 MHz. Two peaks appeared with a separation that was directly related to the change in the start frequency (Figure 4.22). The peaks were weaker as the start frequency was moved further from the ENDOR resonance, until eventually, no EIE was observed at all.

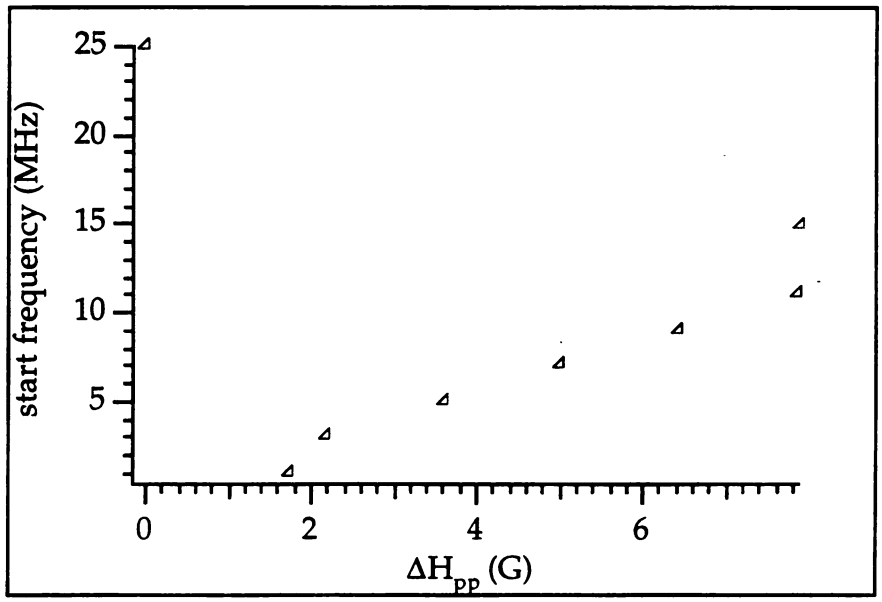

Figure 4.21: Start frequency as a function of the separation between the peaks of the ENDOR-induced EPR.

Analysis of the Magnetic Data

As described above, the packing of the complexed cations in $Li^+(C211)e^-$ results in cavities that are connected by rather open channels in a zig-zag fashion. Careful inspection of the zig-zag configuration reveals that each cavity is actually nearly equidistant to its two second nearest neighbors along the chain with connecting channels that are only about half as wide. Therefore, one expects J_1 (the major magnetic coupling constant) to result from nearest-neighbors in the zig-zag chains, with a smaller, yet significant coupling constant (J_2) from second nearest-neighbor interactions (Figure 4.23). The distance between cavities

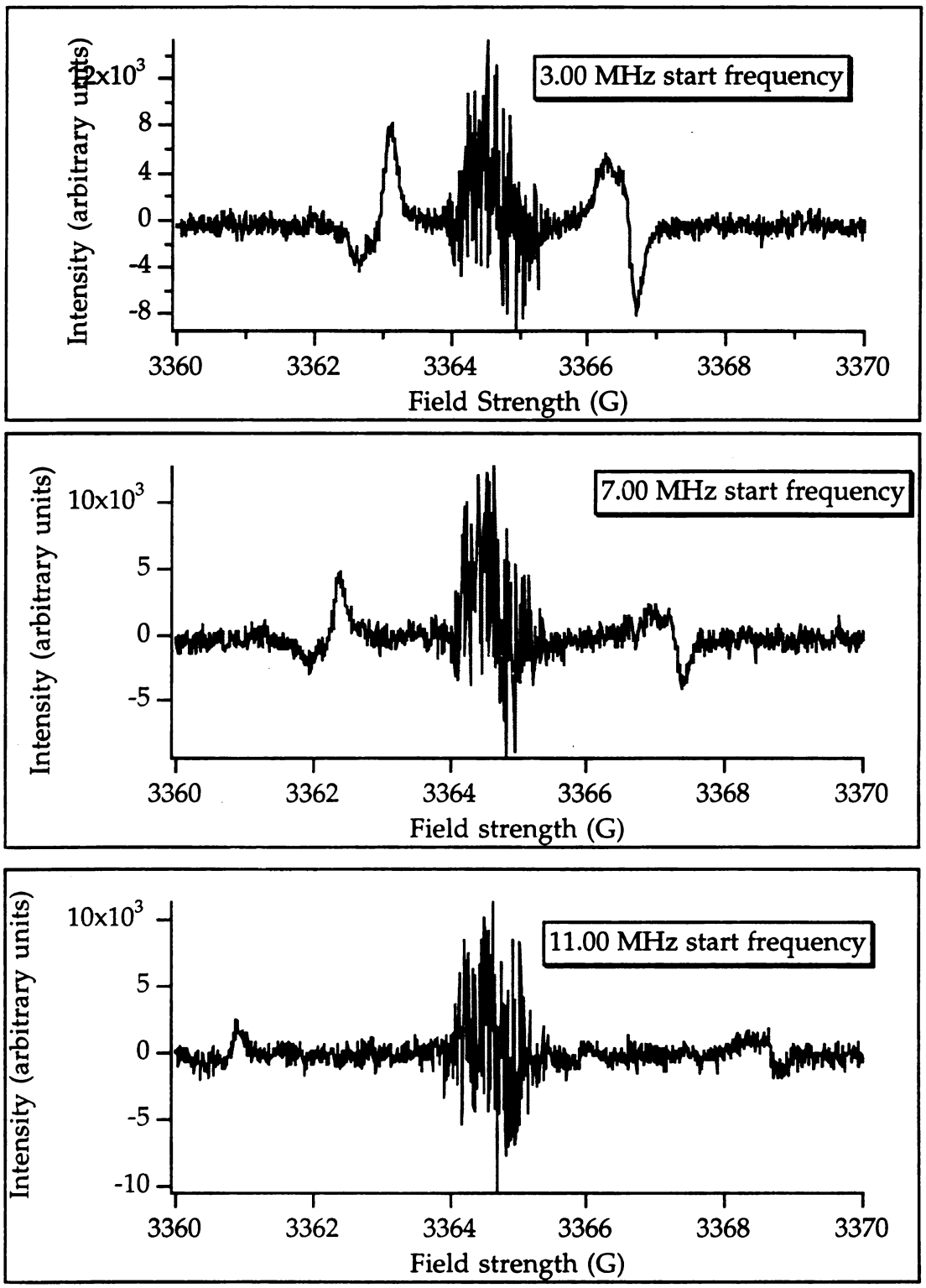

Figure 4.22: ENDOR-induced EPR spectra of $Li^+(C211)e^-$. The start frequency represents the frequency position of the ENDOR scan at which to sweep the magnetic field.

in neighboring chains is only 4% larger than that of the nearest-neighbors within each chain which suggests that no significant inter-chain channels are expected to exist. One can then speculate that the adjacent chains are probably nearly magnetically independent of one another. A dilemma arises if both interactions are AF. If the nearest neighbor interactions align the spins anti-parallel to one another, this sets up a competition because now the nearest neighbor interactions are opposed by the second nearest neighbor interactions. We are unaware of any analytical solution for the magnetic susceptibility of such a system. Numerical solutions have been obtained for finite chain lengths, (Büchner *et al.*, 1996, Castilla *et al.*, 1995, Riera & Dobry, 1995, Riera & Koval, 1996). Moreover, extrapolations to infinite length from exact numerical calculations on finite chains fail to converge, (Anathakrishna *et al.*, 1976). In addition, second nearest neighbor magnetic interactions can be complicated . When both interactions are antiferromagnetic and thus "compete", they tend to display a wide range of magnetic phase behavior (Anathakrishna *et al.*, 1976, Bonner, 1985, Büchner *et al.*, 1996, Castilla *et al.*, 1995, Chubukov, 1990, Haldane, 1982a, Hatfield, 1981, Riera & Dobry, 1995, Riera & Koval, 1996). However, not many materials with structures that suggest such interactions have been found (Brown *et al.*, 1979, Chiari *et al.*, 1990, Chiari *et al.*, 1993, Hase *et al.*, 1993). It seems that the coupling between the electrons occurs through the channels, thus distance is not the only

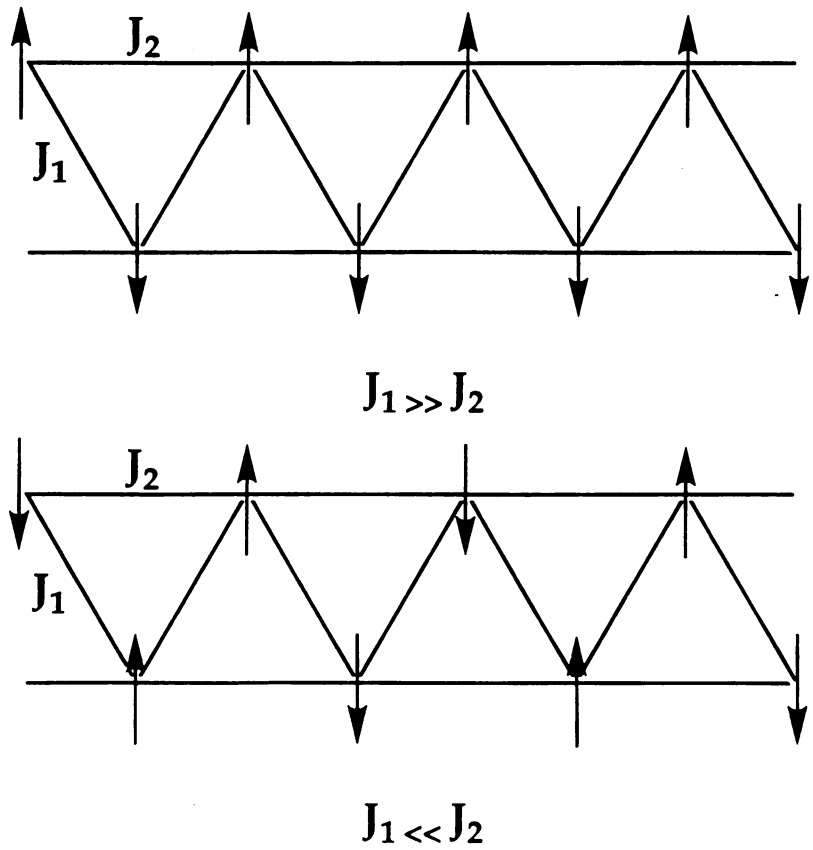

FIGURE 4.23: Illustration showing the possible spin interactions in the zig-zag chains of Li+(C211)e-.

determining factor (Dye, 1993, Dye *et al.*, 1996). Thus, it is reasonable to assume rather strong 1D antiferromagnetic coupling between electrons in adjacent cavities along the chain, weaker coupling between next-nearest neighbors along the chain, and inter-chain coupling can be considered negligible. Coronado described a similar behavior as a 1D "ladder-like" systems where the chain was a "spin frustrated double chain" (Coronado *et al.*, 1993).

Keeping in mind the 1D character, consider the bulk and spin susceptibility data. The magnetic susceptibility has linear chain Heisenberg antiferromagnetic (LCHA) behavior with spin-pairing beginning at 14 K that is complete as T approaches zero. The EPR results also suggest a spin pairing mechanism with a maximum in the spin susceptibility of 57 K in the crystalline sample and 20 K in the 'powder' sample. These data are in good agreement with the bulk susceptibility obtained from the SQUID measurements.

LCHA with S = 1, have recently been the focus of many studies. Inelastic neutron scattering (Renard *et al.*, 1987, Rossat-Mignod *et al.*, 1990) magnetic resonance spectroscopy (Brunel *et al.*, 1992, Date & Kindo, 1990, Date & Kindo, 1992, Kindo *et al.*, 1992) and susceptibility measurements (Katsumata *et al.*, 1989) have been used to verify the presence of an energy gap above the ground state, as Haldane conjectured in 1983 (Haldane, 1983), with much subsequent theoretical support. Haldane also concluded that one-dimensional LCHAs with S = 1 and S = 1/2 (Haldane, 1982b) are qualitatively different, with half integer spins leading to a gapless spectrum. This initially controversial proposal has been solidly supported by a solvable model (Affleck, 1989) numeric studies (Sakai & Minoru, 1990) and experimental evidence (Renard *et al.*, 1987). Haldane argued that spontaneous dimerization would occur in S = 1/2 systems with competing nearest-neighbor (J_1) and next-nearest

neighbor (J_2) interactions for $J_2/J_1 \geq 1/6$. Dimerization can also result as the temperature is reduced as a result of spin-orbit interactions in antiferromagnetically coupled chains. As mentioned previously in this chapter, structural distortions occur to accommodate a spin-Peierls dimerization (Fukuyama, 1987). This dimerized state, which also leads to zero susceptibility at 0 K, can be distinguished from Haldane dimerization, as the latter does not require lattice distortion. A number of S = 1 LCHAs show excitations which are *spin wave*-like in nature and EPR has been used as a direct way to probe the spin states of spin wave modes (Affleck, 1992, Brunel *et al.*, 1992). Both ferromagnetic and anti-ferromagnetic systems can give spin waves (Figure 4.24). A spin flip occurs, and the energy of the flipped spin can be distributed to the whole system of spins. The spin waves at the surface cannot move; they are said to be "pinned".

The anomalous radio frequency-microwave spectroscopy described above and the known structure of the electrides suggest anti-ferromagnetic spin waves. At the very least, this study shows that these electrides have a dense manifold of energy states in the presence of a magnetic field. The most striking feature of these results is the narrow conventional EPR spectrum and yet the ability to excite transitions well below and above the resonance field with *rf* frequencies that precisely match the field offset. This implies the presence of selection rules for the EPR transition that

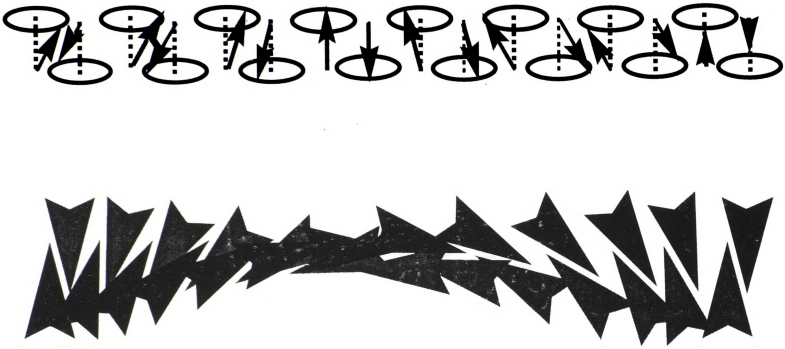

Figure 4.24: Antiferromagnetic *spin waves* on a line of spins. The spins viewed in perspective (top view) and shown from above (bottom view). The tips of the spin vectors show one wavelength. The vectors precess on surface cones, progresively tilting by a constant tilt angle (in this case, 15°).

prohibit arbitrary transitions between energy levels. It also demands a very high density of states as a result of inter-electron coupling such that strong double resonance absorptions can occur at arbitrary fields (within limits). Furthermore, this effect was observed with very low microwave powers (as low as 40 dB) which indicats that saturation is not a necessary requirement. In essence, two types of electromagnetic radiation are coupled together to induce this two-photon effect.

The most likely source of a high density of energy levels in these electrides is the formation of 1D spin-waves. If the "Curie-tail" in the susceptibility of $Li^+(C211)e^-$ is due to the presence of odd chains, we infer from the ~1% contribution, that the average chain length is ~ 50. This, together with a distribution of chain lengths would insure a high density of spin-wave levels. A possible energy level diagram to describe the *rf*-microwave effect is shown in Figure 4.25.

The notion that spin waves in ferromagnetic materials could be affected by a uniform *rf* field, was discussed by Kittel (Kittel, 1958), and in anti-ferromagnetic materials, by Orbach and Pincus (Orbach & Pincus, 1959). For this to transpire, the surface spins must experience local anisotropy that is different from the interior spins. This anisotropy serves to 'pin' the surface spins and quantize spin wave modes perpendicular to the direction of the applied magnetic field. Because the antiferromagnetically coupled electrons in electrides form chains of

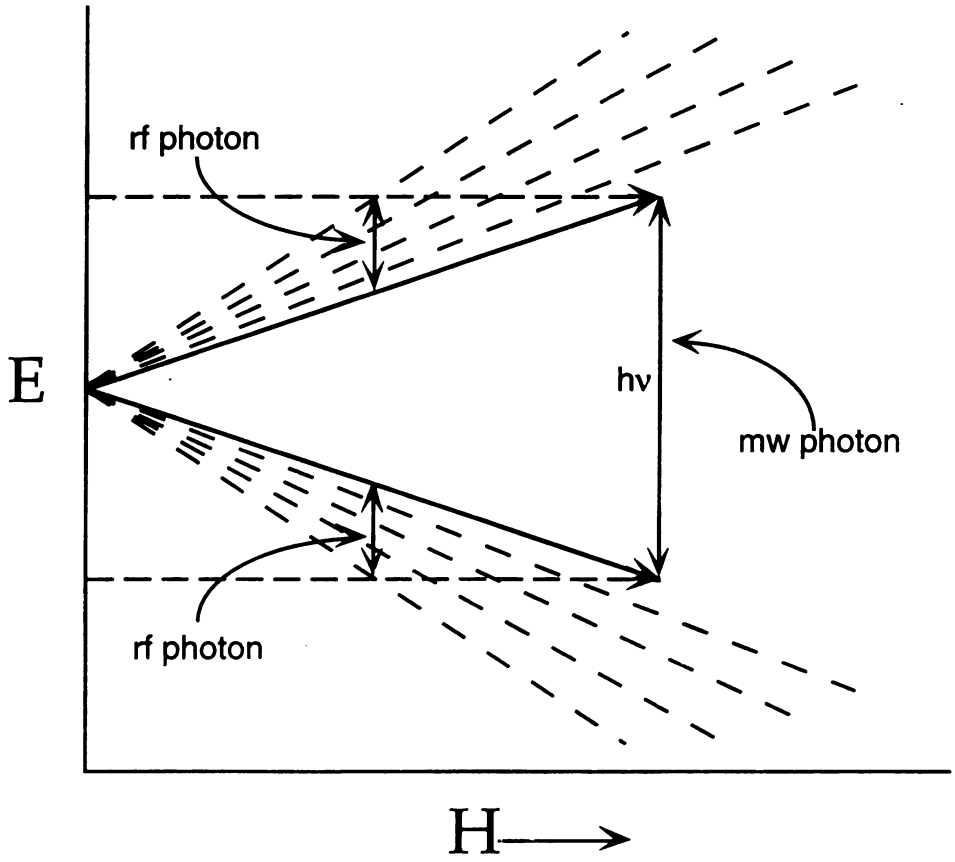

Figure 4.25: Possible energy level diagram describing the anamolous *rf* effect. At resonance, a photon, hν, matches the energy level separation. At lower (and higher) field positions, the rf photon may couple to the microwave photon to allow the transition.

considerable length, these spin wave states are band-like in nature and apparently coupled to the α and β electron spin states. Their presence could be masked in the conventional EPR spectrum by exchange narrowing of the resonance lineshape. The low *rf* power necessary to drive these transitions and the magnetic field dependence of the transition frequency indicate that the transitions being probed concern the magnetic moment of the unpaired electron spin. To our knowledge, this report is the first of its kind, where antiferromagnetic spin waves were excited by using a uniform *rf* field. Mattis theorized the type of behavior reported here for 1D LCHA systems (Mattis, 1965). Studies underway include 'ENDOR' measurements on single crystals of $Li^+(C211)e^-$ to confirm the theory regarding the origin of the *rf* absorptions. We are also modifying the ENDOR coils so that the *rf* intensity can be measured accurately across a variety of frequencies.

Discussion

The electride, $Li^+(C211)e^-$ has been characterized as a 1D LCHA. We now find that they show very strong *rf* -microwave two-photon absorptions consistent with the presence of rather long chain length spin-waves. To our knowledge, this is the first observation of this kind for an S = 1/2 LCHA.

By using the channel and cavity diagrams, one can relate qualitatively, the magnetic properties of the electride to the width, length and shape of their anionic cavities and the channels that interconnect them (Dye *et al.*, 1996, Wagner, 1994). It is not astonishing to expect the wave function's excess electrons to extend into the void space between the cavities in order to minimize kinetic energy. This was illustrated theoretically for $Cs^+(15C5)_2e^-$ (Singh *et al.*, 1993). Currently, there is no quantitative relationship between the extent of overlap of the wavefunctions of neighboring electrons, and the width, length and shape of the channels.

Conclusions

Although the SQUID and EPR measurements suggest evidence of gradual spin dimerization, the driving force for this dimerization is not fully understood. It may be due to a spin-Peierls transition caused by elastic distortions in the lattice or possibly by competing AF intra-chain interactions which can contribute to electronically-driven spin dimerization, as Haldane predicted (Haldane, 1982b).

The spin-Peierls and Haldane dimerizations are both characterized by a non-magnetic singlet ground state with a finite energy gap. However, the origin of the two states is quite different. It was noted recently that small impurities in both Haldane and spin-Peierls materials can have a

remarkable effect on susceptibility measurements (Ajiro, 1995). High field magnetization and temperature dependence of the susceptibility revealed that when the Haldane system, $NiC_2O_4 \cdot 2DMIZ$ (dimethyl imidazole), was doped with up to 20% of a nonmagnetic impurity, the Haldane state survives. However, when $CuGeO_3$, a spin Peierls system, was doped with only 4% impurity, the spin-Peierls state almost disappeared (Ajiro, 1995). This suggests that the origin of the $Li^+(C211)e^-$ dimerization could be determined if doping studies were undertaken.

The negative species in electrides that balances the cationic charges on complexed alkali cations are nearly-free electrons (Dye, 1990, Dye, 1993, Dye & Huang, 1990, Dye *et al.*, 1996). They are trapped in large cavities and interact with one another through open connecting channels (Dye *et al.*, 1996). The geometry, length and diameter of these channels correlate well with the effective magnetic dimensionality and coupling constant. The susceptibility data and fits to Equation 4.7 shown in Figure 4.6 and the spin susceptibilities from EPR intensities (Figure 4.11) show that spin-pairing becomes pronounced below about 10 K and that the susceptibility goes smoothly to zero at 0 K upon removal of a small Curie tail contribution. The fit of the data by the 1 D Heisenberg model with a single value of J is excellent above 14 K for both types of sample. The low temperature drop in the susceptibility is qualitatively like that of a spin-Peierls transition, which is a manifestation of the intrinsic instability of a

1D Heisenberg chain toward dimerization. However, competition between nearest-neighbor and next nearest neighbor interactions may also contribute to the dimerization. The "frustration" could be relieved by redistribution of the electron density within the cavity channel framework to yield stronger pairwise interactions through the major channels, which would decrease the interaction with next nearest-neighbor trapped electrons.

The fact that two phases exist is not unprecented (Dawes *et al.*, 1991, Wagner *et al.*, 1993). The *rf* effect was extremely weak when the powder sample was tested. The signal probably originated from a very minor contribution of crystalline material and this change in packing can drastically affects the electron-electron coupling (Dye, 1993). The powdered samples of $Li^+(C211)e^-$ grow in such a way as to decrease the effective value of $-J_1/k_B$ from 50 K to 18 K, probably by altering the size of the inter-connecting channels. The differences between the two phases is also reflected by differences in the ^7Li NMR chemical shifts. The reason why spin dimerization occurs at the same temperature for both phases is puzzling.

BIBLIOGRAPHY

Affleck, I. (1989) *Journal of PhysicsCondensed Matter 1*, **Quantum Spin Chains and the Haldane Gap.**, 3047-3072.

Affleck, I. (1992) *Physical Review B 46*, **Theory of Electron Spin Resonance in Haldane-gap Antiferromagnets**, 9002-9008.

Ajiro, Y. (1995) *Physical Review 51*, **Remarkable Difference in the Effects of Nonmagnetic Impurities on the Haldane and spin-Peierls Systems**, 9399.

Anathakrishna, G., Weiss, L. F., Foyt, D. C., & Klein, D. J. (1976) *Physica 81B*, **Properties of the Linear Heisenberg Chain with Nearest and Next-Nearest Neighbor Interactions**, 275-284.

Bonner, J. C. (1985) in ***Magneto-Structural Correlations in Exchange Coupled Systems*** (R. D. Willett, D. G., and O. Kahn, Ed.) pp 157, D. Reidel Publishing Company, Dordrecht, Holland.

Bray, J. W., Interrante, L. V., Jacobs, I. S., & Bonner, J. C. (1983) in ***Extended Linear Chain Compounds*** (Miller, J. S., Ed.) pp 353-415, Plenum Press, New York.

Brown, D. B., Donner, J. A., Hall, J. W., Wilson, S. R., Wilson, R. B., Hodgson, D. J., & Hatfield, W. E. (1979) *Inorganic Chemistry 18*, **Interaction of Hydrazine with Copper(II) Chloride in Acidic Solutions. Formation, Spectral Properties, and Structures of Copper(II), Copper(I) and Mixed-Valence Species**, 2635-2641.

Brunel, L. C., Brill, T. M., Zaliznyak, I., Boucher, J. P., & Renard, J. P. (1992) *Physical Review Letters 69*, **Magnon Spin Resonance in the Haldane Spin Chains of $Ni(C_2H_8N_2)NO_2ClO_4$**, 1699-1702.

Büchner, B., Ammerahl, U., Lorenz, T., Brenig, W., Dhalenne, G., & Revcolevschi, A. (1996) *Physical Review Letters 77*, **Magnetic Frustration Induced Formation of the Spin-Peierls Phase in $CuGeO_3$: Experimental Evidence**, 1624-1627.

Castilla, G., Chakravarty, S., & Emery, V. J. (1995) *Physical Review Letters 75*, **Quantum Magnetism of $CuGeO_3$**, 1823-1826.

Chiari, B., Piovesana, O., Tarantelli, T., & Zanazzi, P. F. (1990) *Inorganic Chemistry 29*, **Exchange Interactions in a Novel Copper(II) Linear Chain Compound with Ladderlike Structure: Cu_2(1,4-diazacycloheptane)$_2Cl_4$**, 1172-1176.

Chiari, B., Piovesana, O., Tarantelli, T., & Zanazzi, P. F. (1993) *Inorganic Chemistry 32*, **Further Neighbor Magnetic Exchange Interaction in a Novel Pseudolinear Tetramer of Copper(II)**, 4834-4838.

Chubukov, A. V. (1990) *J. Phys. Condens. Matter* 2, **Unusual States in the Heisenberg Model with Competing Interactions**, 4455-4470.

Coronado, E., Drillon, M., & Georges, R. (1993) in *Research Frontiers in Magnetochemistry* (O'Connor, C. J., Ed.) pp 27-66, World Scientific, Singapore.

Date, M., & Kindo, K. (1990) *Physical Review Letters 65*, **Elementary Excitations in the Haldane State**, 1659-1662.

Date, M., & Kindo, K. (1992) *Journal of Magnetism and Magnetic Material 104-10*, 7811-812.

Dawes, S. B., Eglin, J. L., Moeggenborg, K. J., Kim, J., & Dye, J. L. (1991) *Journal of the American Chemical Society 113*, **Cs^+(15-crown-5)$_2e^-$, A Crystalline Antiferromagnetic Electride**, 1605-1609.

de Jongh, L. J. (1988) .

Dye, J. L. (1990) *Science 247*, **Electrides: Ionic Salts with Electrons as the Anions**, 663-668.

Dye, J. L. (1993) *Nature 365*, **Anionic Electrons in Electrides**, 10-11.

Dye, J. L., & Huang, R. H. (1990) *Chemistry in Britain 26*, **Electride Structures and Properties**, 239-244.

Dye, J. L., Wagner, M. J., Overney, G., Huang, R. H., Nagy, T. F., & Tomanek, D. (1996) *Journal of the American Chemical Society 118*, **Cavities and Channels in Electrides**, 7329-7336.

Estes, W. E., Gavel, D. P., Hatfield, W. E., & Hodgson, D. (1978) *Inorganic Chemistry 17*, **Magnetic and Structural Characterization of Dibromo- and Dichlorobis (Thiazole) Copper(II)**, 1415-1421.

Fukuyama, H. (1987) *Synthetic Metals 19*, **Thoery of Spin-Peierls Transition**, 63-68.

Haldane, F. D. M. (1982a) *Phys. Rev. B 25*, **Spontaneous Dimerization in the S=1/2 Heisenberg Antiferromagnetic Chain with Competing Interactions**, 4925-4928.

Haldane, F. D. M. (1982b) *Physical Review B 25*, **Spontaneous Dimerization in the S=1/2 Heisenberg Antiferromagnetic Chain with Competing Interactions.**, 4925-4928.

Haldane, F. D. M. (1983) *Physical Review Letters 50*, **Nonlinear Field Theory of Large-Spin Antiferromagnetets: Semiclassically Quantized Solitons of the One-Dimensional Easy-Axis Neél State.**, 1153-1156.

Hase, M., Terasaki, I., & Uchinokura, K. (1993) *Physical Review Letters 70*, 3651.

Hatfield, W. E. (1981) *J. Appl. Phys. 52*, **New Magnetic and Structural Results for Uniformly Spaced, Alternatingly Spaced, and Ladder-Like Copper(II) Linear Chain Compounds**, 1985-1990.

Huang, R. H., Wagner, M. J., Gilbert, D. J., Reidy-Cedergren, K., Ward, D. L., Faber, M. K., & Dye, J. L. (1996) *Submitted for Publication*, **Synthesis, Structure and Properties of the "Spin-Ladder-Like" Electride, Li^+(Cryptand[2.1.1])e^-.**

Hyde, J. S. (1965) *The Journal of Chemical Physics 43*, **ENDOR of Free Radicals in Solution**, 1806-1818.

Ichimura, A. S., Dye, J. L., & McCracken, J. L. (1996) *unpublished results.*

Ising, E. Z. (1925) *Physik 31*, 253.

Jakubovics, J. P. (1987) **Magnetism and Magnetic Materials.**, Vol. , The Institute of Metals, London.

Katsumata, K., Hori, H., Takeuchi, T., Date, M., Yamagishi, A., & Renard, J. P. (1989) *Physical Review Letters 63*, **Magnetization Process of an S=1 Linear Chain Heisenberg Antiferromagnet.**, 86-88.

Kindo, K., Takeuchi, T., Yosida, T., & Date, M. (1992) *Physica B 177*, **High Magnetic Field EPR in Haldane Materials.**, 381-385.

Kittel, C. (1958) *Physical Review 110*, **Excitation of Spin Waves in a Ferromagnet by a Uniform rf Field**, 1295-1297.

Landers, J. S., Dye, J. L., Stacy, A., & Sienko, M. J. (1981) *Journal of Physical Chemistry 85*, **Temperature-Dependent Electron Spin Interactions in Lithium[2.1.1] Cryptate Electride Powders and Films**, 1096-1099.

Mattis, D. C. (1965) **The Theory of Magnetism**, Vol. , Harper and Row, New York.

O'Reilly, D. E. (1964) *Journal of Chemical Physics 41*, **Knight Shifts and Relaxation Times of Alkali Metal and Nitrogen Nuclei in Metal-Ammonia Solutions**, 3729-3735.

Orbach, R., & Pincus, P. (1959) *Physical Review 113*, **Excitation of Spin Waves in an Antiferromagnet by a Uniform rf Field.**, 1213-1215.

Renard, J. P., Verdageur, M., Regnault, L. P., Erkelens, W. A. C., Rossat-Mignod, J., & Stirling, W. G. (1987) *Europhysics Letters 3*, **Presumption for a Quantum Energy Gap in the Quasi-One-Dimensional S=1 Heisneberg Antiferromagnetic Ni(C2H8N2)2NO2(ClO4).**, 945-951.

Riera, J., & Dobry, A. (1995) *Physical Review B 51*, **Magnetic Susceptibility in the Spin-Peierls System $CuGeO_3$**, 16098-16102.

Riera, J., & Koval, S. (1996) *Physical Review B 53*, **Magnetic Excitations and Effects of Magnetic Fields on the Spin-Peierls Transition in $CuGeO_3$**, 770-774.

Rossat-Mignod, J., Burlet, P., Regnault, L. P., & Vettier, C. (1990) *Journal of Magnetism and Magnetic Material 90-91*, **Neutron Scattering and Magnetic Phase Transitions.**, 5-16.

Sakai, T., & Minoru, T. (1990) *Physical Review B 42*, **Effect of the Haldane Gap on Quasi-One-Dimensional Systems.**, 4537-4543.

Singh, D. J., Krakauer, H., Haas, C., & Pickett, W. E. (1993) *Nature (London) 365*, **Theoretical Determination that Electrons Act as Anions in the Electride $Cs^+(15\text{-crown-}5)_2e^-$**, 39-42.

Wagner, M. J., **Electrical and Magnetic Properties 0f Alkalides, Electrides and Related Materials and their Structural and Molecular Dynamical Correlations**, 1994.

Wagner, M. J., & Dye, J. L. (1996) in ***Molecular Recognition: Receptors for Cationic Guests*** (Gokel, G. W., Ed.) pp 477-510, Pergamon Press, Ltd., Oxford, U. K.

Wagner, M. J., Huang, R. H., & Dye, J. L. (1993) *Journal of Physical Chemistry 97*, **First Crystalline Electride Revisited: New Magnetic Susceptibility Studies of $Cs^+(18\text{-crown-}6)_2e^-$**, 3982-3984.

Chapter 5

ESEEM Studies of Electron Trapping in $Cs_2^+(21C7)_2Na^-_2$: Mapping the Electron Density

Background Information

Until the year 1974, it was thought that alkali metals could only have the $^{+}1$ or 0 oxidation state in the solid phase. It is now well established that alkali metals can in addition have a $^{-}1$ oxidation state in the solid phase. The alkalide reaction is driven thermodynamically by the encapsulation of the Cs cation in this case, by a crown ether such as 21C7. When an equimolar amount of Na metal is added under anaerobic conditions, the reaction is as follows:

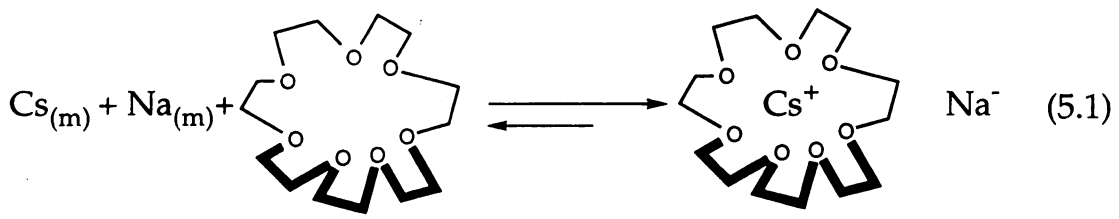

(5.1)

As was addressed earlier in Chapter 1 of this dissertation, there has been some disagreement as to whether the valence electron of the cation resides near the nucleus, or if the electron is trapped and occupies the anionic position. Evidence from our group has agreed with the latter of the two, in particular, the F-center model. However, most experiments have failed to answer this question definitively. EPR is one way in which one can probe the location of the electron density in the electride. During the synthesis of

$Cs^+(21C7)Na^-$, the alkali metals and complexants are dissolved together resulting in an equilibrium between the alkali metal anions and the solvated electrons,

$$M^- \rightleftharpoons M^+ + 2e^-_{solv} \qquad (5.2)$$

Electrons then become trapped in the alkalide crystal, as in the F-center model. The degree of "doping" in the sample depends heavily on the synthetic procedure. The defect electrons that occupy the anionic positions are present in small concentrations isolated from one another, avoiding the problem of an exchange narrowed EPR signal. The driving force behind these experiments is to obtain information regarding the nature of the trapped electrons, and to determine whether the electrons are trapped interstitially, or reside at or near the nucleus of the alkali metal.

While trying to synthesize new alkalides and eventually new electrides, the choice of complexant is of absolute importance. Ideally, tight binding of the cation in the complexant can lead to a relatively stable alkalide perhaps eventually at room temperature. $Na^+(C222)Na^-$ was the first crystallized alkalide (Tehan *et al.*, 1974) and it is stable at room temperature for a couple of days making the possibility of synthesizing room temperature stable alkalides quite promising. However, since then, there has not been such a stable alkalide or electride synthesized. The cesium cation fits very snugly between two 18C6 molecules to form either

an electride (Dawes *et al.*, 1986) sodide (Dawes *et al.*, 1989) or ceside (Huang *et al.*, 1987), depending on the respective quantities of the starting materials. The crown ether 18C6 has a hole diameter in the range of 2.6-3.2 Å while the slightly larger crown ether, 21C7, has a hole diameter of 3.4-4.3 Å (Pedersen, 1970) where two different models were used to calculate these extremes. Since the ionic diameter in a crystal of Cs^+ is 3.34 Å, (Pedersen & Frensdorff, 1972) it makes sense that it takes two 18C6 molecules to sufficiently encapsulate the cation. The cesium cation should fit better in the larger 21C7 complexant and in fact it does, but not in the conventional way.

Synthesis of $Cs^+(21C7)Na^-$

The synthesis of alkalides was already explained in great detail in chapter 2, but there are a few points worth noting for this particular alkalide. The complexants initially need to be purified and 21C7 is a very viscous complexant, therefore it requires a temperature of about 200°C under anaerobic conditions to sublime. Approximately equimolar portions of Cs and Na metals were deposited into one bulb of a two-chamber K-cell (Figure 2.2). To increase the yield and to minimize doping effects, a *slight* increase in stoichiometric amount of Cs was added to the other bulb. When doped material is desired, the stoichiometry changes such that Na is deficient. This allows the extra electron from the Cs cation

to become trapped in the anionic voids that cannot be filled by the sodide. This also increases the number of paramagnetic centers in the material. $MeNH_2$ was purified over NaK alloy, then distilled onto the complexant and reacted swiftly. When confident that nearly all of the 21C7 had dissolved, the solution was poured over to the metal mirror and was allowed to react for at least ten hours. It was found that changing this reaction time altered the yield significantly so the reaction was usually left overnight at -78°C. Freshly purified Et_2O was added to the solution as a co-solvent to make a saturated solution and the mother liquor was then poured through the frit to the chamber containing the collection fingers. Other solvent systems were attempted, e.g. Me_2O and TMA, but this combination did not allow for good crystal growth. Crystals were grown in a temperature cycling bath at -50°C initially, and slowly cooled to a temperature of -70°C over a period of about 2 days. The sharp needle-like dark red crystals that remained were then washed with fresh Et_2O, the solvent was removed completely and the crystals were collected and stored in liquid nitrogen until further use.

Structural Information

A crystal of dimensions 0.1x0.2x0.4 mm^3 was used to determine the crystal structure. A crystal system of triclinic was determined (Huang, 1994) with one molecule per unit cell, where a=10.469 Å, b=10.032 Å,

c=12.708 Å, α=90.919°, β=73.385° and γ=107.453°. The volume of the unit cell and the density of the crystal were found to be 1216.5Å and 1.267 g/cm^3, respectively. This is the first alkalide without any symmetry elements, although most of the alkalide structures are of low symmetry. Strictly speaking, the empirical formula for this compound is $Cs^+_2(21C7)_2Na^-_2$. The ORTEP diagram is shown in Figure 5.1 where the Cs1-O distances range from 3.18 to 3.55Å, and the Cs2-O distances range from 3.10 to 3.48Å. This indicates that the Cs cations are in non-symmetric positions in the crystal. The Cs1-Cs2 distance is 5.28Å and the two Cs-Na distances are 4.48 Å and 4.44Å. This implies that a contact ion pair is present, consequently, this molecule is a good candidate for EPR analysis. Each Cs cation is bonded to seven O atoms from one of the 21C7 molecules, and one O atom of the other 21C7 molecule, making the Cs cation eight coordinate and connects the two $Cs^+(21C7)Na^-$ complexes together. The O7-Cs1(2)-O116 bond angles are around 74° while the Cs1-O7(116)-Cs2 bond angles are around 105°. These atoms form a nearly symmetric parallelogram in the crystal structure. Other pertinent distances within the crystal packing include Cs-Cs, Cs-Na and Na-Na of 8.90, 7.67 and 7.18Å, respectively. Two different perspectives of the packing of this complex are shown in Figures 5.2 and 5.3.

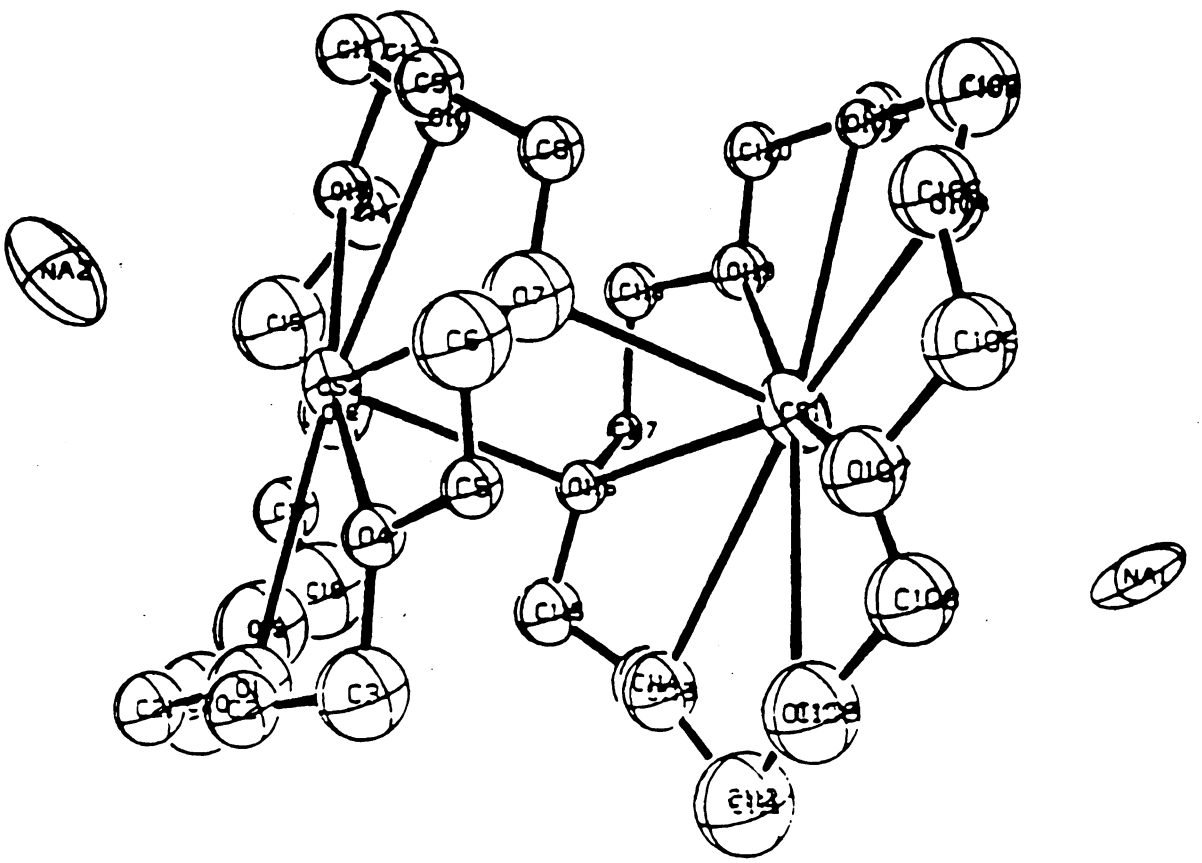

Figure 5.1: Ortep diagram of $Cs^{+}_{2}(21C7)_{2}Na^{-}_{2}$.

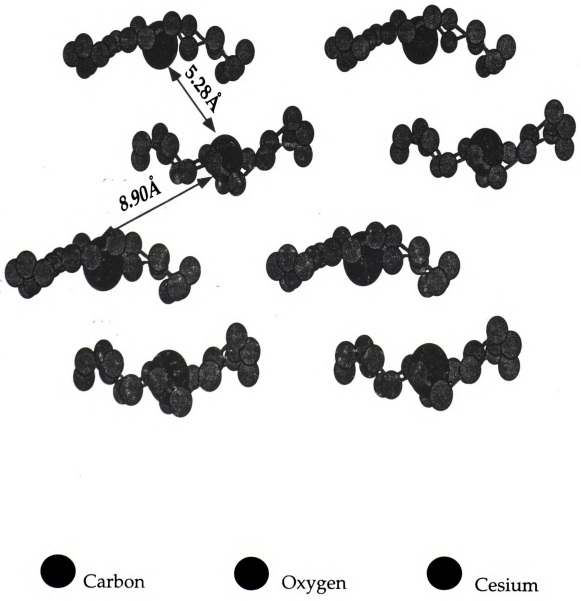

Figure 5.2: One view of four unit cells of $Cs^{+}_{2}(21C7)_{2}Na^{-}_{2}$.

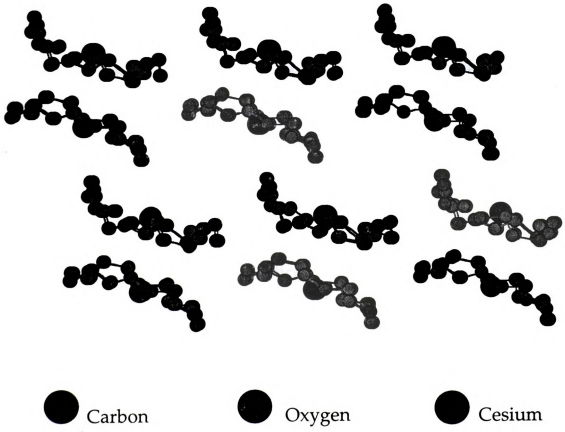

Figure 5.3: Alternate view of the packing of $Cs^{+}_{2}(21C7)_{2}Na^{-}_{2}$.

Physical Properties of $Cs^+_2(21C7)_2Na^-_2$

Since this is the only alkalide to date with two cation-anion contact ion pairs in one molecule with two closely separated cations, it was important to determine as much experimental data about this complex as possible. One might expect the charge to transfer from Na^- to the Cs^+. The properties ascertained include optical spectroscopy, NMR and differential scanning calorimetry (DSC), as well as EPR methods which will be reported separately in this chapter.

Optical Spectroscopy

The solvent evaporated optical spectrum (Huang, 1994) of this alkalide revealed a peak at 650 nm typical of Na^- (Figure 5.4a) This indicates that an electron from the $3s^2$ ground state is excited into the 3s3p state. These data also suggests that there is no compelling difference between the two different Na^- atoms found in the crystal structure. However, the fact that the absorption is broad may indicate that two sodide peaks have coalesced into one broad feature. The data were found to be temperature independent in the range of 153 to 253 K.

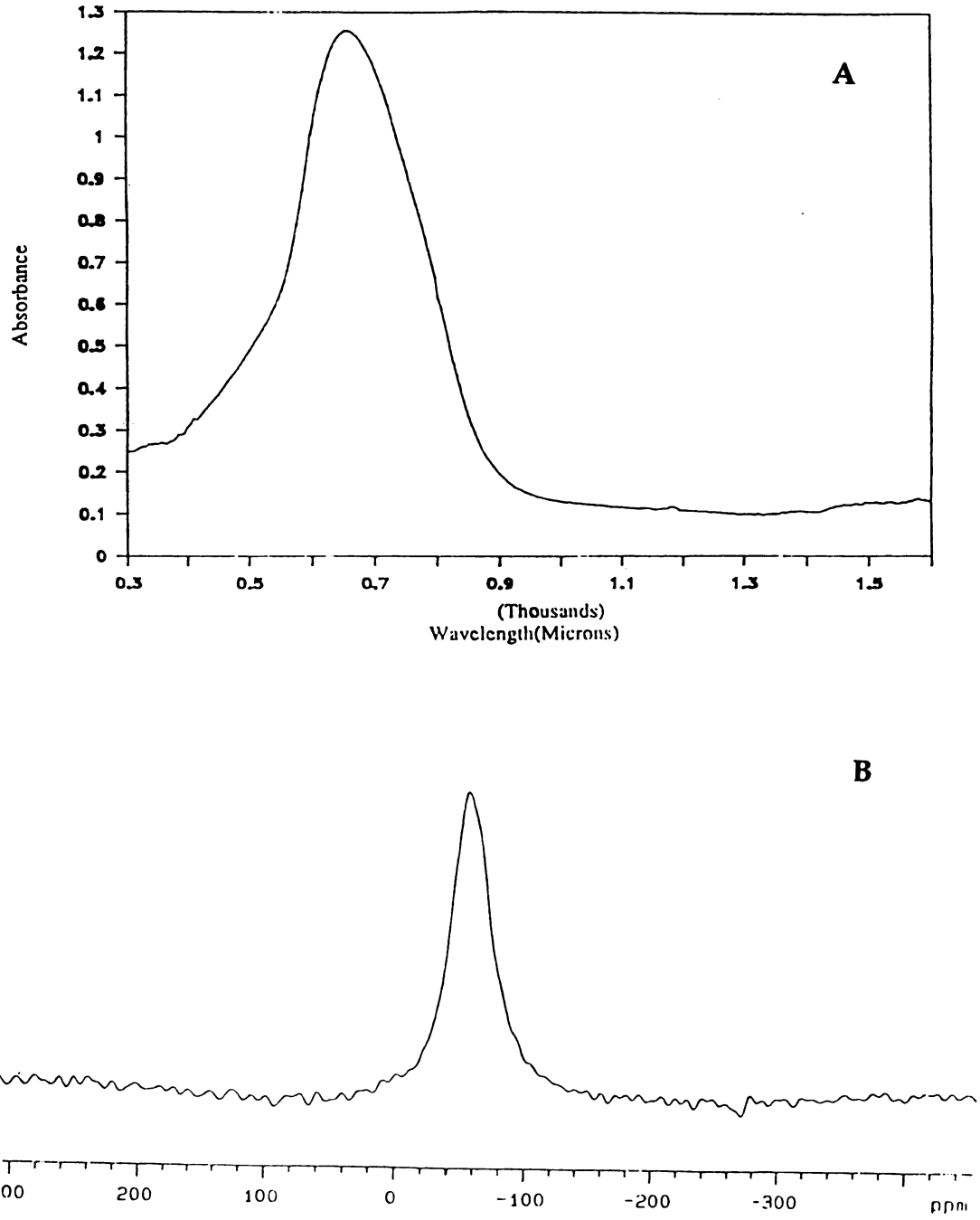

Figure 5.4: A) Optical spectrum of the solvent evaporated film of $Cs^{+}_{2}(21C7)_2Na^{-}_{2}$ in $MeNH_2$. B) ^{23}Na static NMR spectrum of $Cs^{+}_{2}(21C7)_2Na^{-}_{2}$ powder.

NMR

Both static and MAS-NMR data were collected (Huang, 1994) on crushed crystals of the alkalide. Two temperature independent peaks were observed in the ^{133}Cs NMR at -28 and +60 ppm, indicating that the Cs cations are chemically and magnetically nonequivalent. These data along with the range of Cs-O distances, render the Cs cations chemically nonequivalent. The spectra can be found in Figure 5.5. The ^{23}Na NMR reveals one single peak located at -56.3 ppm (Figure 5.4b). This peak position is in the usual region for sodides, about -60 ppm. A temperature dependence of the chemical shifts showed no dependence in the range of 173 to 263 K. The resonance has a full width half maximum (FWHM) of about 40 ppm which is consistent with the assignment.

DSC

Differential scanning calorimetry (Huang, 1994) gives stability information about the compound under observation. A temperature ramp of 5°C/minute was chosen and displayed the onset of decomposition at 120°C. The ΔH associated with that transition was calculated to be -168 kJ/mol. There was also a small irreversible endothermic transition at -68°C with ΔH=5 kJ/mol. This may have been due to decomplexation, where the cation and complexant break bonds between them but the

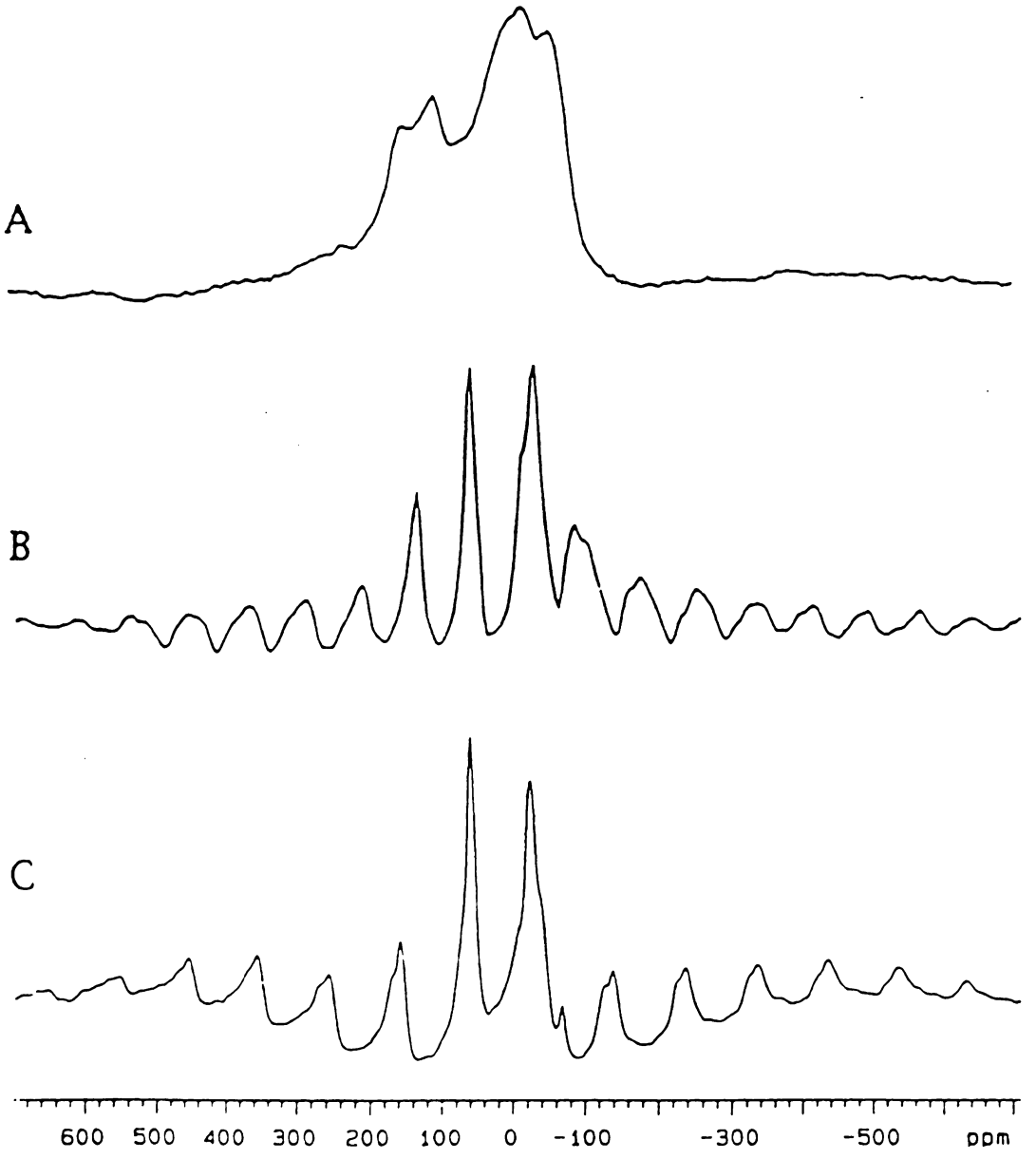

Figure 5.5: A) ^{133}Cs static NMR spectrum recorded at 200 K. ^{133}Cs MAS-NMR spectrum recorded at 200 Kat B) 5 kHz spinning speed and C) 10 kHz spinning speed.

molecules remain intact without decomposing. This was evident in solution to occur at about -49°C. It appears that this compound is pretty stable in the solid state possibly because of the highly extensive coordination between the Cs cations and the O atoms of the crown ether. In addition, the Cs^+-Na^- ion pair may be responsible for some added stability to the complex.

Summary of the Physical Properties

The interesting feature of two contact ion pairs on both sides of the Cs cations, gives intrigue to the $Cs_2^+(21C7)_2Na_2^-$ complex. The large complexants are usually 'soft' or flexible and this presents difficulties in single crystal growth possibly resulting in disorder. Pedersen (Pedersen, 1967, Pedersen, 1968) stated that the cation size and the cavity size of the complexant are important variables in judging the stability of complexation. During crystallization, disorder can be caused by a packing irregularity or by thermal motion. Although the crystals were not very big, as crystal sizes of alkalides go, the structure was determined and many of the physical properties resolved. There were no indications of charge transfer from the ^{23}Na NMR data or from the Na^- peak of the optical spectrum; thus, it appears that there is no significant difference between well isolated Na anions and those which are near the cation.

Pulsed and cw-EPR experiments

Continuous wave and advanced EPR methods were chosen to probe the electronic environment and to map the electron density, since the crystal structure affords a well understood geometry. Moreover, the question regarding the vicinity of the electron density is addressed by using advanced EPR methods. Crushed crystals of $Cs_2^+(21C7)_2Na_2^-$ were loaded into an EPR tube as described earlier. Since alkalides are intrinsically diamagnetic, the presence of defect electrons is relied upon. The concentration of defect electrons cannot be measured directly, but by changing the stoichiometry of the starting materials, a relative estimate can be made. The cw-EPR spectrum is shown in Figure 5.6a. The data were collected on a Bruker ER 200D spectrometer operating at X-band. The EPR signal has an axial g-tensor with $g_{//}$= 2.145 and $g_{\perp}$ = 1.996. The perpendicular feature is split into six lines with a coupling constant of 10 G. The microwave power saturation study shows saturation occurs at relatively low power (.2 mW) at both 4 and 50 K. The ESE-detected EPR spectrum displays a broad 550 G wide asymmetric eight line pattern, indicating one cesium nucleus is coupling to the paramagnetic center (Figure 5.6b). The tau value used was 250 ns, a resonant frequency of 10.011 GHz, repetition rate of 50 Hz and 45.0 dBm microwave power. We were most interested in determining the distance between the Cs^+ and the

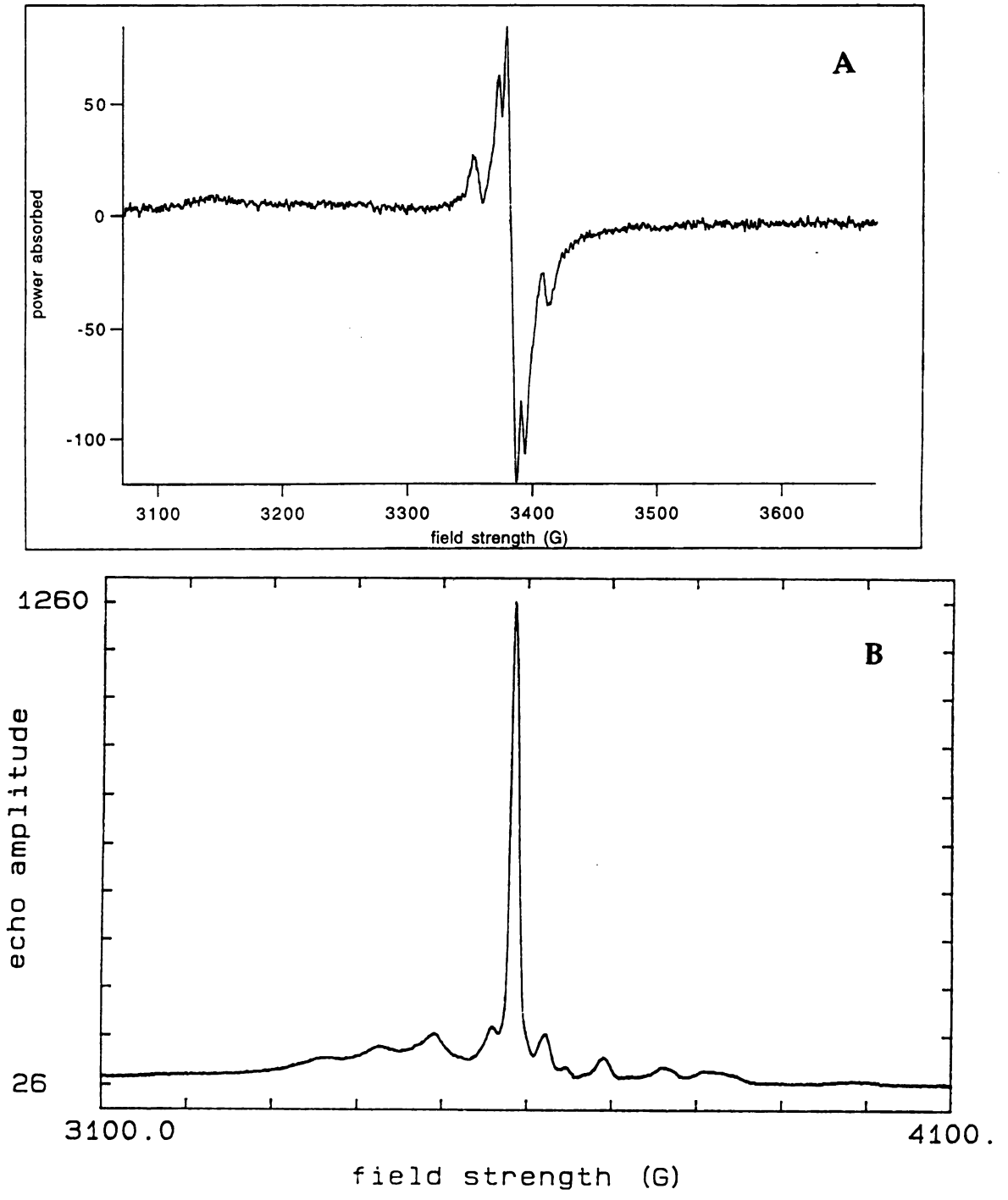

Figure 5.6: A) cw-EPR spectrum collected at 2.08 μW microwave power, 9.4716 GHz microwave frequency, 5.2 Gpp modulation amplitude, 100 kHz modulation amplitude, $5x10^5$ gain and 3.8 K. B) ESE-EPR spectrum collected at 4.2 K, 250 ns τ, 50 Hz repitition rate, 45.0 dBm microwave power, 10.011 GHz microwave frequency.

trapped electrons, to see if they do in fact occupy the anionic vacancies. Often there are weak superhyperfine interactions between the paramagnetic center and the nearby magnetic nuclei that are unresolved due to inhomogeneous broadening. The 2-pulse ESEEM data reveal a textbook example of peaks due to the larmor frequency as well as the combination line at twice the larmor frequency (see modulation function for a 2-pulse experiment in chapter 3). In Figure 5.7a, the time domain trace reveals a weak modulation pattern that dampens modestly. The fourier transform of this trace, 5.7b, shows a sharp peak at 1.87 MHz assigned to the Cs nucleus, at the field strength of 3324.0 G. In addition, the negative going peak at 3.56 MHz (twice that of 1.87) is the sum combination line of cesium . Since there are many protons in the crown ether, it is expected that a proton matrix line would also be present at the larmor frequency of protons, 14 MHz. Note also the sum combination line at 28 MHz. The 3-pulse data collected at several different τ values yield the same peak positions, just different intensities of the lines depending on the τ value. Figure 5.8a,b shows the 3-pulse data at 9.282 GHz. The peaks at 1.830 MHz and 14.217 MHz can once again be assigned to cesium and protons respectively. These data suggest that both cesium and protons couple to the unpaired electron, but to make a more definitive assignment, it is necessary to change the frequency of the resonator. By changing the resonator and therefore the frequency, the new frequencies of the peaks

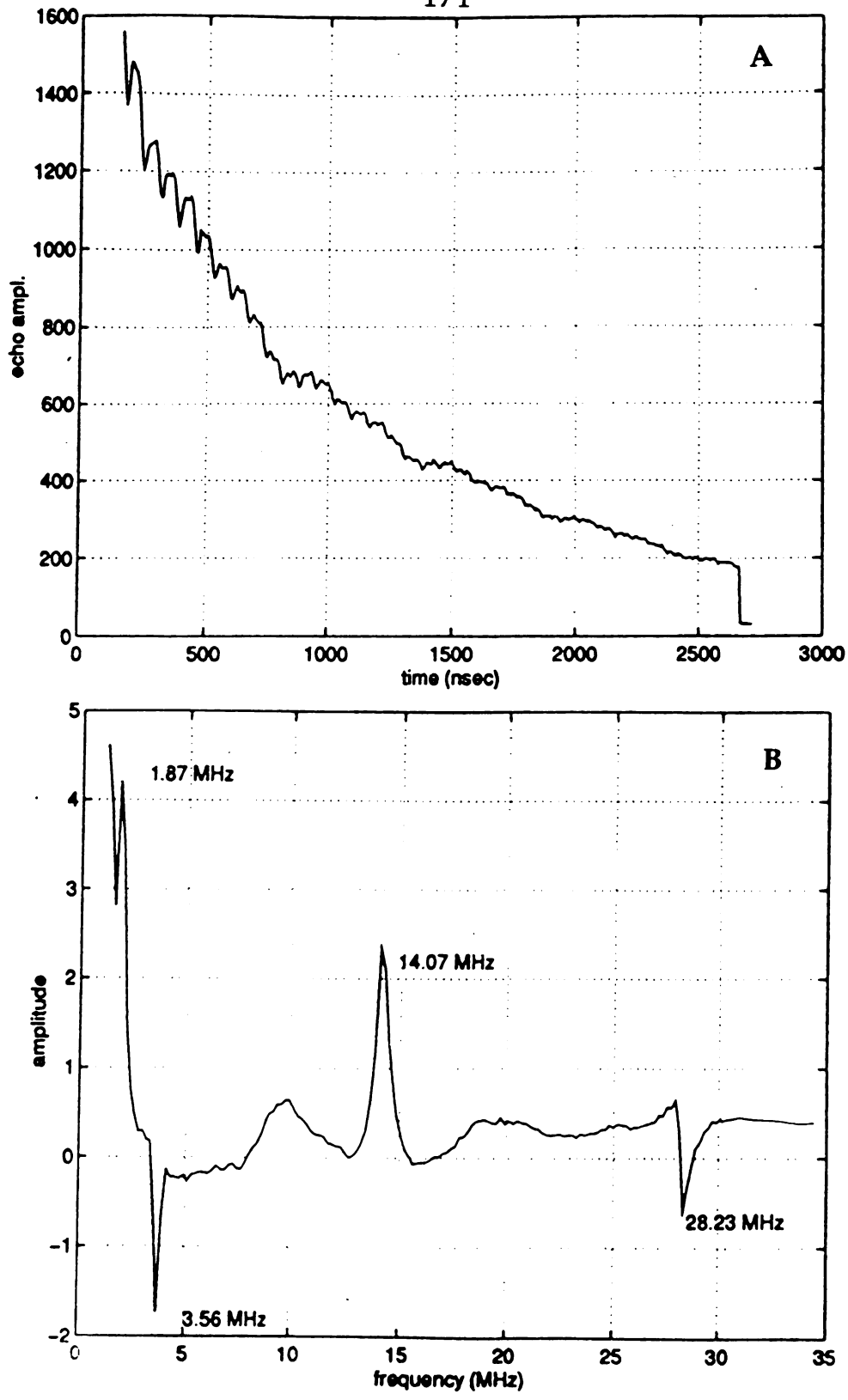

Figure 5.7: A) 2-pulse ESEEM trace collected at 9.282 GHz microwave frequency, 3324.0 G field strength, 180 ns τ, 10 Hz repetition rate and 4 scans collected. B) fourier transform spectrum of trace A.

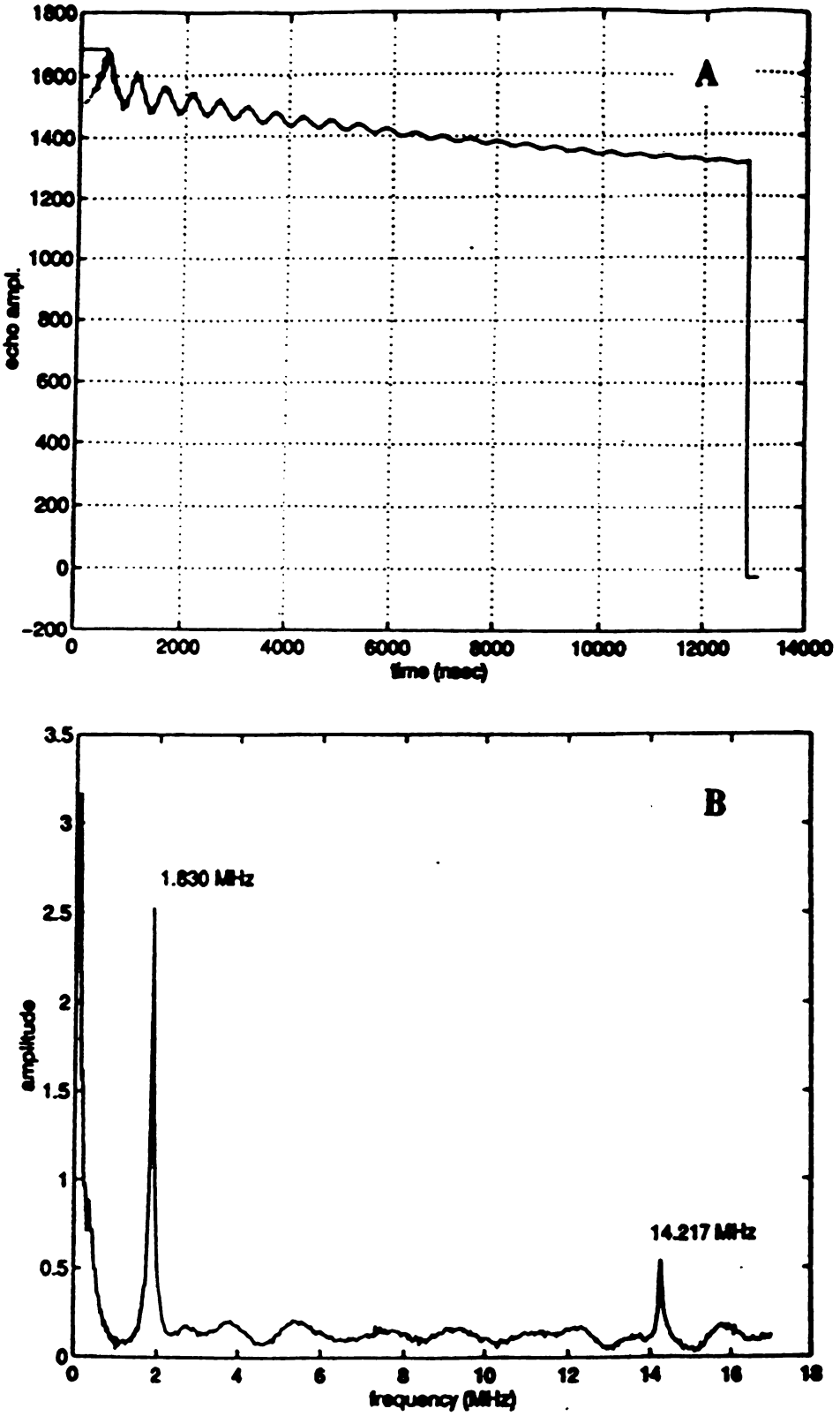

Figure 5.8: A) 3-pulse ESEEM trace collected at 9.282 GHz microwave frequency, 3324.0 G field strength, 180 ns τ, 10 Hz repetition rate and 16 scans collected. B) fourier transform spectrum of trace A.

should lend support to the assignments made. Figure 5.9a,b exhibits the effects from increasing the frequency to 11.358 GHz. Once again both the cesium and proton nuclei are represented by positive and negative peaks at the proper frequency corresponding to the change in field strength and the line positions in the three pulse experiments were assigned to cesium and protons again.

It may seem as though no additional information can be gained by these types of experiments; however, it is the time domain trace that holds much of the information. Simulation of the time domain 3-pulse trace should give information regarding the distance between the Cs nucleus and the paramagnetic center. The simulation program that was used was developed based on a perturbation method by Shubin and Dikanov (Shubin & Dikanov, 1988) for I>1/2 systems. This treatment assumes the anisotropy and the nuclear quadrupole interaction are much smaller than the nuclear Zeeman interaction. The perturbation Hamiltonian is diagonalized and the Eigenvalues are solved. The modulation function described in chapter 3 can be expressed as, (Eq. 5.3),

$$E_{mod}(\tau,T) = 1\text{-}k\{\sin^2 1/2(\omega\tau(1-\cos\omega[\tau+T]))\} \qquad (5.3)$$

where the modulation depth parameter, $k = (B/\omega)^2$ and B is the dipolar component of the hyperfine interaction. Since the dipolar part has a $1/r^3$ dependence within it, the modulation depth then goes as $1/r^6$! Because of

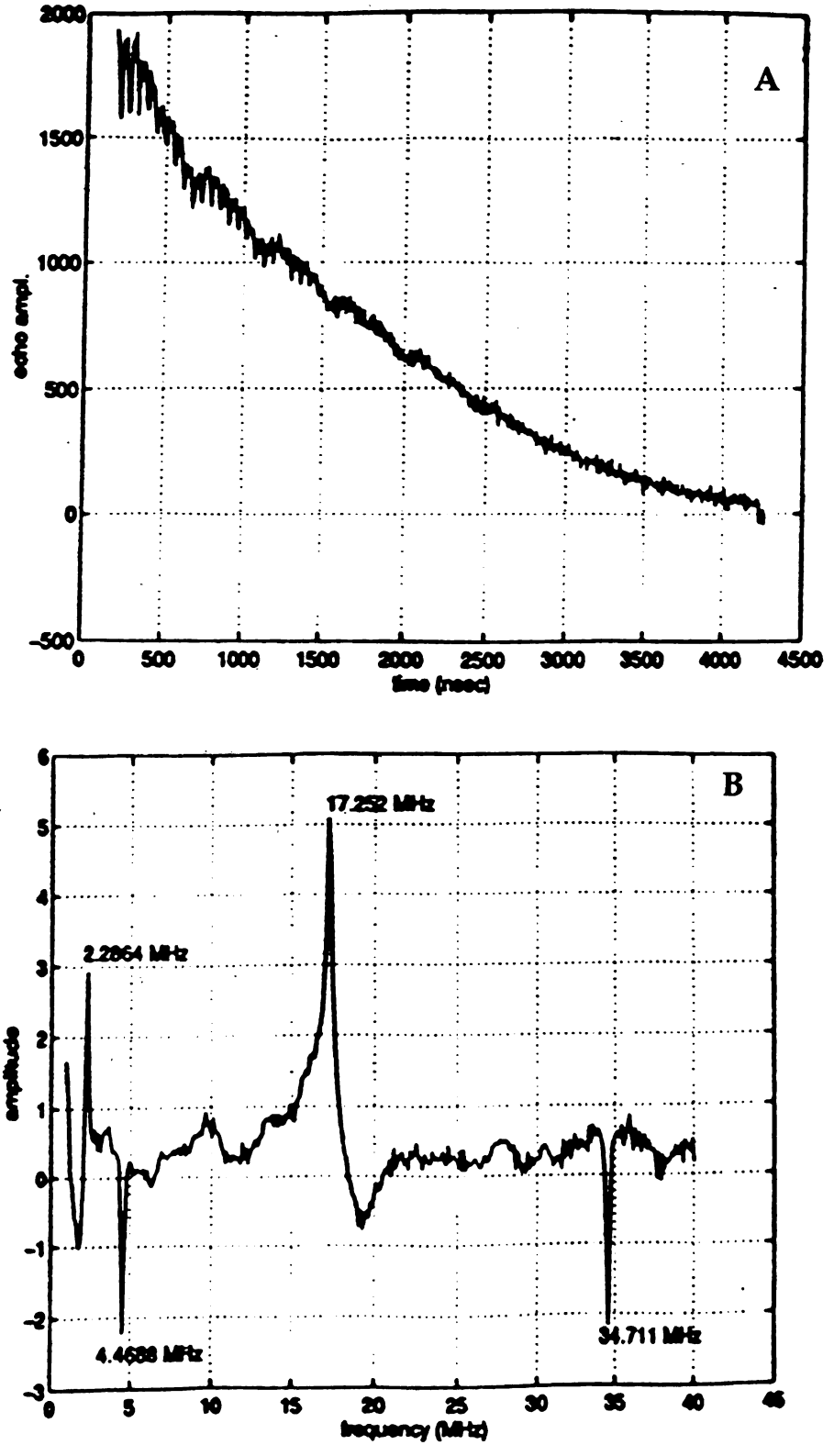

Figure 5.9: A) 2-pulse ESEEM trace collected at 11.358 GHz microwave frequency, 4068.0 G field strength, 180 ns t, 10 Hz repetition rate. B) fourier transform spectrum of trace A.

this strong dependence, there is a lot of weight put on the internuclear distance, as the modulation pattern can change drastically as r changes. This is illustrated in Figure 5.10. Table 5.1 demonstrates the relationship between the time domain trace and fourier transform spectrum.

Table 5.1
Comparison Between the Time Domain and the Frequency Domain

TIME DOMAIN		FOURIER TRANSFORM
period	*corresponds to*	frequency
amplitude of modulation	*corresponds to*	amplitude of frequency
damping of modulation	*corresponds to*	linewidth of peak

For large values of r, one would expect small anisotropy, modest damping, and narrow lines while small values of r should lead to broad lines, deep modulations and fast damping. In addition, the modulation depth is a function of the nuclear spin and goes as I(I+1). Since Cs has a nuclear spin equal to 7/2, one might expect deep modulations, but since **r** is large, the modulation depth is weakened. The modulation depth is about 10% of the echo amplitude and Figure 5.11 shows the best simulation, with an internuclear distance of 4.9 Å. The fourier transform (Figure 5.11b) displays a frequency at 1.87 MHz which is consistent with

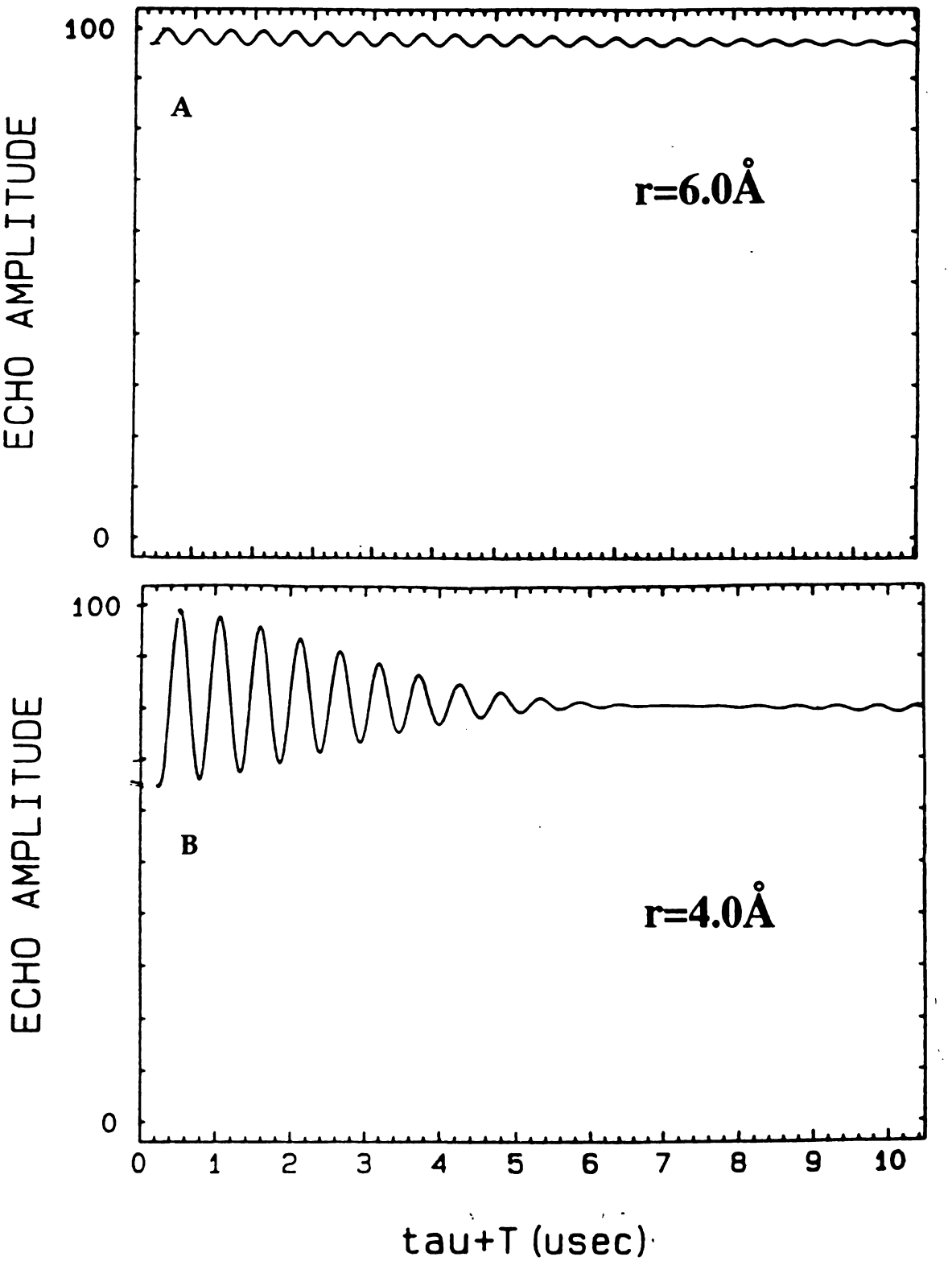

Figure 5.10: Simulations of the time domain trace from the 3-pulse ESEEM experiments of $Cs^+(21C7)Na^-$ at 9.282 GHz, and an internuclear distance parameter, r, of A) 6.0 Å and B) 4.0 Å.

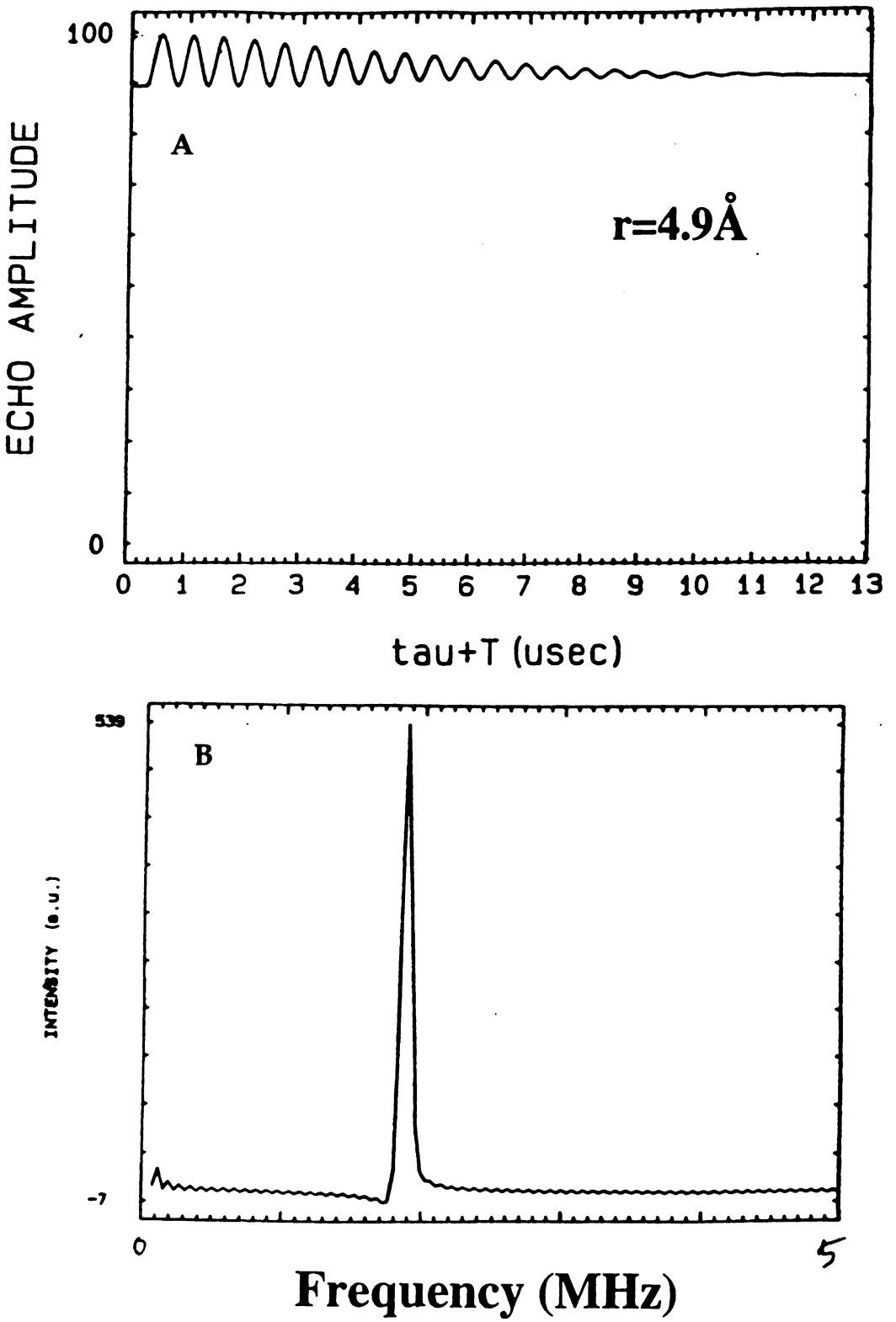

Figure 5.10: A) Best simulations of the time domain trace from the 3-pulse ESEEM experiments of $Cs^+(21C7)Na^-$ at 9.282 GHz, with an internuclear distance parameter, r, of 4.9 Å. B) Fourier transform of A.

the assignment made from the ESEEM data.

Discussion

It is clear from the EPR results that a cesium nucleus is interacting with a trapped electron. The Cs-Na distances are 4.44 and 4.48 Å as determined from the crystal structure, which is slightly smaller in distance than that obtained from the ESEEM studies. However, these data still lend support to the F-center model and argue against Golden and Tuttle's conclusions as described in chapter 1. They claim that in $Cs^+(18C6)_2e^-$, the valence electron is in the *near vicinity* of the Cs^+. It is not stretching the imagination to suggest that the electron occupying the occasional anionic vacancy in $Cs^+_2(21C7)_2Na^-_2$ does not remain in one position but instead is smeared over a large area thus yielding longer electron nuclear distance. If the electron density were in close proximity to the Cs nucleus of $Cs^+_2(21C7)_2Na^-_2$, the modulation pattern would appear drastically different. These ESEEM results are thus the most definitive evidence that the electron does occupy the anionic vacancy of the alkalide. Although electride samples produce a strong free induction decay (FID) corresponding to a long value for T_2, no spin echo is observed. This is consistent with the homogeneous line that typical electrides produce. Currently the electride of this alkalide has not been successfully crystallized, and there is no guarantee that the geometry would be

isostructural to that of $Cs^{+}_{2}(21C7)_2Na^{-}_{2}$. By using the visualization method (Dye *et al.*, 1996), the channel and cavity diagram for $Cs^{+}_{2}(21C7)_2Na^{-}_{2}$ is shown in Figure 5.12. Note the large channels in one direction (2.2Å) with a narrow connection (1.2Å). This picture is consistent with a slightly longer simulated distance between the unpaired electron and the paramagnetic center. The "hypothetical" electride may not have the same channels and cavity structure. In an effort to synthesize the "hypothetical" electride, attempts were made to reduce the stoichiometric quantity of Na^{+}, increasing the doping level until crystals were made with no Na added. Unfortunately, when a deficiency of > 25% Na is attempted, crystal formation does not occur, so until our crystallization methods are improved, this electride will have to remain "hypothetical".

---

† It is worth noting that all of the spectroscopy was collected on various samples from different preparations. Some samples were doped heavily, while others were not. The end result was the same in all cases except that the signal intensity changed according to the doping level. A synthesis prepared from the stoichiometric ratio of Cs:Na:21C7 of 1:1:.75 resulted in a 25% deficiency of Na available to accept the unpaired electron, therefore results in a highly doped sample.

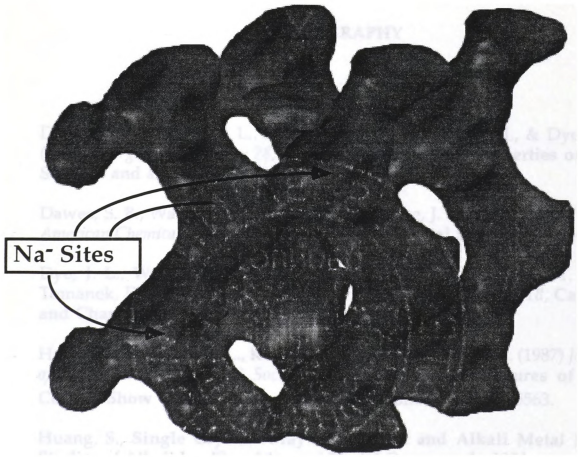

Figure 5.12: Cavity and channel diagram of $Cs_2^+(21C7)_2Na_2^-$ revealing the anionic sites that the trapped electrons most likely occupy. The channels reveal the pathway that the electron has to move from anionic site to anionic site.

BIBLIOGRAPHY

Dawes, S. B., Ward, D. L., Fussa-Rydel, O., Huang, R.-H., & Dye, J. L. (1989) *Inorganic Chemistry 28*, **Crystal Structures and Properties of Two Sodides and an Electride**, 2132-2136.

Dawes, S. B., Ward, D. L., Huang, R. H., & Dye, J. L. (1986) *Journal of the American Chemical Society 108*, **First Electride Crystal Structure**, 3534-3535.

Dye, J. L., Wagner, M. J., Overney, G., Huang, R. H., Nagy, T. F., & Tomanek, D. (1996) *Journal of the American Chemical Society 118*, **Cavities and Channels in Electrides**, 7329-7336.

Huang, R. H., Ward, D. L., Kuchenmeister, M. E., & Dye, J. L. (1987) *Journal of the American Chemical Society 109*, **The Crystal Structures of Two Cesides Show That Cs^- is the Largest Monatomic Ion**, 5561-5563.

Huang, S., **Single Crystal X-ray Diffraction and Alkali Metal NMR Studies of Alkalides, Electrides and Model Compounds**, 1994.

Pedersen, C. J. (1967) *Journal of the American Chemical Society 89*, **Cyclic Polyethers and their Complexes with Metal Salts**, 2495-2496.

Pedersen, C. J. (1968) *Federation Proceedings 27*, 1305.

Pedersen, C. J. (1970) *Journal of the American Chemical Society 92*, **Cyclic Polyethers and Their Complexes with Metal Salts.**, 386.

Pedersen, C. J., & Frensdorff, H. K. (1972) *Angewendte Chemie International Edition 11*, **Macrocyclic Polyethers and Their Complexes**, 16-25.

Shubin, & Dikanov. (1988) .

Tehan, F. J., Barnett, B. L., & Dye, J. L. (1974) *Journal of the American Chemical Society 96,* **Alkali Anions. Preparation and Crystal Structure of a Compound Which Contains the Cryptated Sodium Cation and the Sodium Anion**, 7203-7208.

Chapter 6

Multifrequency ESEEM Studies of Potassium Hexamethyl Hexacyclen Sodide

Background Information

Thermodynamic considerations by Golden and Tuttle suggested that alkali metal anions could exist in liquid ammonia . The Dye group pursued salts of alkali metal anions based on thermodynamic considerations. Unfolding new combinations of alkali metals, complexants and solvents is of primary interest. In principle, the alkaline earth metals or even lanthanides could be the cation. In practice, this is not as simple. Such attempts were made but met with little success. For instance, effort was made to synthesize crystals of $Ba^{2+}(C222)Na^-$ but the synthesis always failed, not even resulting in powder alkalide (Huang, 1994). It seemed reasonable that a more robust complexing agent might help stabilize other types of alkalides.

The utility of alkalides and electrides has been limited due to their thermal instability, resulting from reductive attack on the ether oxygen by either the weakly bound or unbound electrons. The quest for more robust complexing agents led to the implementation of a type of complexant that was more resistant to reductive decomposition. This complexant, hexamethyl hexacyclen (hereafter referred to as HMHCY), was successfully used to produce a more stable alkalide. This fully methylated aza analog

of 18C6, was presumably less reactive due to the replacement of the oxygen ether atoms with the less reactive nitrogen atoms. Three sodides of alkali metal cations K, Rb and Cs were crystallized with HMHCY as the complexing agent. In addition, crown ether complexants such as 12C4 were used to try to place a "cap" over the Cs^+(HMHCY)Na^- complex (Figure 6.1). The Cs cation fits rather well inside of the HMHCY complexant, but sits about .91 Å above the plane of the four nearly planar

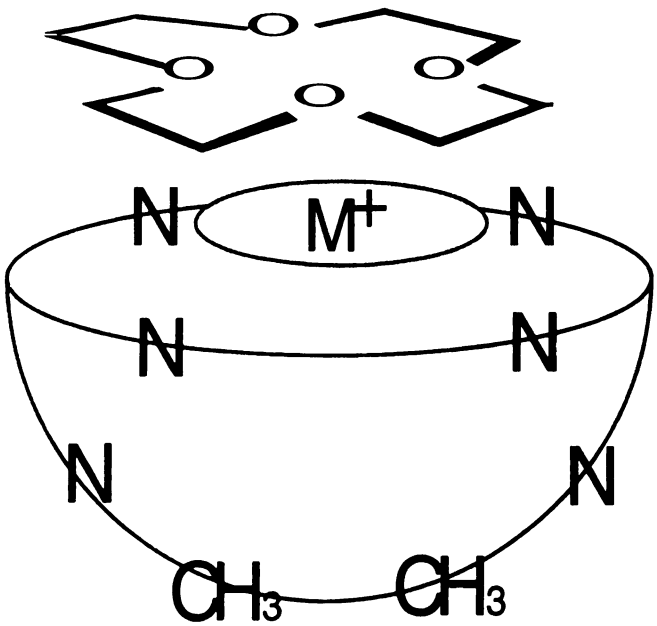

Figure 6.1: Attempts to "cap" the alkali metal cation complexed by HMHCY with 12C4, have thus far failed. Note the cup formation of HMHCY with four nitrogens in the same plane and the methyl groups of the other two nitrogens closing off the bottom of the cup.

N atoms. Based on this, it was proposed that perhaps the 12C4 could "cap" the Cs cation. Every attempt resulted in crystals of Cs^+(HMHCY)Na^-,

verified with X-ray crystal diffraction, and crystals of 12C4. Attempts were made to synthesize Ba^{2+}(HMHCY)Na^- but only a oily liquid was present after several different solvent systems were attempted (Huang, 1994). Currently, there has been no success at synthesizing alkaline earth sodides, or by capping the Cs^+(HMHCY)Na^-.; however, this very robust complexant has served to make three very stable sodides that will the topic of this chapter.

Structural Information

The structure of three HMHCY sodides, have been determined (Kuchenmeister & Dye, 1989, Ward *et al.*, 1989). All three of the HMHCY sodides crystallize in the orthorhombic crystal system. The four nitrogens at positions 4, 7, 13 and 16 are all coplanar to within 0.09Å in the K^+(HMHCY)Na^- and within 0.03Å in Cs^+(HMHCY)Na^-. The methyl groups that are bonded to these nitrogens form a cage around the alkali metal cation. The other two nitrogens at positions 1 and 10 are below the plane of the other four nitrogens by 1.62 Å and 1.23 Å for K^+ and Cs^+ respectively. The methyl groups associated with these two nitrogens essentially close off the bottom of the ring, exhibiting a "cup" formation (Figure 6.1). Both cations are coordinated to all six nitrogens with cation-nitrogen distances ranging from 2.90 to 3.01 Å and 3.17 to 3.35 Å for K and Cs, respectively. The K^+ is located 0.29 Å above the nitrogen ring and Cs^+

is located 0.91 Å above the nitrogen ring. The Cs^+-Na^- distance is 4.28 Å and the K^+-Na^- distance is 4.26 Å. This information, together with the fact that the cations sit slightly above the plane of the complexant ring, make interaction with trapped unpaired spins occupying anionic vacancies, more likely. This structural information renders this a close ion pair, without destroying the rudimentary character of the ions. All pertinent distances are shown in Figure 6.2, and cation-anion packing views are shown (Figure 6.3, and 6.4).

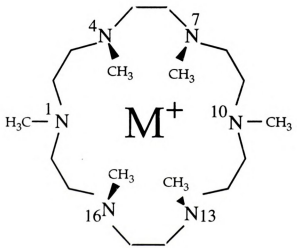

K^+ is located 0.29Å above the center of the plane
Cs^+ is located 0.91Å above the center of the plane

K-N distance ⟶ 2.90-3.10Å
Cs-N distance ⟶ 3.17-3.35Å

Na^- distance from K^+ ⟶ 4.28Å
Na^- distance from Cs^+ ⟶ 4.26Å

Figure 6.2: Structural information for two HMHCY sodide.

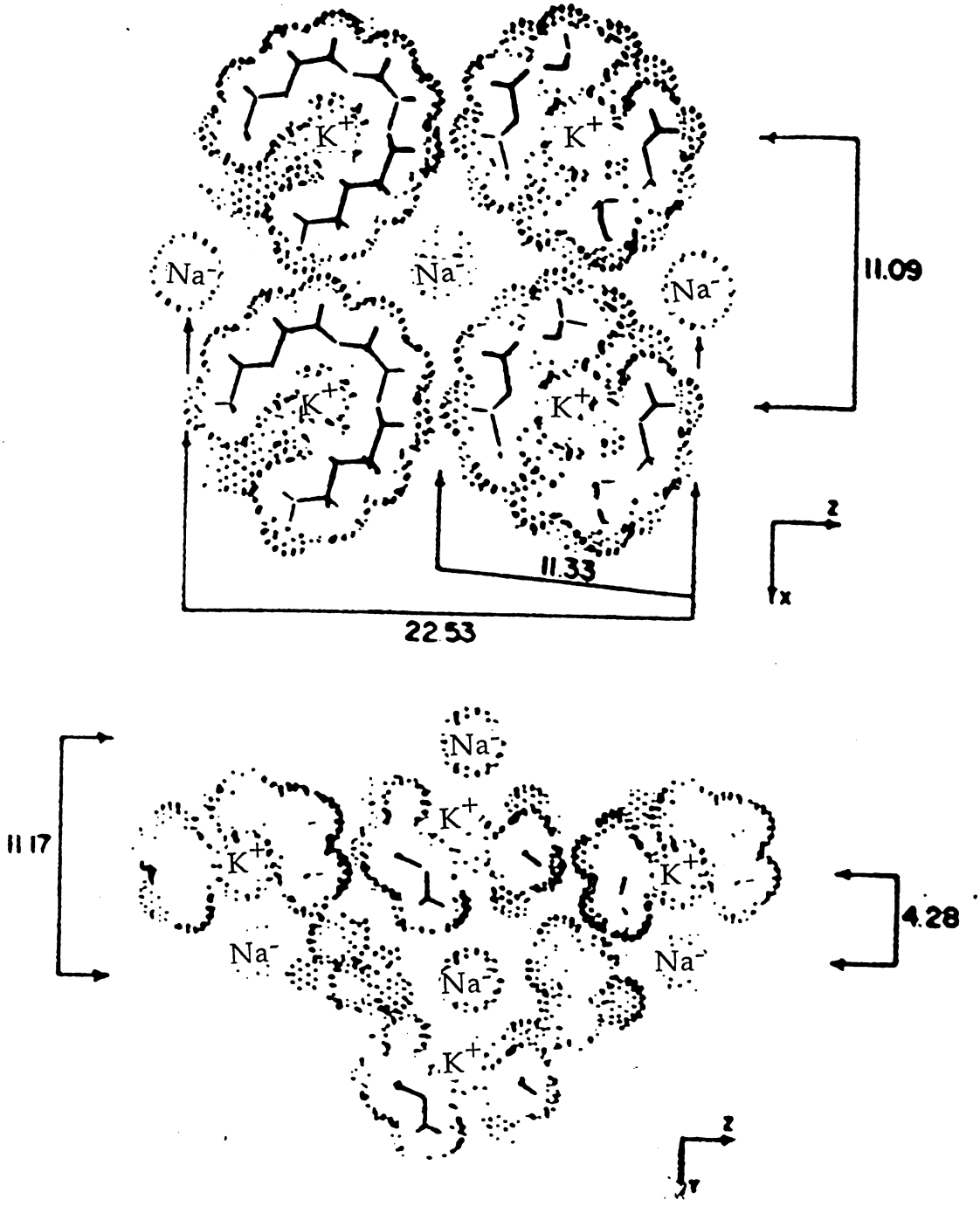

Figure 6.3: Diagram of K^+(HMHCY)Na^-

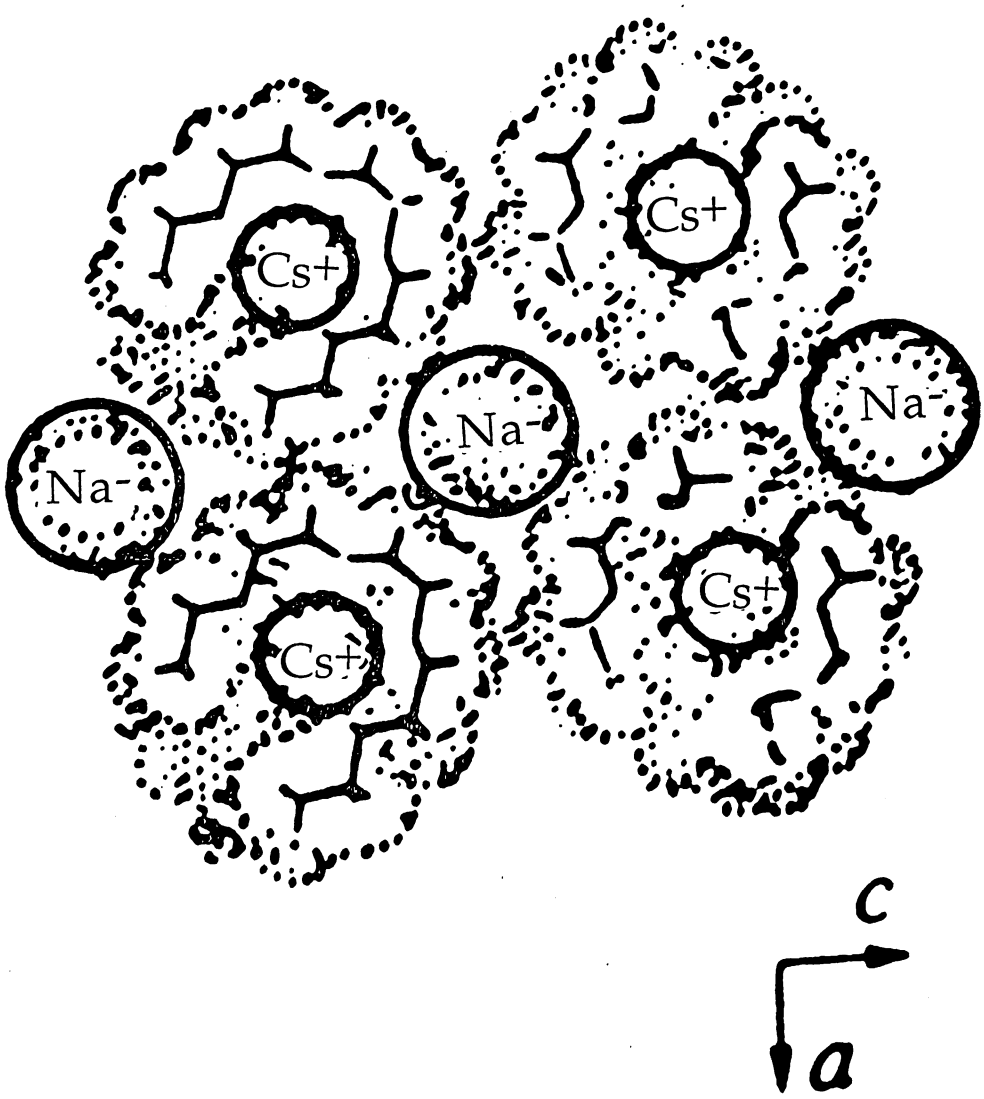

Figure 6.4: Perspectives of Cs^+(HMHCY)Na^-

Thermal Stability

Samples were prepared under an inert nitrogen atmosphere and hermetically sealed in anodized aluminum sample pans for DSC measurement. The initial melting point of K^+(HMHCY)Na^- was measured to be 42 °C but decomplexation into the metals, probably NaK alloy and free amine, occurred at 74°C. Temperatures up to 120°C revealed no additional decomposition, suggesting that even in the presence of alkali metals, the HMHCY complexant is resistant to reductive attack. This sodide is stable at room temperature for up to four days, at which point it decomplexes. In the case of the Cs^+(HMHCY)Na^-, the onset of melting occurs at about 8°C with decomplexation occurring at 37°C. This sodide also decomplexes after about four days, rendering a slow melt in both cases.

EPR Studies

Studying the electronic environment of alkalides and electrides is the theme of this dissertation and the HMHCY compounds proved to be a good subject. Due to the exchange narrowing EPR properties of most electrides, isolation of the trapped electrons in alkalides proved to be more successful at determining hyperfine interactions. Since the alkalides sometimes form *sandwich* complexes as do the electrides, the alkali metal

cation cannot communicate with the unpaired electron spin of the defect electrons since the cations are well shielded from the trapped electrons. This reduces the chances of obtaining hyperfine interactions in the EPR . For example, an EPR comparison was done between three *sandwich* sodides and three HMHCY sodides (Shin *et al.*, 1991). In the sandwich compounds, [$Cs^+(18C6)_2Na^-$, $Cs^+(15C5)_2Na^-$, $Cs^+(12C4)_2Na^-$], each Cs^+ ion is encapsulated between pairs of the respective crown ether, while the Na^- ion is surrounded by eight such complexed cations, at roughly equal distances. In the other compounds, each HMHCY complexed Cs^+, Rb^+ or K^+ is nearly in contact with Na^- at much larger distances from other anionic sites.. The EPR measurements revealed only a single line for the two sandwich compounds, $Cs^+(15C5)_2Na^-$ and $Cs^+(12C4)_2Na^-$ with *g*-values of 2.0020 and 2.0025, respectively, suggesting very little spin-orbit coupling. The peak to peak line widths were 2.21 and 4.40 G respectively. In contrast, the sandwich compound $Cs^+(18C6)_2Na^-$ showed a broad line with a sharp central narrow line. Each synthesis was slightly different so the relative intensities of the two peaks also varied. The spectrum showed no resolved hyperfine coupling and the line broadening was originally thought to come from superhyperfine interactions with several surrounding nuclei rather than a shifting of the *g*-values. High field EPR experiments later determined that the two peaks were due to trapped electrons residing at two magnetically non-equivalent sites.

The differences in the structures of these two families of compounds clearly agrees with the fact that hyperfine interactions are observed for the contact HMHCY complexes, while none is seen for the sandwich compounds.

ESEEM Studies

Multifrequency ESEEM experiments were used to study the electron trapping sites in these thermally stable sodides, with a precise goal to determine charge distribution. As was mentioned in the previous chapter, direct evidence of the electron trapping sites has not been shown until the ESEEM method was used. eseem experiments were used to measure the weak superhyperfine couplings to trapped electrons in Cs^+(HMHCY)Na^- (McCracken *et al.*, 1992). They showed that two magnetically distinct groups of ^{133}Cs were present.

Three pulse stimulated echo ESEEM data collected at g=1.998 is shown in Figure 6.5. The tau value was initially taken at 250 ns and the ESEEM time domain trace exhibited strong proton modulations. These data, when fourier transformed, show a relatively large peak at 14 MHz, and another large peak near the low frequency edge, at 0.65 MHz. In addition there is a small rather sharp peak located at 3.9 MHz. These peaks have been assigned to protons, potassium and sodium, respectively, based on their larmor frequencies at a field strength of 3391 G. Choosing

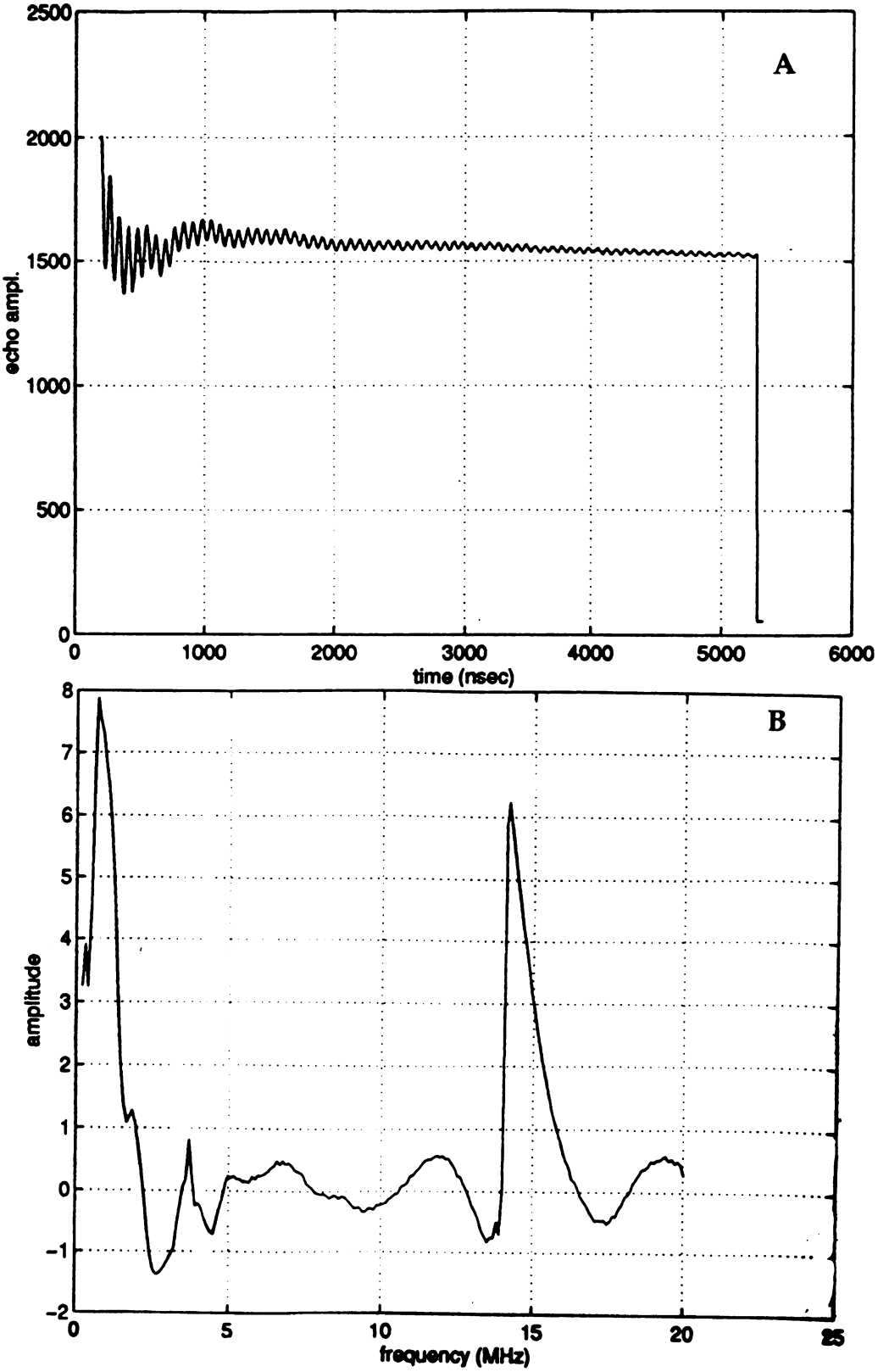

Figure 6.5: A) 3-pulse ESEEM trace of K^+(HMHCY)Na^- at 3300 G, where τ = 288 ns., T=42 ns., tinc = 10 ns., repetition rate = 40 Hz. B) Fourier transform spectrum of A.

the tau value is very important and can aid in peak assignments. The equation for the modulation function reveals that there is a tau dependence on the stimulated echo frequencies. Therefore, if a certain tau value is chosen, it can serve to enhance or suppress certain modulations in the echo. For example,

$$h\nu_N = g_N\beta_N H \qquad (6.1)$$

where ν_N is the larmor frequency, g_N is the nuclear g-factor and β_N is the nuclear Bohr magneton. If the echo is collected at a field strength of 3391 G and a compound with many protons is under study, then the proton larmor frequency at that field strength is,

$$\nu_N = (5.5856912)(5.050824\times10^{-27}\text{J/T})(.03391\ \text{T}/6.63\times10^{-34}\ \text{J·s}) \qquad (6.2)$$
$$= 14.42\ \text{MHz}$$

and therefore, one might expect a peak to be centered at this frequency. Protons are often the most abundant element in a sample and the large modulations can then cause the intensity other frequencies to be diminished. To suppress the undesired contribution of matrix protons to the spectrum, the reciprocal of the larmor frequency will yield the tau value (and integral multiples) that should suppress the proton modulations (Mims, 1972, Mims & Peisach, 1989, Warncke & McCracken, 1994). In this case, multiples of 71 ns should be used to suppress the proton modulations and possibly bring out any other modulations that

are present in the echo envelope. Moreover, 1.5 times the reciprocal of the larmor frequency of the nucleus of interest, should enhance the modulations. Thus careful consideration must be given when choosing a tau value.

When a tau value was chosen to suppress the protons, 213 ns, the echo envelope revealed weak proton modulations as well as another modulation. The time domain trace and fourier transformed spectrum can be found in Figure 6.6. The large peak located at a frequency of 0.67 MHz was assigned again to potassium and the weaker peak at 14 MHz was due to protons, and the intensity was weakened significantly due to the tau suppression effect. Once again, a smaller more broad peak centered around 3.8 MHz was present. The initial judgment was to assign this peak to Na, however upon choosing the tau value that would enhance this feature, no increase in that frequency region was observed. This indicates that the peak cannot be assigned to Na.

The spectrometer dead time limits the start of data collection (140 ns). As a result, reconstruction of the dead time is necessary. To do this, a windowing function is employed where only the peaks that are believed to be real, are windowed. This often gives the lineshapes a more realistic appearance and depletes the baseline thus increasing the signal to noise ratio. When the 3.9 MHz peak is not windowed, it does not disappear

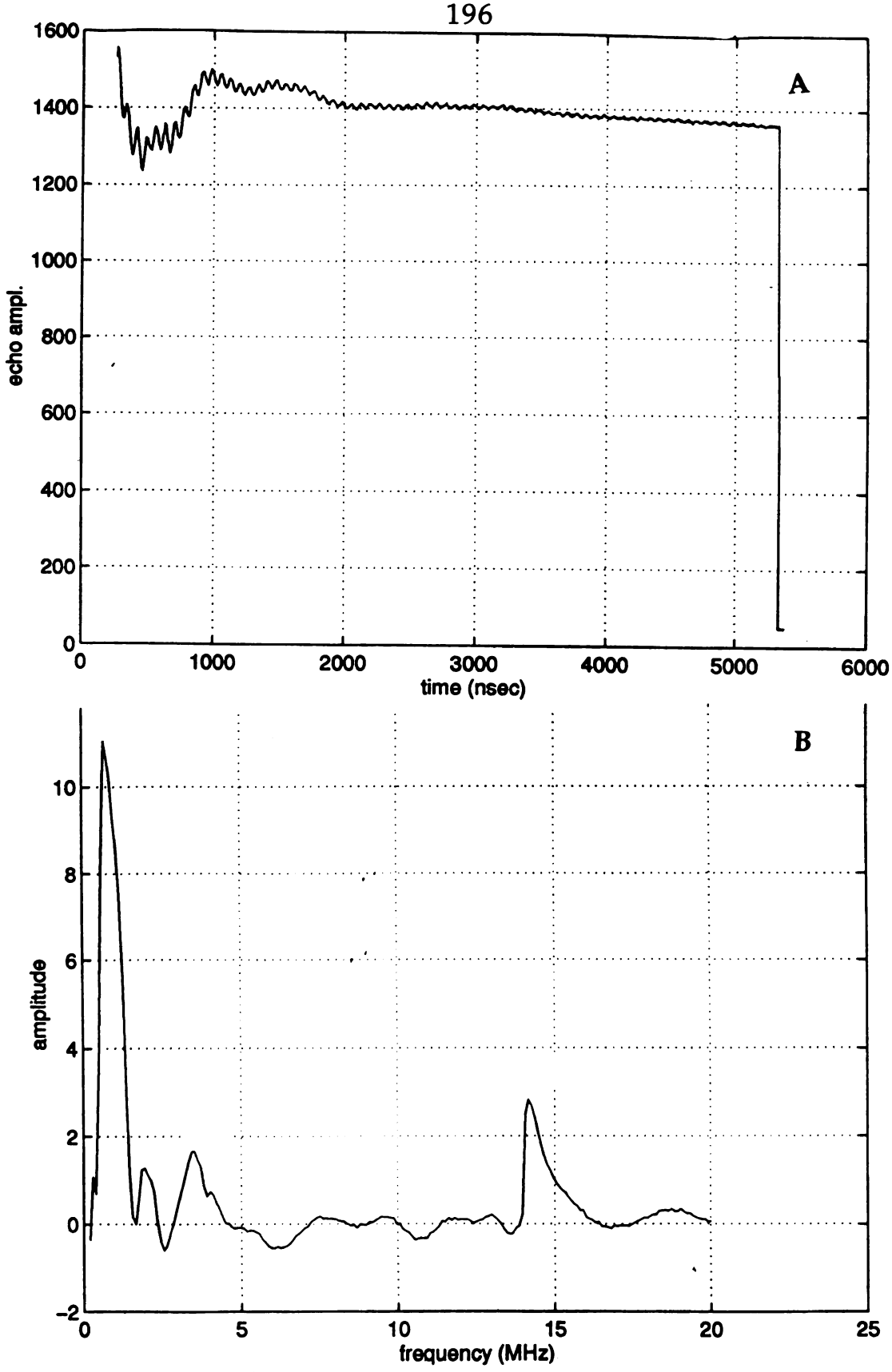

Figure 6.6: A) 3-pulse ESEEM trace of K^+(HMHCY)Na^- at 3300 G, where τ = 324 ns., T=46 ns., tinc = 10 ns., repetition rate = 40 Hz. B) Fourier transform spectrum of A.

completely, but the shape is somewhat distorted. Perhaps the peak was part of the baseline, but generally, baseline features are not such sharp peaks. Several attempts were made to bring out the sodium modulations, if they were present. In addition, two other frequencies were used to try to confidently assign the frequencies, 11.4 GHz and 12.2 GHz. The resonance was located at a higher field strength thus the larmor frequency changed accordingly. The stimulated echo, collected at 4100 G and a tau value of 324 ns, showed a very weak modulation pattern (Figure 6.7). Only protons and potassium were present at this frequency, so more than likely, the initial assignment to sodium was incorrect. Experiments recorded at 12.5 GHz revealed the same modulation pattern as observed at 11.4 GHz with only potassium and protons present. Simulations of all of these data should verify the assignments.

Conclusions

It was not too surprising that the eseem results indicated that the trapped electrons in K^+(HMHCY)Na^- only interacted with the protons and potassium. Initial experiments showed a peak at the expected frequency of sodium, but further investigation negated that assignment. Given the crystal structure of this sodide, the distance between a sodium anion and a trapped electron ranges from 8.66 to 9.94 Å as the sodium anions are effectively shielded from one another by the large complexed cation. There

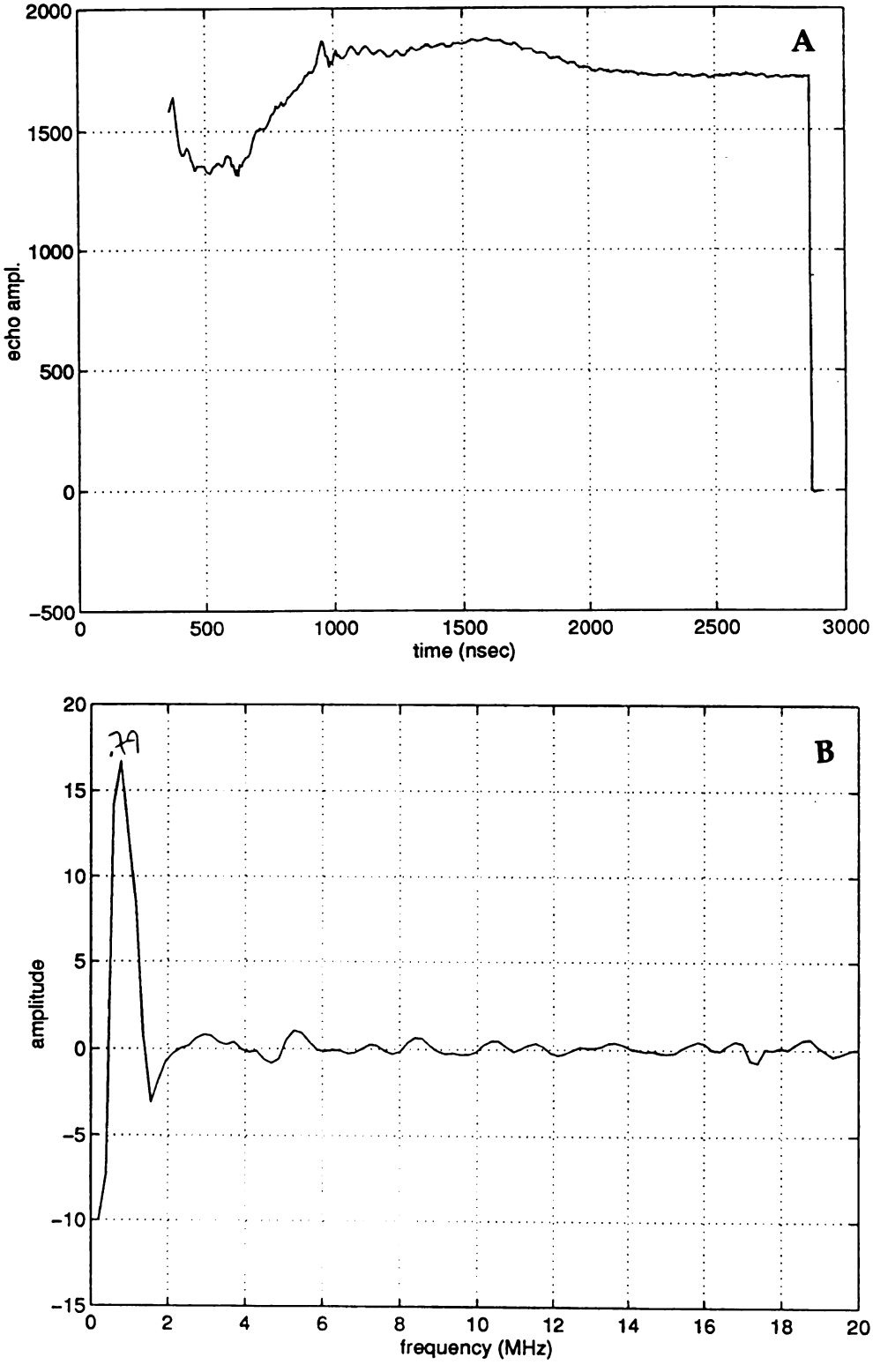

Figure 6.7: A) 3-pulse ESEEM trace of K^+(HMHCY)Na^- at 4250 G, where τ = 288 ns., T=42 ns., tinc = 10 ns., repetition rate = 40 Hz. B) Fourier transform spectrum of A.

is relatively strong interaction between the trapped electrons and the potassium cation; however, there is a reasonable amount of charge distribution near the potassium cation.

BIBLIOGRAPHY

Kuchenmeister, M. E., & Dye, J. L. (1989) *Journal of the American Chemical Society 111*, **Synthesis and Structures of Two Thermally Stable Sodides with the Macrocyclic Complexant Hexamethyl Hexacyclen**, 935-938.

Huang, S., **Single Crystal X-ray Diffraction and Alkali Metal NMR Studies of Alkalides, Electrides and Model Compounds**, 1994.

Kuchenmeister, M. E., & Dye, J. L. (1989) *Journal of the American Chemical Society 111*, **Synthesis and Structures of Two Thermally Stable Sodides with the Macrocyclic Complexant Hexamethyl Hexacyclen**, 935-938.

McCracken, J., Shin, D.-H., & Dye, J. L. (1992) *Applied Magnetic Resonance 3*, **Pulsed EPR Studies of Polycrystalline Cesium Hexamethyl Hexacyclen Sodide**, 305-316.

Mims, W. B. (1972) *Physical Review B 6*, 3543-3545.

Mims, W. B., & Peisach, J. (1989) (Hoff, A. J., Ed.) pp 1-57, Elsevier, New York.

Shin, D.-H., Ellaboudy, A. S., Dye, J. L., & DeBacker, M. G. (1991) *Journal of Physical Chemistry 95*, **EPR Studies of Electrons Trapped in Sodides**, 7085-7089.

Ward, D., Kuchenmeister, M., & Dye, J. L. (1989) *unpublished results, this laboratory.*

Warncke, K., & McCracken, J. (1994) *Journal of Chemical Physics*, **2H Electron Spin Echo Envelope Modulation (ESEEM) Spectroscopy of Strong, a-Hydrogen Hyperfine Coupling in Randomly-oriented Paramagnetic Systems.**,